Virtual Model Building for Multi-Axis Machine Tools Using Field Data

by

Chia-Pei Wang

A thesis

presented to the University of Waterloo

in fulfillment of the

thesis requirement for the degree of

Doctor of Philosophy

in

Mechanical and Mechatronics Engineering

Waterloo, Ontario, Canada, 2023

Examining Committee Membership

The following served on the Examining Committee for this thesis. The decision of the Examining Committee is by majority vote.

External Examiner	Shreyes N. Melkote Professor, Mechanical Engineering Georgia Institute of Technology
Supervisor	Kaan Erkorkmaz Professor, Mechanical and Mechatronics Engineering University of Waterloo
Supervisor	John McPhee Professor, System Design Engineering University of Waterloo
Internal Member	Kaan Inal Professor, Mechanical and Mechatronics Engineering University of Waterloo
Internal Member	Behrad Khamesee Professor, Mechanical and Mechatronics Engineering University of Waterloo
Internal-external Member	Glenn Heppler Adjunct Professor, System Design Engineering University of Waterloo

Author's Declaration

This thesis consists of material all of which I authored or co-authored: see Statement of Contributions included in the thesis. This is a true copy of the thesis, including any required final revisions, as accepted by my examiners.

I understand that my thesis may be made electronically available to the public.

Statement of Contribution

[C1] C. Wang, K. Erkorkmaz, and J. McPhee, "Virtual model building for 5-axis laser drilling machine from field data", 8th International Conference on Virtual Machining Process Technology (VMPT), Vancouver, Canada, 2019.

[J1] C. Wang, K. Erkorkmaz, J. McPhee, and S. Engin, "In-process digital twin estimation for high-performance machine tools with coupled multibody dynamics", CIRP Annals, 69(1), 321-324, 2020.

[J2] C. Wang, K. Erkorkmaz, J. McPhee, and S. Engin, "Identification of flexible joint multibody dynamic models for machine tool feed drive assemblies via IMU and CNC data" (under preparation for submission to ASME Journal of Manufacturing Science and Engineering).

Through the course of PhD study, the author Mr. Chia-Pei Wang has prepared or published the papers listed above. They are also the backbone of this thesis from Chapter 3 to Chapter 7.

[C1] presents earlier research on the identification of open-loop electromechanical dynamics of a multi-axis feed drive system. The model is derived considering multi-rigid-body dynamics, nonlinear friction, and nonlinear motor ripple. This open-loop dynamic model is identified by pseudo-random in-process servo data. This work is reported in Chapter 3 of this thesis.

[J1] presents a novel decoupling formulation to derive an equivalent dynamic model representing a nonlinear closed-loop control system. This paper also proposes the corresponding model identification approach utilizing pseudo-random in-process servo data. Experimental validation shows that coupled nonlinear dynamic behaviors such as inter-axis coupling effects and the dynamic responses to nonlinear motor ripple are nicely captured. The proposed methodology and experimental validation of this paper are detailed in Chapter 4 of this thesis.

[J2] is an extension of [J1]. This paper focuses on the modeling and identification of multibody dynamic models with lumped flexible joints. To identify such models with the proposed identification approach, the internal structural vibration has to be captured. This paper proposes to apply a MEMS IMU to capture the internal structural vibration. Experimental validation shows that vibratory coupled nonlinear dynamic behaviors such as inter-axis coupling effect and position-dependent effects are

nicely captured. The methodology and experimental validation of this paper are detailed in Chapter 5 ~ Chapter 7 of this thesis.

Regarding the contribution to [C1], [J1], and [J2], Mr. Chia-Pei Wang is the originator of the new theories developed in these papers and also gets the credit for the experimental validation. Prof. Kaan Erkorkmaz and Prof. John McPhee are Mr. Wang's supervisors and have provided expertise in control and multibody dynamics respectively. Dr. Serafettin Engin is from Pratt & Whitney Canada, and has contributed to the research and provided industrial direction and assistance.

Abstract

Accurate machine dynamic models are the foundation of many advanced machining technologies such as virtual process planning and machine condition monitoring. Viewing recent designs of modern high-performance machine tools, to enhance the machine versatility and productivity, the machine axis configuration is becoming more complex and diversified, and direct drive motors are more commonly used. Due to the above trends, coupled and nonlinear multibody dynamics in machine tools are gaining more attention. Also, vibration due to limited structural rigidity is an important issue that must be considered simultaneously. Hence, this research aims at building high-fidelity machine dynamic models that are capable of predicting the dynamic responses, such as the tracking error and motor current signals, considering a wide range of dynamic effects such as structural flexibility, inter-axis coupling, and posture-dependency.

Building machine dynamic models via conventional bottom-up approaches may require extensive investigation on every single component. Such approaches are time-consuming or sometimes infeasible for the machine end-users. Alternatively, as the recent trend of Industry 4.0, utilizing data via Computer Numerical Controls (CNCs) and/or non-intrusive sensors to build the machine model is rather favorable for industrial implementation. Thus, the methods proposed in this thesis are top-down model building approaches, utilizing available data from CNCs and/or other auxiliary sensors. The achieved contributions and results of this thesis are summarized below.

As the first contribution, a new modeling and identification technique targeting a closed-loop control system of coupled rigid multi-axis feed drives has been developed. A multi-axis closed-loop control system, including the controller and the electromechanical plant, is described by a multiple-input multiple-output (MIMO) linear time-invariant (LTI) system, coupled with a generalized disturbance input that represents all the nonlinear dynamics. Then, the parameters of the open-loop and closed-loop dynamic models are respectively identified by a strategy that combines linear Least Squares (LS) and constrained global optimization. This strategy strikes a balance between model accuracy and computational efficiency. This proposed method was validated using an industrial 5-axis laser drilling machine and an experimental feed drive, achieving 2.38% and 5.26% root mean square (RMS) prediction error, respectively. Inter-axis coupling effects, i.e., the motion of one axis causing the dynamic responses of another axis, are correctly predicted. Also, the tracking error induced by motor ripple and nonlinear friction is correctly predicted as well.

As the second contribution, the above proposed methodology is extended to also consider structural flexibility, which is a crucial behavior of large-sized industrial 5-axis machine tools. More importantly, structural vibration is nonlinear and posture-dependent due to the nature of a multibody system. In this thesis, prominent cases of flexibility-induced vibrations in a linear feed drive are studied and modeled by lumped mass-spring-damper system. Then, a flexible linear drive coupled with a rotary drive is systematically analyzed. It is found that the case with internal structural vibration between the linear and rotary drives requires an additional motion sensor for the proposed model identification method. This particular case is studied with an experimental setup.

The thesis presents a method to reconstruct such missing internal structural vibration using the data from the embedded encoders as well as a low-cost micro-electromechanical system (MEMS) inertial measurement unit (IMU) mounted on the machine table. It is achieved by first synchronizing the data, aligning inertial frames, and calibrating mounting misalignments. Finally, the unknown internal vibration is reconstructed by comparing the rigid and flexible machine kinematic models. Due to the measurement limitation of MEMS IMUs and geometric assembly error, the reconstructed angle is unfortunately inaccurate. Nevertheless, the vibratory angular velocity and acceleration are consistently reconstructed, which is sufficient for the identification with reasonable model simplification.

Finally, the reconstructed internal vibration along with the gathered servo data are used to identify the proposed machine dynamic model. Due to the separation of linear and nonlinear dynamics, the vibratory dynamics can be simply considered by adding complex pole pairs into the MIMO LTI system. Experimental validation shows that the identified model is able to predict the dynamic responses of the tracking error and motor force/torque to the input command trajectory and external disturbances, with 2% ~ 6% RMS error. Especially, the vibratory inter-axis coupling effect and posture-dependent effect are accurately depicted.

Overall, this thesis presents a dynamic model-building approach for multi-axis feed drive assemblies. The proposed model is general and can be configured according to the kinematic configuration. The model-building approach only requires the data from the servo system or auxiliary motion sensors, e.g., an IMU, which is non-intrusive and in favor of industrial implementation. Future research includes further investigation of the IMU measurement, geometric error identification, validation using more complicated feed drive system, and applications to the planning and monitoring of 5-axis machining process.

Acknowledgements

I would like to express my sincere gratitude to my supervisors, Professor Kaan Erkorkmaz and Professor John McPhee for the guidance, encouragement, and motivation they have provided over the past years.

I would like to thank Dr. Serafettin Engin, Dr. Jochem Roukema and everyone at Pratt & Whitney Canada for their assistance and feedback in validating my research. It is a great pleasure and experience working with them.

I would like to thank my thesis committee members: Professor Shreyes Melkote, Professor Glenn Heppler, Professor Kaan Inal, and Professor Behrad Khamesee for taking time reading my thesis and contributing constructive feedback. Special thanks go to Professor Melkote for his in-person visit to Waterloo.

Sincere thanks go to our strong technical staffs: Mr. Jason Benninger, Mr. Karl Janzen, Mr. Robert Wagner and Mr. Neil Griffett. The experimental setup cannot be done without their tremendous technical support.

Many thanks go to all the brilliant colleagues in the Precision Controls Laboratory. We learn from each other through the journey of Ph.D. program.

Lastly, I greatly appreciate the encouragement and support of my dear family, which made my graduate studies possible.

This research was sponsored by Natural Sciences and Engineering Research Council of Canada (NSERC) and Pratt & Whitney Canada (P&WC).

Table of Contents

List of Figures

List of Tables

Chapter 1
Introduction

1.1 Background and Research Motivation

1.1.1 Virtual Machining with Digital Twin

Nowadays, since most Computer-Aided Manufacturing (CAM) software can only simulate the "ideal" machining process, process planning therefore heavily relies on the experience of machine operators. Time-consuming trial cuts are necessary for verifying and adjusting the process until part quality requirements are satisfied. To mitigate such problems, the concept of virtual machining [1] was proposed, where the machining operation can be predicted by virtual machine models, i.e., digital twins [2] (see Figure 1-1).

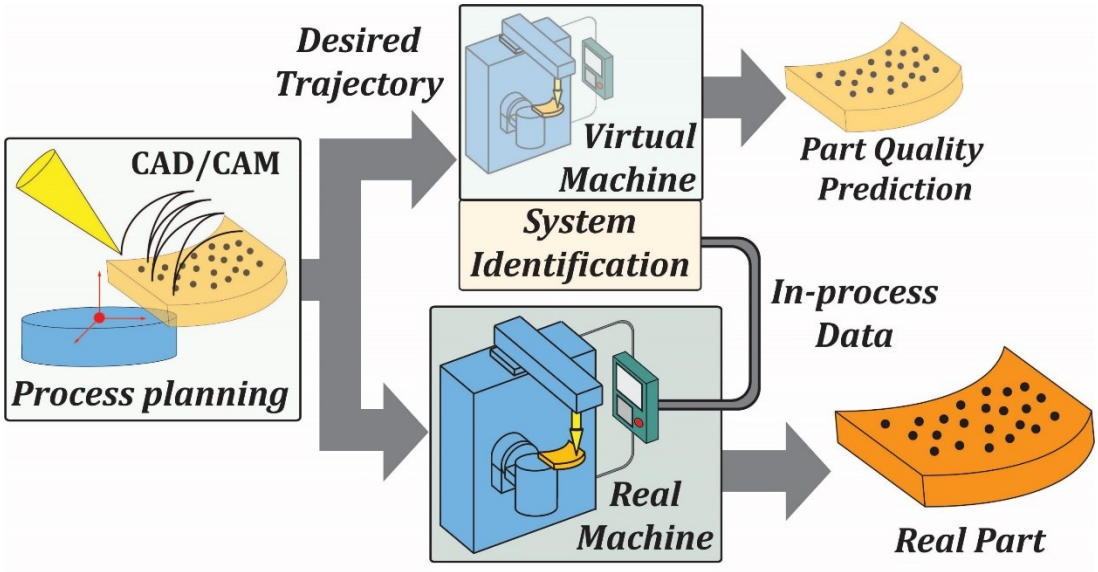

Figure 1-1 Virtual model and machining processes.

A thorough modeling of the machine and process involves several aspects, such as the cutting mechanics, tool wear, tool flexibility, spindle dynamics, thermal expansion, etc. In particular, the dynamic behavior of the feed drives is one of the dominant factors impacting the productivity and resulting part quality in machining. With the aid of high-fidelity machine feed drive models, high-productivity machining trajectory planning, without violating part tolerances, can be designed in a virtual environment, or in semi-real time (as a digital twin). If the model of the feed drive control system can be built, the production trade-off (see Figure 1-2) between production speed, contour accuracy, and

surface finish can then be predicted and optimized without time-consuming and expensive trials on real machines (see Virtual CNC in Section 2.3.1).

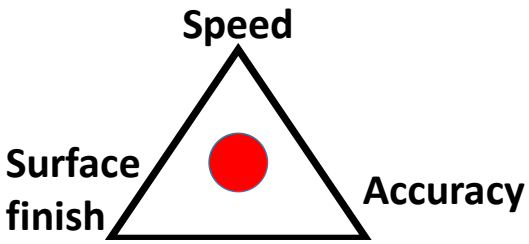

Figure 1-2 Performance trade-off of a machine tool feed drive control system [3].

Furthermore, an accurate dynamic model of the feed drive mechatronic system can be used for monitoring the machining process, such as real-time estimation of the cutting forces through indirect methods (like Kalman filtering of motor current and/or low-cost accelerometer signals), without having to apply intrusive and expensive direct force measurement methods, such as using table or rotational dynamometers [4]. Lastly, a dynamic model of the machine tool multi-axis feed drive assembly can be used for machine condition monitoring, by tracking the evolution of key parameters, feed drive natural frequency, stiffness, and damping values. Such models can also be used to train machine learning methods, to help diagnose faults and root causes of error.

On the other hand, the concept of Industry 4.0 aims to establish smart factories with integrated virtualization, monitoring, data integration, self-optimization, and control functionalities within and across manufacturing processes, taking advantage of increasing connectivity and automation capabilities [5]. In this context, developing the capability to identify realistic dynamic models of production machines, in a practical manner, is key to elevating the overall productivity, efficiency, and longevity in the operation of machine tools and other production equipment.

1.1.2 Digital Twin Estimation for Multi-axis Machine in the Context of Industry 4.0

Building a machine model via conventional bottom-up approach may require extensive investigation of every single component, which is time-consuming or sometimes infeasible (especially for machines already operational in industry). Alternatively, following the trend of Industry 4.0, commercial Computer Numerical Controls (CNCs) have been increasingly powerful to provide real-time in-process data, which can be used to estimate machine models in a top-down sense. Consequently, such a non-intrusive model-building approach is more suitable for industrial implementation [2].

Following the above concept, numerous top-down identification approaches, (i.e., referred to as 'rapid identification'), have been developed [6][7][8][9]. The identified machine models can predict machining accuracy due to rigid body control, structural vibration, and nonlinear friction (see Section 2.3.2).

Overall, viewing the design of modern high-performance machine tools, the following trends can be observed: (a) To enhance the productivity, high-speed direct drive motors are becoming increasingly used. (b) To enhance the versatility, the configurations of machine axes are becoming more and more diverse and complex (see Section 2.4). Thus, coupled multibody dynamics needs to be carefully investgated and considered, to obtain realistic digital models of such machines.

Regarding multi-axis machines, academic research in the past primarily focused on the kinematics and trajectory planning. Multibody dynamics in the context of multi-axis machines has been less studied. While machine model estimation with multibody dynamics is very much worth investigating, vibration response due to limited structural rigidity is also an important attribute that must be considered simultaneously, especially as it is prevalent in medium-to-large-sized multi-axis machine tools. Furthermore, when nonlinear multibody dynamics are invloved, the vibratory behavior also becomes nonlinear and posture-dependent. Hence, the machine vibratory dynamics should, in the ideal case, be studied hand-in-hand with multibody dynamics.

However, rather than resorting to computationally expensive and highly complex flexible multi-body (FMB) approaches, which are typically generated via FEM and model truncation, a more practical and physically interpretable approach would successfully fill the gap between simple (rigid body) decoupled modeling and highly complex FEM approach, thereby allowing computationally efficient and sufficiently accurate models which can be readibly applied in industry as *easy-to-identify*, *easy-to-use* and *sufficiently accurate* 'digital twins'. This has been the primary motivation of this thesis research.

1.2 Research Objective

This thesis has focused on estimating dynamic models of multi-axis feed drive control systems, directly from field (i.e., in-process CNC) data, or sometimes non-intrusive instrumentation (e.g., low-cost sensors), which can be used for the purposes of process planning, optimization, and machine and process monitoring. Table 1-1 shows the roadmap of the conducted research. Specifically, this thesis has aimed at extending the earlier rapid identification methodologies [6][7][8][9], to consider dynamic

coupling effects between the axes and the structural flexibility. In addition to utilizing servo data from CNC, data from low-cost and practical auxiliary sensors, e.g., an IMU (Inertial Measurement Unit), has also been utilized for identifying a model which can capture both coupled multibody dynamics, and also structural vibrations.

Table 1-1 Research roadmap on digital twin estimation for multi-axis machines.

	Model assumption	
Erkorkmaz et al. [4]	Decoupled single-axis	Rigid body model
Tseng et al. [7]	Decoupled single-axis	Flexible model
Chapter 3 ~ 4	Coupled multi-axis	Rigid body model
Chapter 5 ~ 7	Coupled multi-axis	Flexible model

The major research contributions are two new identification methods listed as follows:

A. A new identification method for closed-loop control system of coupled rigid multi-axis feed drives. This has been achieved by incorporating the identification for multibody dynamics, and the decoupling of the nonlinear open-loop MIMO (multiple-input multiple-output) dynamics from the closed-loop MIMO LTI (linear time-invariant) dynamics. This contribution is detailed in Chapter 3 and Chapter 4.

B. A new identification method based on Contribution A, where structural flexibility is also considered. In addition to considering the nonlinear multibody dynamics, the structural vibration is captured by extending the higher-order MIMO LTI portion of the model. In this step, it is seen that an IMU measurement is essential to reconstruct the internal vibration signal (as velocity and acceleration terms), as this response cannot be readily captured with the existing position feedback sensors on a servo control system. This contribution has been developed in Chapter 5 through Chapter 7.

1.3 Thesis Layout

Chapter 2 is a literature review covering relevant literature to this thesis, such as the modeling of machine tool feed drives, an overview of 5-axis machines, and an introduction to IMUs.

Chapter 3 presents the identification of the open-loop (plant) dynamics. The identification takes numerous physical phenomena into account, such as multibody dynamics, motor ripple, and nonlinear friction. Although the methods reviewed in this chapter are prior art, they are essential to the methodologies developed in the later chapters.

Chapter 4 introduces a new identification method for closed-loop control system of coupled rigid multi-axis feed drives. An equivalent dynamic model and the corresponding identification procedures are first elaborated, followed by experimental validation using two different multi-axis feed drives.

Chapter 5 extends the method in Chapter 4 to also consider the structural flexibility. As structural flexibility can lead to a very broad set of dynamic system equations, the research scope is first defined and limited by analyzing the prominent types of vibratory dynamics in a general linear (translating) feed drive. Then, adding a rotary drive on top of a linear drive (which is common in machine tools), it is found that if there is significant structural flexibility between the linear and rotary drives, the model identification additionally requires a motion sensor, e.g., an IMU, to measure the internal structural vibration, which is missing from the feedback of regular position sensors. Then, this case has been experimentally studied in the following chapters.

Chapter 6 first introduces the experimental feed drive with an I-beam type flexible connection element. As an IMU is intended to be used, its relevant fundamental utilization techniques, such as strapdown integration and sensor fusion, are reviewed and applied. Then, the missing vibration of the I-shaped flexible structure is reconstructed by a method by comparing the rigid and flexible kinematic models.

Chapter 7 presents the results of the model identification for the experimental drive. The data from the CNC and the IMU are simultaneously utilized to identify the dynamic model. Not only inter-axis dynamic coupling effect, but also posture-dependent vibratory behavior can be accurately predicted by the identified model. Hence, the proposed identification methodology is validated been, which can be applied and extended for building comprehensive models of a coupled multi-axis feed drive control systems, with mechanical flexibility.

Finally, the conclusions and future research directions are presented in Chapter 8.

Chapter 2
Literature Review

2.1 Introduction

Establishing high-fidelity models of feed drive control systems is critical for virtual process planning. Using the models, the process planner can evaluate the cycle time and control system positioning accuracy. Such models can also enhance process monitoring and provide insight regarding the machine condition.

To achieve higher productivity and versatility, in recent years high-speed machine tools with diverse axis configuration have emerged. Such design trend leads to more complex machine dynamics, as it involves structural vibrations, and also the interaction between axes. In the context of virtual process planning, the influence of these dynamic effects on the dynamic performance of the machine tool must be addressed. The literature review regarding the above research motivation is arranged as follows.

In Section 2.2, literature on the structural dynamics of machine feed drives is presented. This topic is more or less foundational in machine tool research. In addition to structural dynamics, this thesis aims at the modeling and identification of "the entire feed drive control system", so that the control performance with respect to a certain inputs (such as command trajectory or disturbance forces) can be predicted. This is beneficial to the planning and monitoring of production systems. In Section 2.3, such a modeling concept (Virtual CNC) and an identification approach in a top-down sense (rapid identification) are presented. Section 2.4 introduces the configuration and recent design trends of high-performance 5-axis machines. It is found that, in addition to mechanical vibration, the inter-axis dynamic coupling originating from multibody dynamics is critical. Since this issue has been investigated more thoroughly in robotics than in machine tools, Section 2.5 reviews the modeling and identification of multibody dynamics in the field of robotics.

The proposed identification method for a multibody system with mechanical flexibility requires extra motion sensor(s), to capture missing internal structural vibration. A variety of motion sensors are surveyed in Section 2.6.1. As IMUs are suitable for this application, this sensor is introduced in Section 2.6.2. To obtain the best estimated attitude information, the IMU signals have to be processed by a sensor fusion algorithm, reviewed in Section 2.6.3.

2.2 Modelling of Structural Dynamics of Machine Feed Drives

2.2.1 Rigid Body Dynamics

A feed drive including the mechanical structure (assumed to be rigid) and the current amplifier can be simplified as in Figure 2-1.

A current command I_s is sent to a current controller, which is usually embedded in an amplifier for the purpose of servomotor control. The current controller regulates the actual armature current I in order to compensate the back electromotive force (EMF) voltage E_b and the electrical dynamics characterized by inductance L and resistance R when the armature is rotating by (angular) velocity ω. The bandwidth of the current control is substantially higher than that of velocity and position control. Therefore, when analyzing the mechanical response, it is common to neglect the current controller and electrical components' dynamics , i.e. $I_s \approx I$. Then, the motor torque τ can be indirectly measured by $K_t I_s$, where K_t is the actuator torque constant.

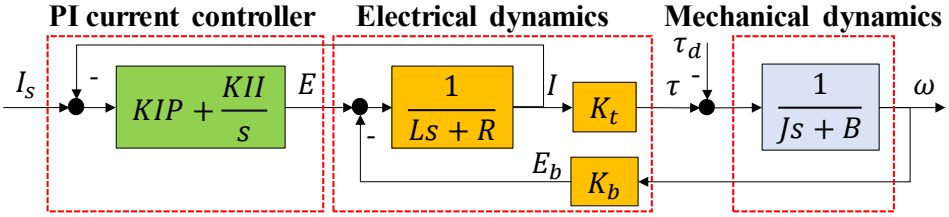

Figure 2-1 A feed drive as an electro-mechanical system.

Assuming that the mechanical structure is sufficiently rigid and driven by a smooth trajectory (lacking high-frequency content which would excite structural vibrations), the mechanical plant can be simplified as a rigid body with inertia J and viscous damping B. Then, the dynamic equation can be written as:

$$\omega(s) = \frac{1}{Js + B}[\tau - \tau_d] \tag{2.1}$$

Assuming τ_d as a constant Coulomb friction, then J, B, and τ_d can be simply estimated by Least Squares (LS) estimation using the measured I_s and ω, as such in [10].

2.2.2 Vibratory Dynamics

Vibratory dynamics are very essential characteristics for the machine tool feed drives, as the servo (actuation) force also excites the mechanical resonance. This constitutes a limit to allowable maximum acceleration and jerk values in trajectory planning. In addition, process (machining) forces also excite the vibratory dynamics, which leads to wavy surface finish or even unstable (chatter) machining conditions.

In industrial machines, one of the most common actuation mechanisms is the ball screw drive, of which the flexibility is one of the primary issues causing machine tool vibrations. A flexible ball screw drive can be simply described by a two-mass spring-damper model in Figure 2-2, which captures the rigid-body mode and the dominant vibratory mode. More complicated lumped models for capturing higher-order axial and rotational modes [11][12][13] have also been proposed, as shown in Figure 2-3-Figure 2-5.

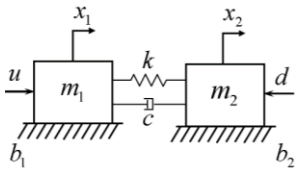

Figure 2-2 A two-mass model.

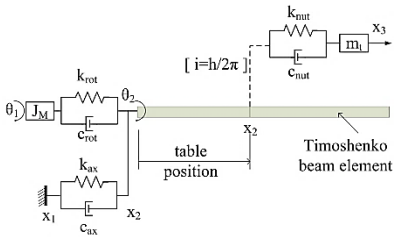

Figure 2-3 Hybrid model [12].

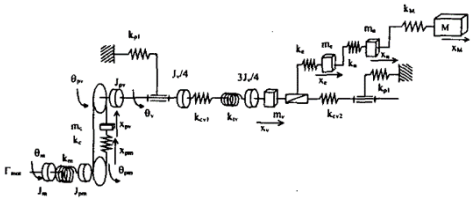

Figure 2-4 8-mass model [13].

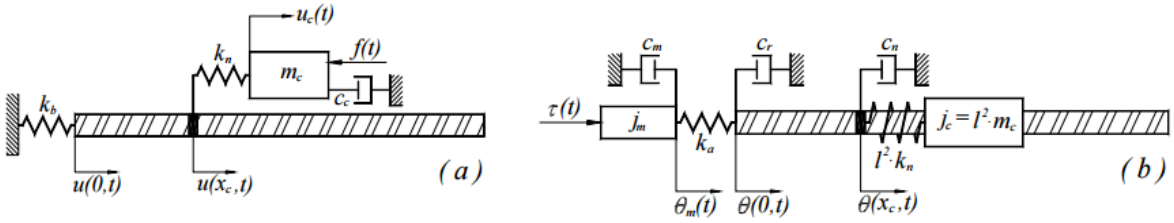

Figure 2-5 Ball screw feed system, axial (a) and rotational (b) model [11].

Machine frame vibration is more complicated and harder to describe by lumped models with physical meaning. Instead, it can be modeled by FEM.

Alternatively, a generalized expression for servo systems with inherent vibratory modes can be described by the modal analysis technique, assuming proportional damping characteristics – which seems to agree well with most machine tool structures:

$$G(s) = \frac{1}{Js^2 + Bs} + \sum_{i=1}^{N} \frac{{sign_i}/{m_i}}{s^2 + 2\omega_{n_i}\zeta_i s + {\omega_{n_i}}^2} \tag{2.2}$$

This dynamic equation can be used for a single drive with one rigid-body mode and N decoupled flexible modes, where ω_{n_i}, ζ_i, and m_i are natural frequency, damping ratio, and modal mas of the ith mode. Then, the parameters can be determined by system identification. Prior to the author's PhD study at U.Waterloo, he successfully used this approach to identify feed drives in a 3-axis milling machine [14] (see Figure 2-6). The feed drive was excited by a swept-frequency sine torque input. The position feedback is measured for the curve fitting in the frequency domain to identify multiple flexible modes. Those modes could originate from the ball screw vibration, as well as the complex machine tool structure vibration. The identified transfer function $G(s)$ is later integrated with the controller model and friction model. Thus, the tracking error in the time domain can be predicted. The control parameters can also be automatically optimized based on the identified model.

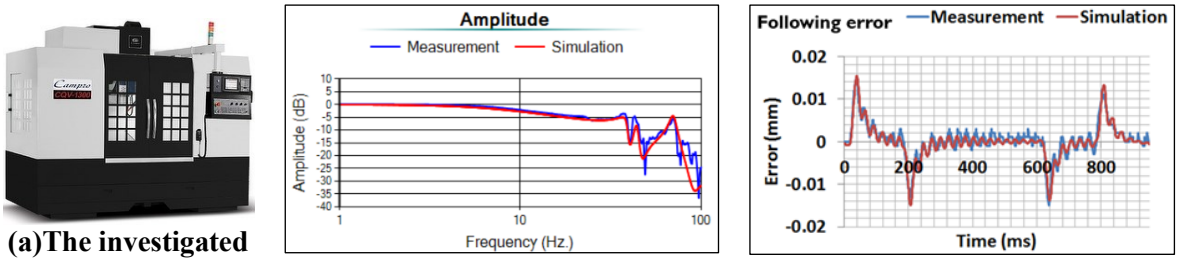

(a)The investigated machine. **(b) Frequency domain response.** **(c) Tracking error prediction.**

Figure 2-6 Identification and simulation result for a flexible drive [14].

In general, lumped mass-spring-damper modeling is suitable for building a computationally efficient model, where the parameters can be identified by input/output signals collected from the CNC. But if the parameters in the model are constants, this type of model cannot consider the position-dependent dynamics problem, i.e., the natural frequency changing with axis travel [15].

2.2.3 Machine Structure Analysis by Finite Element Method (FEM)

As shown in Figure 2-7, FEM can model the flexibility of the structures with complicated geometry. It is an essential tool to shorten the time-to-market during the product development stage and widely used in the machine tool industry [16][17].

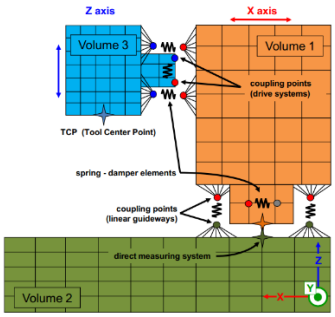

Figure 2-7 A FE-model of machine tool structure [17].

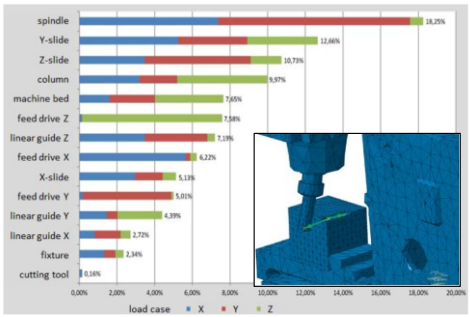

Figure 2-8 Displacement portions analysis for three cutting load cases [18].

Generally, the complex machine structure is represented by 3D-solid elements, while the joints, including the guideways and bearings, are simplified by lumped elements for reducing the computational cost. Figure 2-8 demonstrates an example of FEM analysis, which evaluates the tool deflection contributed by each component [18]. This also reveals the necessity of using FEM, because the column and machine bed contribute considerable deflection, which cannot be easily analyzed with lumped models. For the purpose of analyzing the performance of the feed drive, in his earlier study, the author successfully used FEM to simulate mode shapes excited by the motor actuation force (see Figure 2-9). This is important information, which can be used to optimize the machine tool structure. For example, the author applied structural topology optimization to a machine tool head structure (see Figure 2-10) [19]. These examples show the benefit of FEM in machine tool design.

However, the accuracy of the simulation relies highly on the correctness of the properties of each component, e.g. contact stiffness and damping of the guideway, material density and Young's modulus of the cast iron frame, etc. In addition, the contact stiffness and damping may change with the assembly processes and contact conditions, e.g. surface roughness, lubrication, preload, component wear, etc. Thus, these properties show noticeable variation [20]. They can be identified by dedicated experiments [21][22][23][24] under certain conditions. Figure 2-11 [24] is an example of measuring the equivalent contact stiffness and damping for a given component. The component tested has to be disassembled from the machine and mounted on a test bench. This approach, while being a valuable contribution to new fundamental knowledge, is difficult and intrusive to apply on machine tools already in use on a shop floor.

Additionally, the FE analysis requires highly detailed machine design information, e.g., complete computer-aided design (CAD) models, which may not always be disclosed to the end users in industry. As a result, this type of **bottom-up model-building approach** is usually more suitable when the

machine is still in the design or development stage. The obtained results can guide the machine designer to understand and compare various sources of flexibility, vibratory response, and positioning error. It is no coincidence that majority of such research originates from countries with highly active machine tool industries.

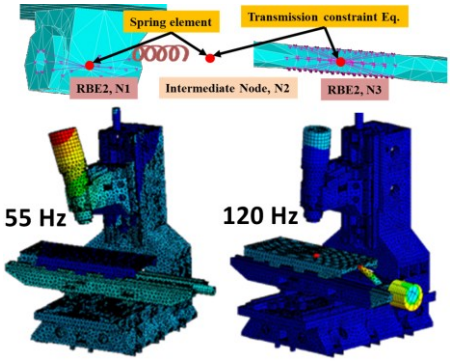

Figure 2-9 Modal analysis of the whole machine structure [14].

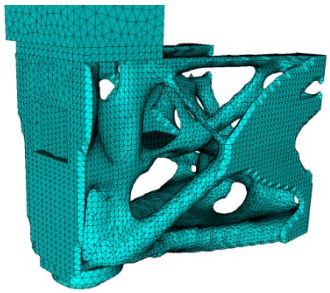

Figure 2-10 Structural topology optimization of a machine tool head [19].

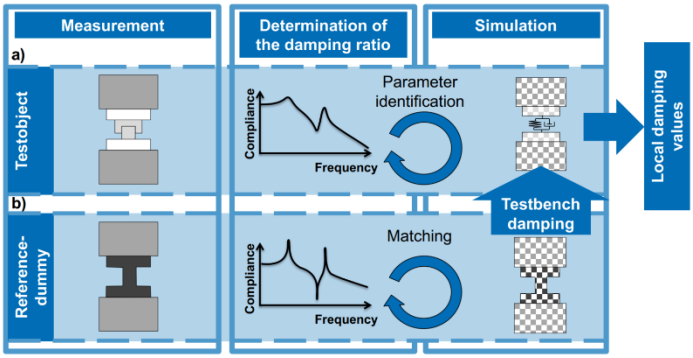

Figure 2-11 A measuring system for the normal contact stiffness and damping [24].

2.2.4 Friction Modelling

Friction is a result of complex interactions between two contacting surfaces with relative motion [25]. When machining accuracy tolerance is down to the micron-level, the friction in feed drives becomes one of the primary sources of positioning errors. Common undesired friction induced phenomena, which deteriorate the positioning accuracy, are outlined below. At velocity reversals, quadrant glitch is unavoidable due to the static friction. At extremely low velocity, stick-slip phenomenon may occur and even induce unwanted vibration. Thus, a limit cycle behaving as fluctuating motion around the positioning reference may occur due to the interaction between the integral control and nonlinear friction. The above phenomena can be represented by various friction models, as illustrated below.

Static (Classical) Friction Models

In classical friction models [10][25][26], the friction force $F_f(v, F_a)$ is a function of the relative velocity v and the applied actuation force F_a as:

$$F_f(v, F_a) = \begin{cases} s(v) + \sigma_2 v & if\ v \neq 0 \\ F_a & if\ v = 0\ and\ |F_a| < F_s \\ F_s sign(F_a) & otherwise \end{cases} \tag{2.3}$$

F_s is the breakaway force, and σ_2 is viscous friction coefficient. $s(v)$ can be a simple Coulomb friction model, such as $s(v) = F_c sign(v)$, or a Stribeck curve as:

$$s(v) = sign(v)\left(F_c + (F_s - F_c)e^{-|\dot{v}/v_s|}\right) \tag{2.4}$$

Above, F_c, F_s, and v_s are Coulomb friction, Stribeck friction, and Stribeck velocity respectively. This model uses inequalities and if-else criteria to determine the friction at near-zero velocity, i.e. the stiction region. This model is simple, but has several drawbacks as illustrated in the following.

Problems in Numerical Simulation

In numerical simulation, it is difficult to find the exact zero velocity and the discontinuity due to the sign function. Numerous modifications have been proposed [25]. For example, Karnopp [27] proposed a modified friction law which sets a narrow region around zero velocity. In the slash region in Figure 2-12, the velocity is considered to be zero, and the stiction is then determined by other forces in the system. Brown and McPhee [28] proposed an approximated continuous friction model as a function of velocity (see Figure 2-13). The model can avoid discontinuities and is differentiable.

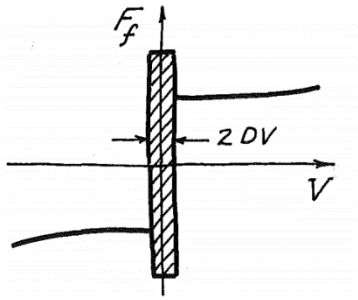

Figure 2-12 Karnopp friction model [26].

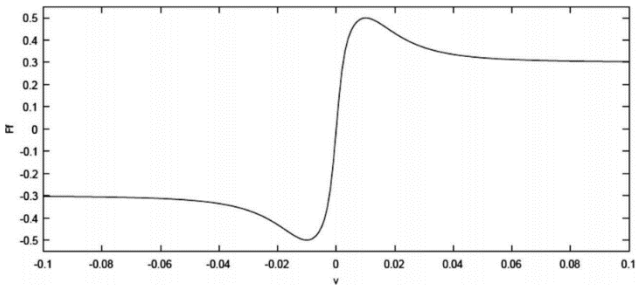

Figure 2-13 Continuous friction function [28].

Another major drawback is that, the friction acting on each body in a multibody system is dependent on the coupled constrained reaction forces. Thus, the analytical value of friction or stiction cannot be

determined explicitly [29]. Haug [26] demonstrated a simulation of a simple three-mass planar mechanism considering friction and stiction. Since the value of stiction and other applied forces should satisfy static equilibrium conditions, in the three-mass system, the analytical stiction criteria turns out to be a large number of inequalities. Hence, the extension of analytical stiction criteria to general multibody systems is still an open research area.

Microscopic Displacement in the Pre-Sliding Regime

It is important to recognize that Eq.(2.3) are not fully accurate, physics-wise, as a deflection is normally experimentally observed at the microscopic scale, even breakaway force is not reached, which is characterized as the pre-sliding regime. In this regime, friction tends to be a function of position [30]. Armstrong [25] has extended classical friction models and proposed a seven-parameter model, which captures the pre-sliding displacement and several friction behaviors. The model essentially integrates two separate models for pre-sliding and sliding regimes respectively. However, the transition between the two regimes is not obvious. As a result, this model has not found wide adoption in practical engineering applications.

Dynamic Friction Models

One of the earliest attempts to describe the friction in the pre-sliding regime was the Dahl model [31], proposed in the late 1960s. The Dahl model was further developed and refined by subsequent efforts, such as the LuGre friction model [32], which captures the Stribeck effect and stick-slip motion. Later, Swevers et al. [33][34] proposed a more elaborate model, called the Leuven model, which includes the frictional properties of the LuGre model and an accurate description of the pre-sliding regime using a hysteresis function with non-local memory. Building on these works, the generalized Maxwell-slip (GMS) model [35] is one of the most recent dynamic friction models, which best captures both the pre-sliding and sliding dynamics of friction in mechatronic systems. This model is essentially a hybrid of the LuGre model and the Maxwell-slip model that was applied in the Leuven model. The GMS model is composed of N elementary slip-blocks and spring elements. It successfully captures the hysteresis effect and frictional memory observed during pre-sliding, and also the Stribeck-type velocity dependent behavior.

2.3 Modelling and Identification of Feed Drive Control System

2.3.1 Virtual CNC

In the context of machine tools and Industry 4.0 style manufacturing [5], having a virtual model of the control system, comprising the electromechanical 'plant' and the digital controller, is indispensable to enhance the machining productivity [1]. Following this concept, Erkorkmaz and Yeung [36] proposed a Virtual CNC system which contains digital models of the controller and the mechanical feed drive (see Figure 2-14). VCNC aims to emulate a real CNC so that its performance can be tested and predicted. Several applications are demonstrated, such as predicting the machining accuracy, modifying process planning (see Figure 2-15), and real-time monitoring [37]. Other research groups such as Sato [38] (see Figure 2-16) and the author [14] also developed similar simulation environments.

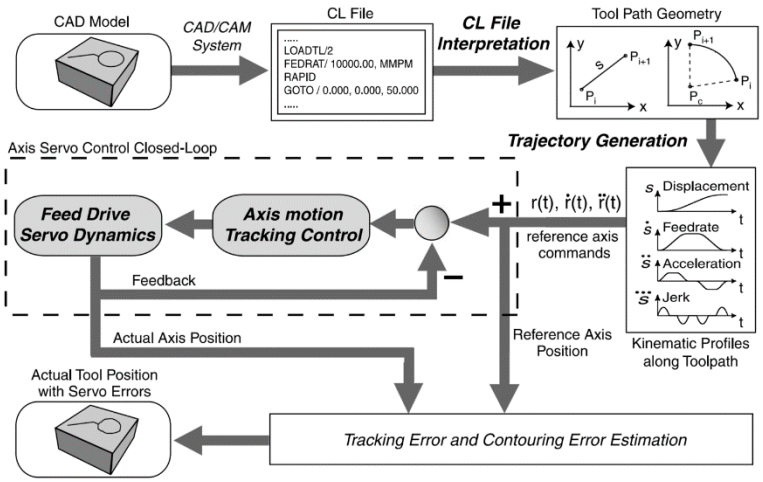

Figure 2-14 Architecture of a virtual CNC system [36].

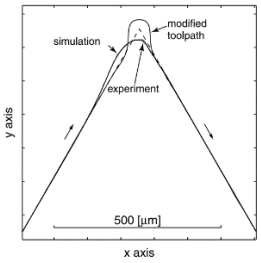

Figure 2-15 Contouring simulation and validation [37].

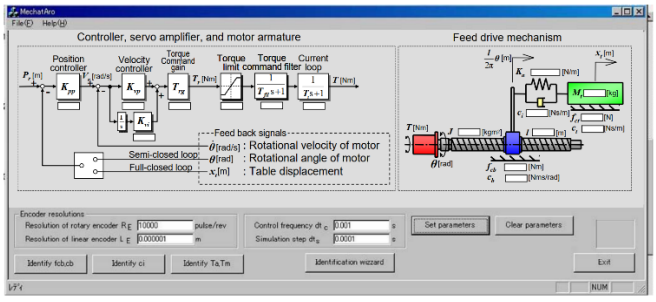

Figure 2-16 GUI of feed drive simulator [38].

2.3.2 Rapid Identification

Motivation

In the above section, Virtual CNC has been shown to advance the performance of machine tools. However, building this model for a machine tool already commissioned in industry is a challenge. Regarding the mechanical model, as mentioned in Section 2.2.3, the bottom-up model-building approach using a high-order FE model (which requires disassembly of the physical machine structures for parameter tuning) is very costly and typically not practical. Building the models of commercial controllers is also challenging. Most commercial CNC providers, like FANUC, Siemens, and HEIDENHAIN, unfortunately do not disclose their control laws in full detail. In some cases, the controller model could be built by a bottom-up approach.

As shown in Figure 2-17 [14], the author built a realistic FANUC controller model which operates according to the control parameters from the CNC panel by a reverse engineering approach. However, this approach is time-consuming and not universal. It involves decoding the control parameters and extensive investigation on the controller product itself. The model is specific only for this product. Therefore, once the control system is upgraded or changed, the investigation has to be repeated.

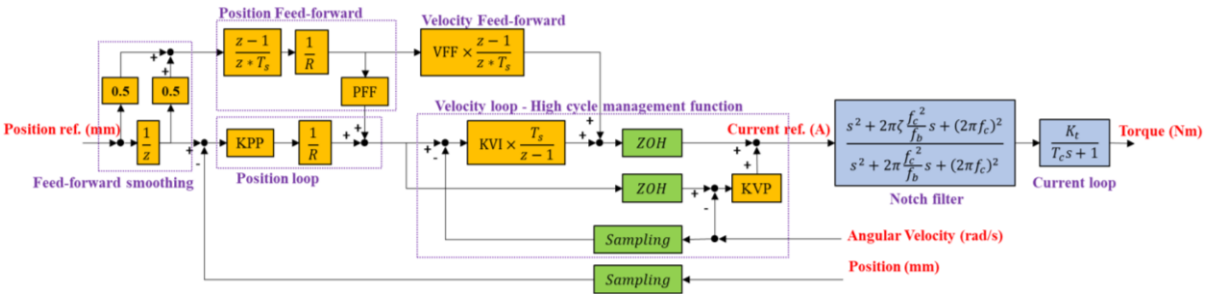

Figure 2-17 A block diagram of FANUC controller built by a reverse engineering [14].

With the increasing accessibility of the data from commercial CNCs, an alternative approach of building a model is utilizing the input and output data of the control system collected during the machine's operation. The data are used to fit simplified models with only sufficient fidelity in a top-down sense. Such approach is non-intrusive and does not cause unproductive machine downtime on the shop floor. Thus, it is favorable and practical for the industry.

Rapid Identification

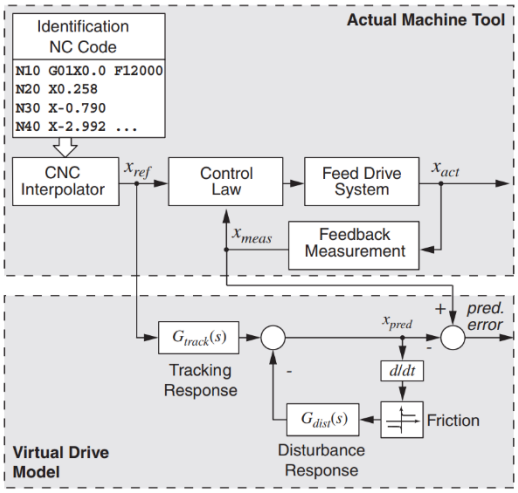

Figure 2-18 Overview of identification scheme.

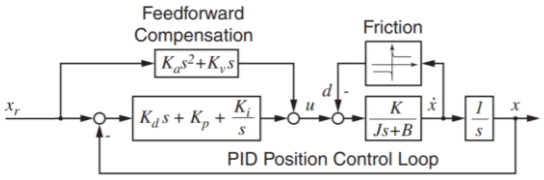

Figure 2-19 PID control system.

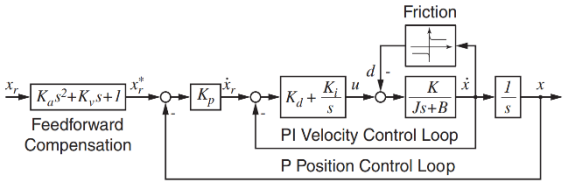

Figure 2-20 P-PI control system.

The concept of rapid identification [4] (see Figure 2-18) considers the closed loop control system as a whole. This general expression can represent PID and P-PI control systems controlling decoupled axes, as shown in Figure 2-19 and Figure 2-20, which are commonly used in industry. In rapid identification, the actual (i.e., measured) position x is considered as the response of the commanded position x_{ref} and disturbance d in a general expression:

$$x(s) = G_{track}(s)x_{ref}(s) + G_{dist}(s)d(s) \tag{2.5}$$

The disturbance $d(s)$ usually refers to the friction which can be represented by various models, such as Coulomb friction, as a function of feed drive motion. It implies that the transfer functions, $G_{track}(s)$ and $G_{dist}(s)$, as well as the friction model, can adequately capture the dominant dynamics of the feed drive control system. The commanded position x_{ref} and actual position x are collected to identify the parameters of the transfer functions. In Eq.(2.5), G_{track} and G_{dist} have different numerators but share the same denominator. Since the system involves a rigid body motion feedback controller with an integrator, the denominator assumes the structure of a *3*rd-order polynomial as:

$$A(s) = s^3 + a_1 s^2 + a_2 s + a_3 = (s + p_r)(s^2 + 2\zeta_c \omega_c s + \omega_c^2) \qquad (2.6)$$

To ensure that only stable models are estimated, which is a reasonable assumption, pole locations, as shown in Figure 2-21, can be found by imposing constraints, on global optimization methods, such as Genetic algorithm [39], Particle Swarm Optimization [9], or global search algorithms [7][8]. Then, the rest of the term (i.e., zeros and gain) in all the transfer functions and the parameters in the friction model can be estimated by Least Squares (see Figure 2-22).

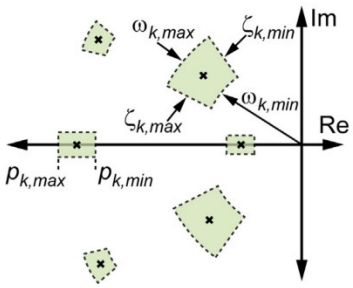

Figure 2-21 Candidate pole locations [7].

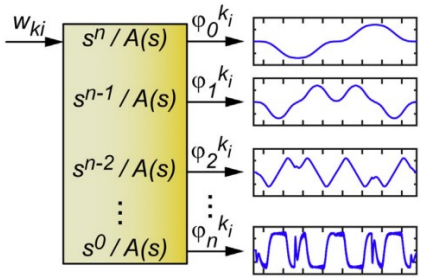

Figure 2-22 Regressors of LS [7].

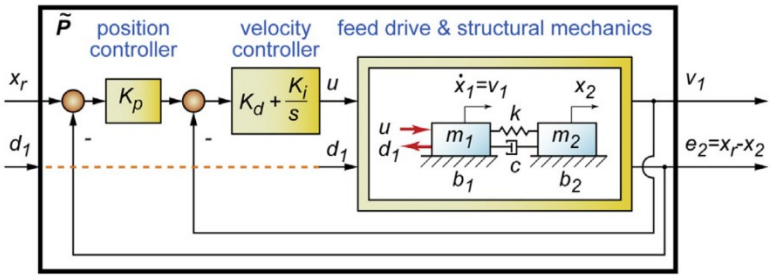

Figure 2-23 A flexible drive presented by a MIMO model [7].

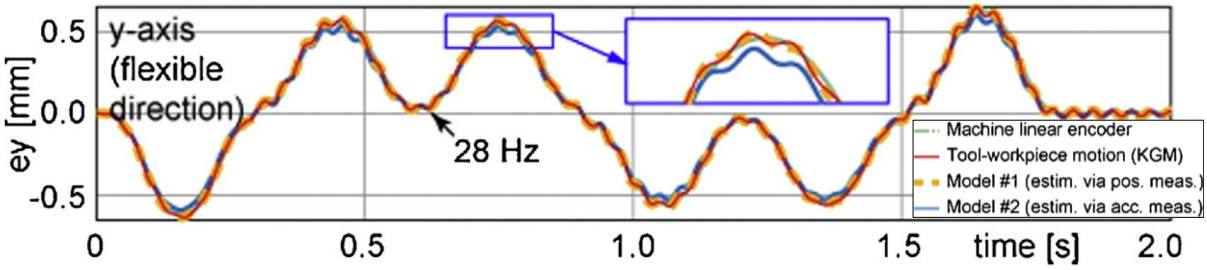

Figure 2-24 Tracking error prediction based on experimental data from a machine tool and flexible fixture assembly [7].

The expression Eq.(2.5) can be generalized as a high-order multi-input multi-output (MIMO) model [8], according to the user's interest, to additionally consider vibratory dynamics [7]. A two-mass

flexible drive model (see Figure 2-23) has two inputs (x_r, d_1), and two outputs (v_1, e_2). Figure 2-24 shows that this model enables the prediction of vibratory behavior in tracking error. The real tool-workpiece motion (red line) is very close to the prediction results (yellow and blue lines).

Among all the published papers at present, MIMO high-order identification has not yet been applied to multi-axis machines with coupled dynamics. This is one of the contributions achieved in this PhD thesis.

2.4 Five-Axis Machine Tools

Machine Configuration

Excluding the degree of freedom of spindle rotation (which becomes important only in specific operations, such as thread cutting), five degrees of freedom are the minimum requirement to define the relative position and orientation between the tool and workpiece. A five-axis machine tool can be composed of any combinations of five linear and/or rotational axes. Most of the existing 5-axis machine tools are composed of 3 linear axes X, Y, Z and 2 rotary axes AB, BC, or AC (A, B, and C designating rotations around X, Y, Z, rep). These five axes can be distributed in either the tool side or the workpiece side with different sequences. Figure 2-25 exemplarily demonstrates 3 different configurations for AC type rotary axes with XY axes at the workpiece side and Z axis at the tool side. According to the above classification, there are hundreds of possible configurations for 5-axis machine tools. The pros and cons of different configurations for 5-axis machine tools were investigated in [40][41].

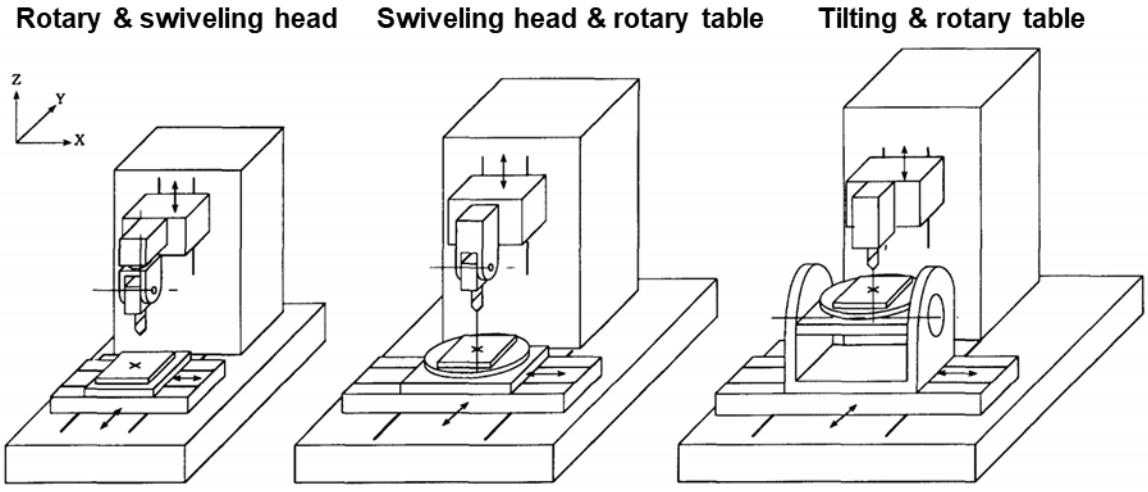

Figure 2-25 Different distributions of A and C rotary axes [41].

Recent Trends in Machine Tool Design

In the past, a machine shop may have been equiped with multiple dedicated machines for different processes. However, this requires large investment, large footprints, and more time spent in loading and unloading workpieces between machines with low utilization rate. Koren, as a pioneer in the 90's, proposed reconfigurable machine tools for realizing reconfigurable manufacturing systems (RMS), in order to handle fluctuating orders from the markets [42]. In practice, multi-functional machine tools gained popularity in the market after 2000 [43]. The concept of multi-functional machines is essentially integrating differents processes in one versitile machining center (see Figure 2-26 (a)). They can be designed originating from a turning machine or a milling machine (see Figure 2-26 (b) and (c)). The tooling is also changeable from milling, turning, boring, grinding, to gear skiving and gear hobbing. Such machines are sometimes also integrated with built-in part measurement (metrology) capabilities. Additionally, hybrid manufacturing capability can also be integrated by exchanging the conventional spindle used for subtractive machining with a laser nozzle for additive manufacturing [44]. Therefore, it is a clear and foreseeable trend that the configuration and kinematics of modern machine tools is becoming more complex and diversified.

(a) Integrated machining process.

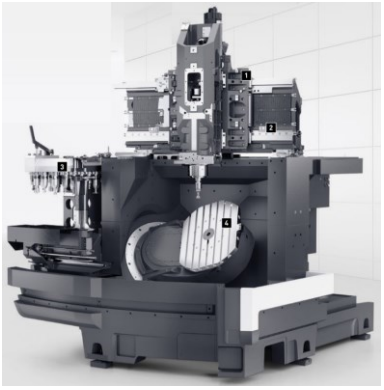

(b) Turn-mill machine center.

(c) Mill-turn machine center.

Figure 2-26 Modern machine tool and process [45].

It should be noted that the application of direct drive motors has been one of the integrated features in the above new developments [43]. In the past, rotary axes were mostly driven by a motor with a speed reduction mechanism, such as a worm gear. However, these types of mechanisms exhibit large friction, backlash, and mechanical flexiblity. In contrast, direct drive motors have superior servo dynamic response, without the above drawbacks. They can achieve higher rotational speeds and accelerations

compared to using a geared transmission, thereby allowing higher feedrates and productivty in part machining. However, due to the absence of a speed reduction mechanism, the feed drive becomes more sensitive to the forces resulting from the coupled dynamics between axes, and the disturbances such as machining forces and friction. As a result, the study of the dynamics of multi-axis machines is a highly relevant and important topic at the moment, in the manufacturing and machine tool research community.

2.5 Multibody Dynamics

In the past, the motion of machining processes was rather slow, due to the spindle speeds also being lower (in the order of a few thousand rpm, rather than over 15 thousand RPM). Also, rotary axes were mostly driven by geared mechanisms. Thus, the net force in an individual axis is dominated by its inertia and friction, with coupling effects being strongly mitigated due to the gearing. Thus, the dynamics of each feed drive could reasonably be modeled independently.

However, in next generation machine tool design, as the factors illustrated in Section 2.4, the machine configuratrion is becoming more complex and diversified, and direct drive motors are more commonly used. Thus, the issue of coupled multibody dynamics in machine tools is gaining more attention and research importance. As studies on multibody dynamics in the field of machine tools are still relatively new, the review in this section focuses on the state-of-the-art in the field of robot manipulators.

2.5.1 Multi-Rigid-Body Dynamics

Both Newton-Euler equations and Euler-Lagrange equations are able to analyze the dynamics of a multi-axis feed drive [46]. Newton-Euler equations relate all the applied force and torque to the linear and angular momentum for each body. Thus, the internal constraint forces/torques for connecting the bodies have to be solved or eliminated during the computation. Additionally, each body is represented by its corresponding mass and complete inertia tensor. Therefore, all the parameters are required in order to formulate the equations.

On the other hand, in Euler-Lagrange equations, the system dynamics is described by generalized coordinates $\boldsymbol{q}$ and generalized forces $\boldsymbol{\tau}$**.** The Lagrangian L is defined as:

$$L(\boldsymbol{q}, \dot{\boldsymbol{q}}) = K(\boldsymbol{q}, \dot{\boldsymbol{q}}) - P(\boldsymbol{q}) \tag{2.7}$$

K is the system kinetic energy from the translational and rotational motion of all the bodies. P is the system potential energy. In rigid-body systems, only the gravity contributes the potential energy. Then, the equation of motion of the jth coordinate can be derived in terms of work and energy as:

$$\frac{d}{dt}\frac{\partial L}{\partial \dot{q}_j} - \frac{\partial L}{\partial q_j} = \tau_j \tag{2.8}$$

Considering an n-axis machine tool feed drive system, if all the joint variables are chosen as the generalized coordinates $\boldsymbol{q} = \{q_1, \dots, q_n\}^T$, the constraint forces for connecting bodies at the joints are in the orthogonal direction to the generalized coordinates (i.e., directions of movement). According to the principle of virtual work, this implies that the knowledge of constraint forces is not required in the analysis. Thus, the generalized forces can just include the joint actuator forces. Additionally, non-conservative forces, such as friction, can also be included in the generalized forces term. Then, Eq. (2.8) can be written into the form as:

$$\boldsymbol{M}(\boldsymbol{q})\ddot{\boldsymbol{q}} + \boldsymbol{C}(\boldsymbol{q}, \dot{\boldsymbol{q}})\dot{\boldsymbol{q}} + \boldsymbol{g}(\boldsymbol{q}) + \boldsymbol{\tau}_{\boldsymbol{fric}} = \boldsymbol{\tau} \tag{2.9}$$

$\boldsymbol{M}$ is the inertia matrix, which relates the mass and inertia in body-fixed frame to the generalized coordinates. So, $\boldsymbol{M}$ can be position-dependent. The centrifugal and Coriolis terms are included in $\boldsymbol{C}(\boldsymbol{q}, \dot{\boldsymbol{q}})\dot{\boldsymbol{q}}$, while $\boldsymbol{g}$ covers the gravity related terms. $\boldsymbol{\tau}_{\boldsymbol{fric}}$ is the friction term, which can be represented by linear viscous damping, nonlinear Coulomb friction, Stribeck friction or other model.

Newton-Euler equations vs. Euler-Lagrange equations

For the purpose of control and system identification, Lagrangian formulation provides advantages over Newton-Euler formulation, due to the following reasons [46]. First, it is convenient to consider the elastic deformations of the links, simply by adding the potential energy stored by the elastic deformation to the Lagrangian. Second, since unknown internal constraint forces are automatically eliminated, it yields closed-form equations explicitly describing the input-output relationship. Third, the equations of motion only include non-redundant parameters, also called '*base parameters*' or '*identifiable parameters*' [47], which are linear with respect to the equations. Therefore, it is convenient to reformulate the equations of motion into linear regression form to identify the unknown base parameters.

2.5.2 Multibody Dynamics Considering Mechanical Flexibility

In robot manipulators, there are numerous sources of flexibility such as gears and bearings at the joints, and the links. The joint flexibility is usually the dominant one. The modeling technique for the flexible joints and flexible links are introduced in the following section. It is noteworthy that a recent new application of robot manipulators is the machining operation [48][49][50][51]. Therefore, detailed studies related to the robot stiffness in different postures have been emerging recently [52][53].

Flexible Joint

In robot manipulators, the motor in each joint is often equipped with a gearbox in order to generate sufficient torque. The gear teeth usually contribute most of the elastic deformation among the whole structure. Such joint stiffness can be represented by a torsional spring which connects the motor shaft with the actuated link (i.e., robot arm) (see Figure 2-27) [54][55]. Then, the equations of motion Eq. (2.9) can be extended as:

$$\begin{cases} \boldsymbol{M}(\boldsymbol{q})\ddot{\boldsymbol{q}} + \boldsymbol{S}(\boldsymbol{q})\ddot{\boldsymbol{q}}_{\boldsymbol{m}} + \boldsymbol{C}(\boldsymbol{q},\dot{\boldsymbol{q}})\dot{\boldsymbol{q}} + \boldsymbol{g}(\boldsymbol{q}) + \boldsymbol{K}(\boldsymbol{q} - \boldsymbol{q}_{\boldsymbol{m}}) + \boldsymbol{D}(\dot{\boldsymbol{q}} - \dot{\boldsymbol{q}}_{\boldsymbol{m}}) = 0 \\ \boldsymbol{M}_{\boldsymbol{m}}\ddot{\boldsymbol{q}}_{\boldsymbol{m}} + \boldsymbol{S}^{T}(\boldsymbol{q})\ddot{\boldsymbol{q}} + \boldsymbol{K}(\boldsymbol{q}_{\boldsymbol{m}} - \boldsymbol{q}) + \boldsymbol{D}(\dot{\boldsymbol{q}}_{\boldsymbol{m}} - \dot{\boldsymbol{q}}) + \boldsymbol{\tau}_{\boldsymbol{fric}} = \boldsymbol{\tau}_{\boldsymbol{m}} \end{cases} \tag{2.10}$$

The usual notation in this thesis follows the textbook written by Shabana [56]. Besides the joint coordinates $\boldsymbol{q}$, the angular positions of motor shafts $\boldsymbol{q_m}$ are further introduced into the model. $\boldsymbol{M_m}$, $\boldsymbol{S}$, and $\boldsymbol{\tau_m}$ are the inertia of the motor shafts, coupling term, and the motor torque before transmitting to the link via the gearbox. $\boldsymbol{K}$ and $\boldsymbol{D}$ represent the stiffness and damping of the gearbox.

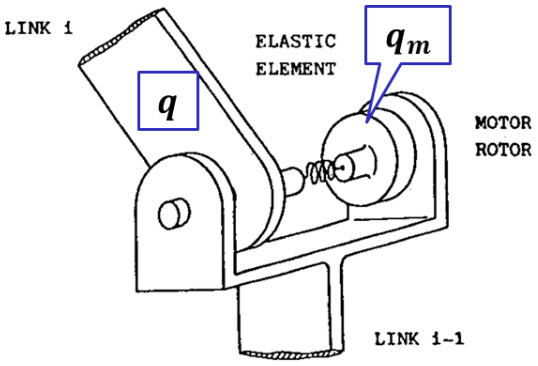

Figure 2-27 Flexible joint model [54].

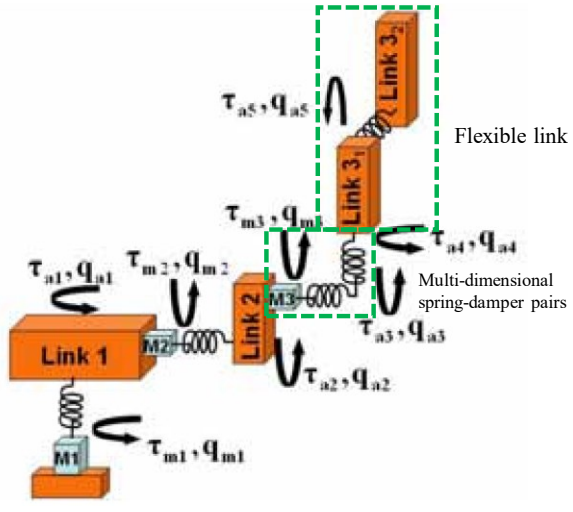

Figure 2-28 Extended flexible joints model [59].

Extended Flexible Joint

The flexibility of bearings and the machine frame could also be considered by extending the above model in the following ways [57][58][59] (see Figure 2-28). For example, the original uni-directional spring-damper pairs in the actuated joints can be replaced by multi-dimensional spring-damper pairs, in order to capture the deformation perpendicular to the rotation direction. A rigid link can be divided into several links connected by multi-dimensional spring-damper pairs to represent the bending of a link. However, determining these non-actuated joints at suitable location and orientation is challenging, which may require some understanding of the vibration characteristics in advance. In this thesis, this approach has been followed in Chapter 5-Chapter 7 for the estimation of a multibody feed drive model with inherent flexibility.

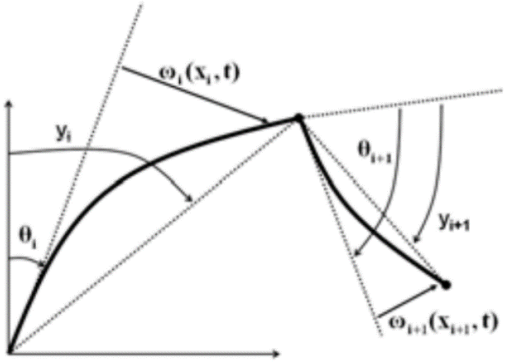

Figure 2-29 Flexible link model.

Flexible Link

The bending of the links could be represented by a distributed elasticity model, e.g. Euler–Bernoulli beam, which is described by partial differential equations with infinite dimension. In practical application, the dynamic equations are truncated to a finite dimension by the *'Assumed Mode Method'* [60][61]. As described by the assumed mode method in [58] and shown in Figure 2-29, for a system with N links, the bending deflection w_i at a location $x_i \in [0, l_i]$ along the ith link of length l_i, is represented by N_{ei} separable vibration modes φ_{ij} as:

$$w_i(x_i, t) = \sum_{j=1}^{N_{ei}} \varphi_{ij}(x_i)\delta_{ij}(t)\,, i = 1 \dots N \tag{2.11}$$

δ_{ij} are the generalized coordinates. Then, the equations of motion Eq. (2.9) can be extended as:

$$\begin{bmatrix} \boldsymbol{\tau_a} \\ 0 \end{bmatrix} = \begin{bmatrix} \boldsymbol{M}_{qq} & \boldsymbol{M}_{q\delta} \\ \boldsymbol{M}_{q\delta}^T & \boldsymbol{M}_{\delta\delta} \end{bmatrix} \begin{bmatrix} \ddot{\boldsymbol{q}} \\ \ddot{\boldsymbol{\delta}} \end{bmatrix} + \begin{bmatrix} \boldsymbol{C}_q \\ \boldsymbol{C}_\delta \end{bmatrix} + \begin{bmatrix} 0 \\ \boldsymbol{D}\dot{\boldsymbol{\delta}} + \boldsymbol{K}\boldsymbol{\delta} \end{bmatrix} \tag{2.12}$$

$\boldsymbol{\delta}$ includes all δ_{ij}. The assumption is that the vibration is relatively small. Deflection due to the vibration does not affect the joint location for large body motion. Therefore, the rigid body motion can be separated from the small vibration, and the same kinematic models as for the rigid or flexible joint model can be used. Finally, the deformed angular position y_i at the tip location l_i of the ith link is the combination of the rigid body motion and the deflection angle as:

$$y_i = q_i + \frac{1}{l_i}\left[\varphi_{i1}(l_i), \dots, \varphi_{iN_{ei}}(l_i)\right]\boldsymbol{\delta}_i \tag{2.13}$$

The assumed mode method is based on the beam theory which is suitable for robot manipulators because the geometry of the links could be simplified as beam structures. However, it may not be suitable for modeling the machine tool structure as the geometry is rather complex and irregular.

2.5.3 Parameter Identification for Multi-Rigid-Body Dynamics

The research history and the principle of parameter identification, applied predominantly to rigid-body based robot dynamics, is summarized in this section. Some of the methodology reviewed on this topic has been applied in Section 3.3 of this thesis.

In the late 80's, several pioneer researchers, such as Mayeda [47], Khosla [62], Atkeson [63], Gautier [64], and Olsen [65] initiated the research on parameter identification for robot dynamics. The relevant identification schemes are summarized in [66][67][68]. A general approach is described as follows.

First, the dynamic model in Eq. (2.9) is rearranged and expressed in linear form with respect to the parameters to be identified. As mentioned, the dynamic model derived by Lagrangian formulation yields the *base parameter* representation, convenient for parameter identification. Coulomb and viscous friction properties can also be added to the model since their parameters can also be incorporated into the equations in linear form [66].

The position and the input torque of each joint are sampled while executing an excitation trajectory. Then, an overdetermined linear system is constructed from the sampled data. The base parameters can be estimated by several methods, such as LS, weighted LS [69], extended Kalman filtering [70], or maximum-likelihood estimation [71]. Other potential estimation techniques can be found in [72].

To ensure that the system is fully excited, and that the sampled data is persistently exciting (i.e., informative) to identify the system, the command trajectory can be designed to minimize the condition number of the observation matrix by non-linear optimization methods. The excitation trajectory can be designed as a polynomial trajectory [73] or as a periodic Fourier series [71]. If the measured position signal is corrupted by noise and/or quantization error, when computing the velocity and acceleration by discrete differentiation, filtering techniques [69] are needed. Alternatively, the model can be derived from the energy approach [64][69] based on the principle of the applied mechanical energy equaling the sum of the kinetic and potential energy of the system. Such an energy model can avoid using joint accelerations.

2.5.4 Parameter Identification for Multibody Dynamics with Structural Flexibility

The identification of the robot flexibility is challenging and complex [59]. It is still an ongoing research topic. One of the reasons is that the encoder measurements at each joint only represent part of the states of the whole system. While model-based state observation is possible, when the model itself is the entity to be identified, accurate measurement of internal states becomes very important. Furthermore, the deflection of the flexible structure (e.g., link) is not directly detected. Also, the correctness of the identification relies on the assumed model structure, requiring significant mechanical flexibilities that contribute to vibratory behavior be identified ahead of time from modeling insight. Additionally, if nonlinear effects such as backlash, friction, nonlinear gear stiffness, etc. are considerable, then the frequency-domain identification approach and associated practices from modal analysis, which are based on the LTI assumption, cannot be directly adopted.

Table 2-1 Summary of the identification methods for robots with flexible joints.

	Time/frequency domain	Algorithm	Extra sensors	SISO/ MIMO
Albu-Schaffer et al. (2001) [74]	Freq.-domain	Nonlinear opt.	Torque sensor	SISO
Pham et al. (2001) [75]	Time-domain	LS	Extra encoder	SISO
Pham et al. (2002) [76]	Time-domain	LS	Gyro / accel.	SISO
Östring et al. (2003) [77]	Time-domain	Nonlinear opt.	N/A	SISO
Öhr et al. (2006) [78]	Freq.-domain	Nonlinear opt.	N/A	MIMO
Lightcap et al. (2007) [79]	Time-domain	LS	Marker & camera	MIMO
Oaki et al. (2009) [80]	Time-domain	Hybrid	Gyro / accel.	MIMO
Wernholt et al. (2011) [81]	Freq.-domain	Nonlinear opt.	N/A	MIMO
Moberg et al. (2014) [82]	Freq.-domain	Nonlinear opt.	Gyro / accel.	MIMO
Gaz et al. (2014) [83]	Time-domain	LS	Torque sensor	MIMO
Miranda et al. (2018) [84]	Time-domain	LS	Extra encoder	MIMO

In Table 2-1, the surveyed identification methods for robots with flexible joints are summarized. As seen, if employing extra sensors to capture missing variables, then identification by LS in the time domain becomes possible [75][76][79][80][83][84]. Otherwise, the model parameters have to be identified by nonlinear optimization methods, which are typically more time-consuming [77][78][81].

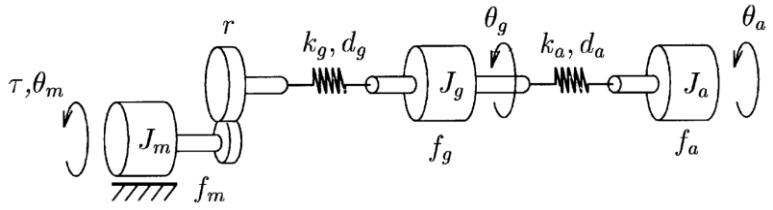

Figure 2-30 Three-mass flexible model for a single axis [77].

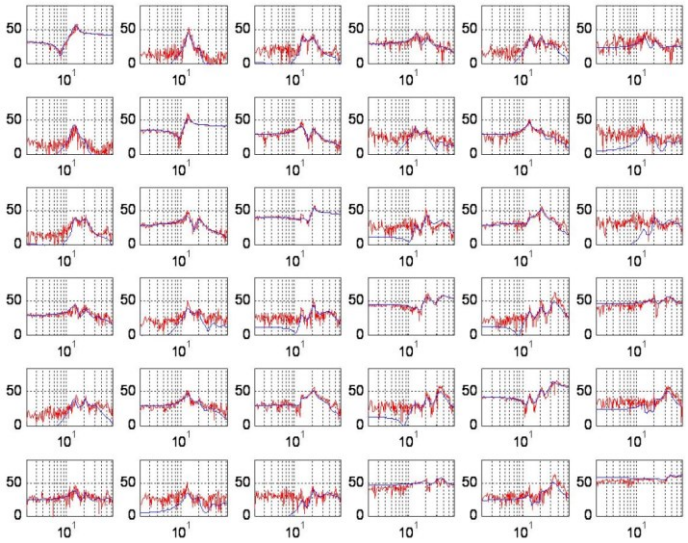

Figure 2-31 FRFs of a 6-axis manipulator, motor torque to motor acceleration [78].

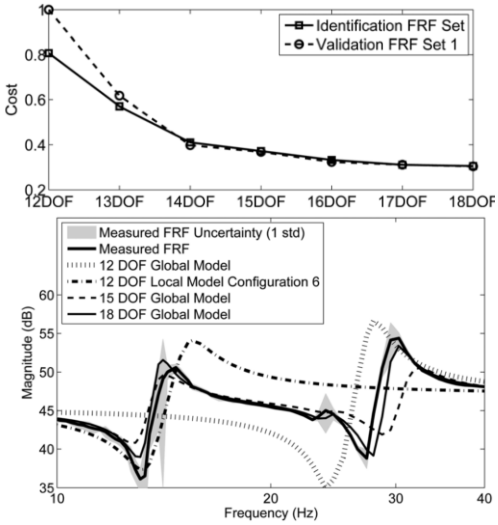

Figure 2-32 Identification based on different model structures [82].

In the earlier research, the stiffness of each joint was locally identified by moving one axis at a time. In such cases, each joint is assumed as a decoupled SISO model. For example, Figure 2-30 is a three-mass decoupled model capturing the flexibility of the gear and the arm of a single axis [77]. However, lateral flexibility and coupling effects are ignored in this approach. To circumvent this problem, Öhr et al. [78] performed a global MIMO identification in the frequency domain on a 6-axis manipulator. The measured and simulated frequency response functions (FRFs) are compared in Figure 2-31. The model considers the joint stiffness as well as unactuated bearing stiffness built by an extended flexible joint

model. Based on this approach, Moberg et al. [82] further investigated the influence of considering different numbers of extended flexible joints on the fitting of the cost function (see Figure 2-32).

Regarding the use of additional motion sensors, as demonstrated in Figure 2-33, the deflection of the links can be measured by extra encoders mounted externally [75][84][85]. However, such sensor installation is sometimes impractical. Hence, gyroscopes or accelerometers are used [76][80][82] to capture the motion of the links or the end effectors. Alternatively, the torque transmitted to the links can be measured by torque sensors [74][83]. This information can also help identify the model.

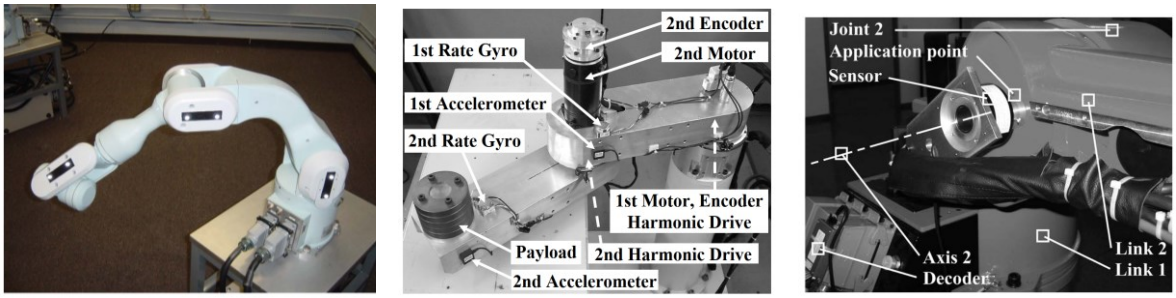

(a) Passive markers motion camera system [79]. **(b) Accelerometer & gyro sensors [80].** **(c) Extra Encoder mounted externally [85].**

Figure 2-33 Identification with extra motion sensors.

Another concept to evaluate the stiffness of flexible robots is via Cartesian stiffness matrix [48]. It measures the joint's deflection as well as the translational and rotational displacements at the end-effector location with given applied forces and torques [86][87]. Such approach aims to correlate the stiffness at the end-effector with the stiffness at joints by the kinematic Jacobian matrix.

2.6 3D Motion Sensing for Precision Engineering

The research goal of this thesis is to build a machine model which is able to predict the tool-end and/or table-end motion, including vibration and rigid body motion in 3D space. However, the embedded encoder sensors for feedback control can only detect the motion at the encoder's mounting location. The vibration in other locations is unknown. In order to capture this additional motion, extra sensors are required. Section 2.6.1 presents a survey on the available candidate sensors, and Section 2.6.2 introduces MEMS IMUs, the auxiliary sensor adopted in this research. Such IMUs also require adequate sensor fusion, which is discussed in Section 2.6.3.

2.6.1 A Survey on Candidate Position Sensors

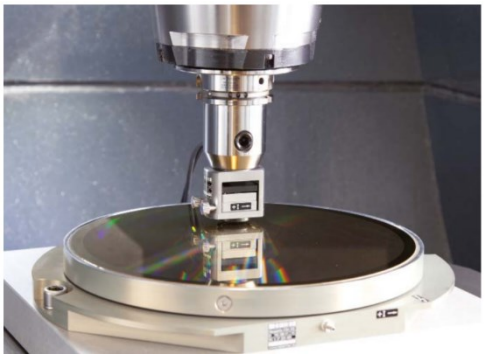

Figure 2-34 Grid encoder (KGM) [89].

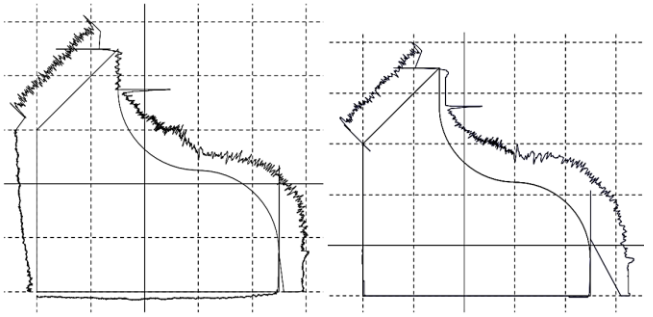

Figure 2-35 Contouring error measured by KGM (left) and position feedback signal (right) [90].

A wide range of sensing technologies have been applied for precision positioning [88]. In machine tools, capacitive, eddy current, and inductive sensors are not applicable due to the limited measuring range, e.g. a few millimeters. Laser interferometers are capable of long-range measurement, e.g. tens of meters, but limited to one dimension at a time. In the machine tool industry, grid encoders (KGM) (see Figure 2-34) are mainly applied for testing contouring accuracy [89][90] in 2D planar motion. Figure 2-35 shows different contour errors measured by KGM and the position sensor for feedback control. It also demonstrates the necessity of using additional sensors for capturing the tool-workpiece relative motion more accurately, which cannot otherwise be picked by the servo feedback position encoders. Law et al. [91] applied high frame rate cameras to measure machine tool vibrations. However, this method is also confined to planar motion, unless stereoscopic vision is used, and requires dedicated image processing techniques.

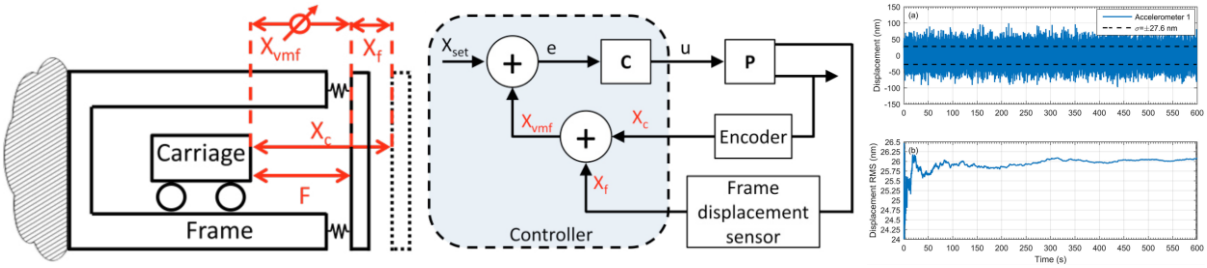

Figure 2-36 Accelerometer assisted position feedback control [92].

Abir et al. [92] use an IEPE (Integrated Electronics Piezo-Electric) accelerometer to capture the relative vibration of the machine frame (see Figure 2-36). An IEPE accelerometer is excellent in capturing vibration. However, it cannot accurately capture rigid body motion, due to its inherent behavior as a

high-pass filter. In the next section, IMUs (Inertial Measurement Units) are specifically introduced since it is more suitable for sensing rigid body motion in space.

2.6.2 Introduction to MEMS IMUs

An IMU (Inertial Measurement Unit) is an integrated sensor consisting of a triaxial accelerometer and a triaxial gyroscope, which together measure linear accelerations and angular velocities. The motion orientation can then be estimated by the measured information [93][94]. IMUs have been widely used in many applications, such as aircraft navigation, automobiles, control of mobile robots, locomotion recognition, etc. They have also has been integrated in cellphones for more functionalities. Regarding machine tool applications, IMUs have not yet been widely applied to this field. Vogl et al. [95] used an IMU as metrology equipment to inspect the positioning error of a feed drive (see Figure 2-37), investigating the practicality of replacing a laser interferometer system which is typically used for long measurement tasks.

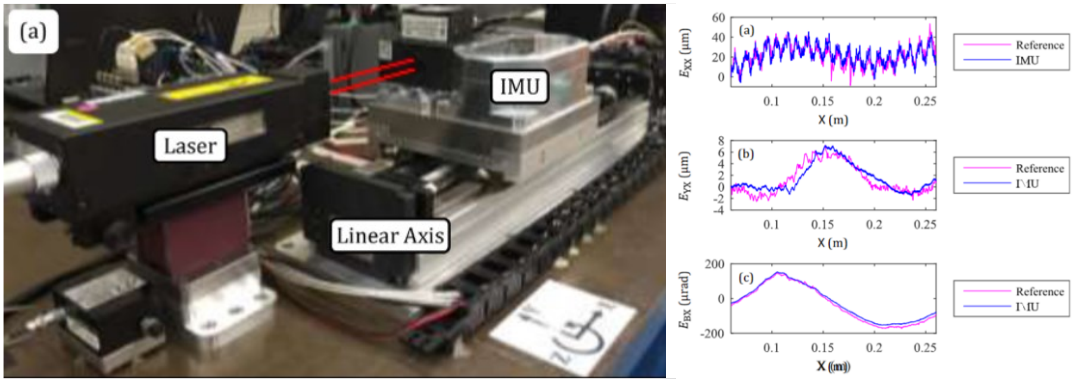

Figure 2-37 Positioning error inspected by IMU [95].

The behavior of angle random walk and bias instability are the main key performance metrics of an IMU [94][96]. There are a variety of IMUs designed for different applications (see Figure 2-38), and the size and price are typically inversely proportional to the performance. High performance (military grade) gyroscopes can be achieved by optical gyroscopes which are based on the Sagnac effect [98]. When two laser beams are travelling along the same path but in opposite directions, a rotational motion can cause a phase difference between the laser beams. However, optical gyroscopes, whether they are ring laser gyroscopes (RLG) or fiber-optic gyroscopes (FOG), are bulky and extremely expensive. Hence, they are primarily only applied to aircraft navigation.

Figure 2-38 IMU product line, Honeywell [97].

On the other hand, IMUs made by Microelectromechanical system (MEMS) technology are relatively small, lightweight, and inexpensive [93]. Over the past decade, the performance of MEMS IMUs has improved significantly. Following this trend, it can be anticipated that more applications will emerge in the future.

The principle of MEMS gyroscopes is based on the Coriolis effect, where oscillating masses during a rotational motion induce a Coriolis force. MEMS gyroscopes sense the corresponding changes of capacitance. MEMS accelerometers also sense capacitance change due to the structural deflection caused by the inertial force.

Regarding the frequency response of MEMS accelerometers and gyroscopes, they can measure 0 Hz motion such that gravity and constant acceleration are included in the measurement. The maximum bandwidth is however only up to a few hundred hertz [99]. Therefore, MEMS accelerometers and gyroscopes are only suitable for measuring motion with low frequency content. This is successful in capturing rigid body motion and structural vibrations of machine tools which lie in this range.

2.6.3 Sensor Fusion for Orientation Estimation

Orientation computation is very important for interpreting the IMU signals correctly. This can be achieved by numerically integrating the measured angular velocities. This step is also called ‘strapdown integration’. The main error sources for strapdown integration are angle random walk (ARW) and the bias instability of a gyroscope. ARW is the accumulated angular error due to the integration of

uncorrelated white noise. Bias instability refers to the random variation of the bias over time. These errors are further propagated in the acceleration estimation, when extracting the gravity portion from the measured acceleration.

These errors can be reduced by sensor fusion, which estimates the sensor orientation by fusing the information from multiple sensors and/or prediction. For example, the inclination (the orientation except the rotation around the gravity vector, i.e., the pitch and roll angle) can be corrected by accelerometers which measure the gravity direction. If integrating a triaxial magnetometer, the measured magnetic field can help correct the heading direction (yaw angle). However, magnetic field measurement can be significantly affected by local magnetic disturbances, e.g., servo motors. Hence, magnetometers are not applicable to the machine tool application.

Due to the significant improvement of MEMS IMUs over the past two decades, an extensive effort has also been made to develop orientation estimation techniques. Well-known and published sensor fusion algorithms for IMUs are summarized in Table 2-2 and discussed in the following.

Table 2-2 Summary of sensor fusion algorithms for IMUs.

	Orientation	Fusion algorithm	Bias estimation	Body acc. rejection scheme
Rehbinder et al. (2004) [100]	DCM	KF	No	Yes
Luinge et al. (2005) [101]	DCM	IKF	Accel. & gyro.	Yes
Sabatini (2006) [102]	Quaternions	KF	Accel. only	Yes
Suh (2010) [103]	Quaternions	IKF	Accel. & gyro.	Yes
Yoo et al. (2011) [104]	Euler angle	CF	No	Yes
Lee et al. (2012) [105]	Euler angle	KF	No	Yes
Valenti et al. (2015) [106]	Quaternions	CF	No	Yes

KF: Kalman filter, IKF: indirect Kalman filter, CF: complementary filter

Orientation expressions: As can be seen from the table, numerous equivalent expressions of the orientation [107] are employed. Euler angles is a sequence of three rotation angles, which are easy to denote and understand. However, this representation sometimes is not unique, and may lead to singularity condition, i.e., gimbal lock. In contrast, direction cosine matrix (DCM) and quaternions are robust, mathematically. A DCM is a three-by-three matrix; a quaternion contains one scalar and a three-dimensional vector, i.e. four parameters in total, which is more efficient than DCM. In particular, a quaternion is a linear formulation of the orientation, which, for example, is commonly used when developing extended Kalman filters [102].

Fusion algorithms: Three types of fusion algorithms are shown in Table 2-2. Non-model-based filters such as complementary filters, Mahony filter [108], and Madgwick filter [109] are computationally efficient, which favors the use of low-cost processors. However, complementary filters are generally not capable of dynamically estimating sensor biases and adjusting gains with respect to the nonlinear orientation kinematics. These drawbacks can be addressed by a model-based filter, i.e., Kalman filter, treating sensor biases as additional states in the system model. A typical Kalman filter implementation first predicts the orientation by the gyroscope output, and then corrects the predicted orientation using the accelerometer output. In contrast, an indirect Kalman filter estimates the error of orientation prediction. The estimated orientation is later obtained by this error estimation.

Body acceleration rejection scheme: Another critical issue is to consider and reject the body (sensor) acceleration. When a body, where an IMU is attached, is subject to high accelerations, the orientation derived from accelerometer outputs is no longer accurate. Numerous strategies have been proposed (see Table 2-2). However, there is still no perfect solution to distinguish the body acceleration from the gravity among the accelerometer outputs. A general concept of all the proposed schemes is that it modulates the gains or switches the models with respect to the magnitude of the sensed acceleration. Therefore, when high acceleration is detected, orientation estimation relies mainly on the gyroscope outputs and bypasses the information from the accelerometers. When the sensor is at rest, more weighting is provided on the accelerometer measurement. Hence, even employing the current state-of-the-art techniques, it is important to recognize that motion estimation for only short period acceleration periods is acceptable, due to accumulating drift. However, during each ‘rest’ position (which happens frequently in machine tools), the fusion algorithm can be reset and another packet of short movement can be monitored and estimated correctly.

Another point to keep in mind is that the sensor fusion algorithm is just one contribution to the overall accuracy of an IMU. In addition, the design of the micro-structure, fabrication quality, signal processing pipeline from analog to digital signals, calibration for misalignment and temperature effect, etc. are all important factors which influence the accuracy of such a highly integrated measurement device [110].

2.7 Conclusions

This chapter has presented a survey of the literature and current state-of-the-art industrial practices in modeling and identification of multi-axis machine tool and robot servo systems, including effects such as the control law, the friction and vibrations. Review of foundational theory in multibody dynamics is

also conducted, and the utilization of auxiliary motion sensors in the measurement of the dynamic response, which cannot be accurately detected by the servo control system's own sensors, is discussed. Building on this knowledge, the proceeding chapters present the accomplished research in this dissertation.

Chapter 3
Identification of Open-Loop Dynamics of Multi-Axis Feed Drives

3.1 Introduction

Understanding the structure of open-loop dynamics of the feed drive, i.e., the plant in a control system, is a fundamental step prior to building the model of the entire feed drive closed-loop control system in the next chapter. This chapter elaborates the procedure of the parameter identification for the open-loop dynamic model.

An industrial 5-axis laser drilling machine is studied in this chapter. In Section 3.2, the open-loop dynamic model of the feed drive assembly is derived according to the machine configuration and characteristics. Section 3.3 presents the parameter identification via linear Least Squares (LS) with nonlinear optimization approach. Section 3.4 presents the experimental results. In the next chapter, the identification of the closed-loop control system will incorporate the results of this chapter.

3.2 Open-Loop Dynamic Model of Multi-Axis Feed Drives

The machine studied here is a 5-axis laser drilling machine. It can drill and penetrate holes by delivering laser pulses from the nozzle to the workpiece. Integrated with a 5-axis positioning configuration, holes on freeform shaped parts along any orientation can be drilled. Such a drilling process is applied in the aerospace manufacturing industry.

The machine configuration is shown in Figure 3-1. The X and Y axes are placed on top of the machine frame to support the laser nozzle, while the Z, B, and C axes form a serial kinematic chain as shown in Figure 3-2. Considering the characteristics of machine dynamics, the following assumptions are made:

1. The X and Y axes can be simply assumed as independent decoupled feed drives, due to their orthogonal configuration.
2. In contrast, the Z, B, and C axes form a serial kinematic chain where the rotary axes make the kinematics and dynamics inherently coupled and nonlinear.
3. It is given that the X, Y, B and C axes are all driven by direct drive motors. Therefore, substantial position-dependent force/torque ripples, acting as disturbances, should be taken into account.

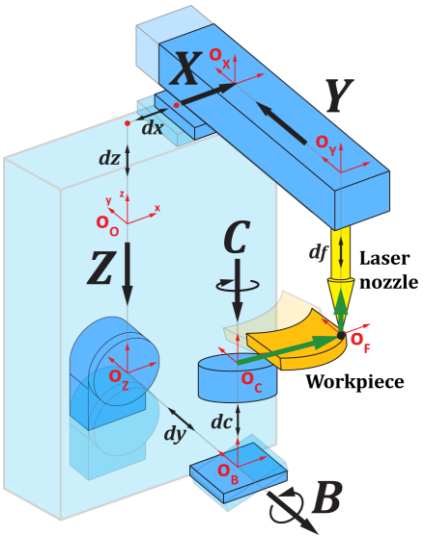

Figure 3-1 Machine kinematic diagram.

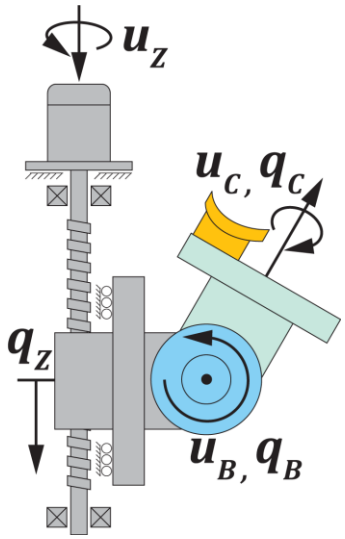

Figure 3-2 Z-B-C kinematic chain.

The dynamic equations for each axis are derived as follows. To make the equations easier to read, each characteristic is denoted in respective color as the sample equation Eq. (3.1).

$$u_i = Multibody\ dynamics + viscous\ damping + Stribeck\ friction + ripple \tag{3.1}$$

X-axis:

$$u_X = M_X\ddot{q}_X + V_X\dot{q}_X + C_X sign(\dot{q}_X) + S_X sign(\dot{q}_X)e^{-|\dot{q}_X/vs_X|} + R_X \sin(\omega_{r_X} q_X + \phi_{r_X}) \tag{3.2}$$

Y-axis:

$$u_Y = M_Y\ddot{q}_Y + V_Y\dot{q}_Y + C_Y sign(\dot{q}_Y) + S_Y sign(\dot{q}_Y)e^{-|\dot{q}_Y/vs_Y|} + R_Y \sin(\omega_{r_Y} q_Y + \phi_{r_Y}) \tag{3.3}$$

Z-axis:

$$\begin{aligned} u_Z = {} & (M_Z + M_B + M_C + M_W + M_{SC})\ddot{q}_Z + (M_Z + M_B + M_C + M_W)(-g) \\ & + (r_C M_C + z_W M_W + r_C M_W - r_B M_B)\left(cos(q_B)\,\dot{q}_B{}^2 + sin(q_B)\,\ddot{q}_B\right) \\ & + y_W M_W\left(-2\,cos(q_B)\,cos(q_C)\,\dot{q}_B\dot{q}_C + \left(\dot{q}_B{}^2 + \dot{q}_C{}^2\right)sin(q_B)\,sin(q_C)\right. \\ & \left. - sin(q_B)\,cos(q_C)\,\ddot{q}_C - cos(q_B)\,sin(q_C)\,\ddot{q}_B\right) \\ & + x_W M_W\left(2\,cos(q_B)\,sin(q_C)\,\dot{q}_B\dot{q}_C + \left(\dot{q}_B{}^2 + \dot{q}_C{}^2\right)sin(q_B)\,cos(q_C)\right. \\ & \left. + sin(q_B)\,sin(q_C)\,\ddot{q}_C - cos(q_B)\,cos(q_C)\,\ddot{q}_B\right) + V_Z\dot{q}_Z + C_Z sign(\dot{q}_Z) \\ & + S_Z sign(\dot{q}_Z)e^{-|\dot{q}_Z/vs_Z|} \end{aligned} \tag{3.4}$$

B-axis:

$$
\begin{aligned}
u_B = {} & \left(I_{Byy} + I_{Cxx} + I_{Wxx} + M_C {r_C}^2 + M_B {r_B}^2 + M_W {y_W}^2 + M_W {z_W}^2 + M_W {r_C}^2 \right. \\
& \left. + 2M_W r_C z_W\right)\ddot{q}_B + (r_C M_C + z_W M_W + r_C M_W - r_B M_B)(\ddot{q}_Z - g)\sin(q_B) \\
& + (-I_{Wzx} + M_W r_C x_W + M_W x_W z_W)\left({\dot{q}_C}^2 \cos(q_C) + \ddot{q}_C \sin(q_C)\right) \\
& + \left(I_{Wxy} - M_W x_W y_W\right)(2\dot{q}_B \dot{q}_C - 2\ddot{q}_B \cos(q_C)\sin(q_C) \\
& - 4\cos(q_C)^2 \dot{q}_B \dot{q}_C) \\
& + \left(I_{Wyz} - M_W r_C y_W - M_W y_W z_W\right)\left(\ddot{q}_C \cos(q_C) - {\dot{q}_C}^2 \sin(q_C)\right) \\
& + \left(I_{Wxx} - I_{Wyy} - M_W {x_W}^2 + M_W {y_W}^2\right)(2\cos(q_C)\sin(q_C)\dot{q}_B \dot{q}_C \\
& - \cos(q_C)^2 \ddot{q}_B) + M_W y_W (g - \ddot{q}_Z)\cos(q_B)\sin(q_C) \\
& + M_W x_W (g - \ddot{q}_Z)\cos(q_B)\cos(q_C) + V_B \dot{q}_B + C_B sign(\dot{q}_B) \\
& + S_B sign(\dot{q}_B) e^{-|\dot{q}_B / vs_B|} \\
& + R_B\left(1 + \alpha_B \left|\sin\left(q_B + \varepsilon_{r_B}\right)\right|\right)\sin\left(\omega_{r_B} q_B + \phi_{r_B}\right)
\end{aligned}
\tag{3.5}
$$

C-axis:

$$
\begin{aligned}
u_C = {} & \left(I_{Czz} + I_{Wzz} + M_W {x_W}^2 + M_W {y_W}^2\right)\ddot{q}_C + \left(I_{Wxy} - M_W x_W y_W\right)(2\cos(q_C)^2 - 1){\dot{q}_B}^2 \\
& + (-I_{Wzx} + M_W r_C x_W + M_W x_W z_W)\ddot{q}_B \sin(q_C) \\
& + \left(I_{Wyz} - M_W r_C y_W - M_W y_W z_W\right)\ddot{q}_B \cos(q_C) \\
& + \left(I_{Wxx} - I_{Wyy} - M_W {x_W}^2 + M_W {y_W}^2\right)\left(-\sin(q_C)\cos(q_C){\dot{q}_B}^2\right) \\
& + M_W y_W (-\ddot{q}_Z + g)\sin(q_B)\cos(q_C) + M_W x_W (\ddot{q}_Z - g)\sin(q_B)\sin(q_C) \\
& + V_C \dot{q}_C + C_C sign(\dot{q}_C) + S_C sign(\dot{q}_C) e^{-|\dot{q}_C / vs_C|} \\
& + R_C\left(1 + \alpha_C \left|\sin\left(q_C + \varepsilon_{r_C}\right)\right|\right)\sin\left(\omega_{r_C} q_C + \phi_{r_C}\right)
\end{aligned}
\tag{3.6}
$$

The parameters shown in the above dynamic equations are categorized in Table 3-1.

Table 3-1 Parameters of the dynamic model.

Type	Notation	Description
Multibody	$M_X, M_Y, M_Z, M_B, M_C, M_W, M_{SC}$	Mass of each axis, workpiece, and equivalent mass of the Z-axis ball screw
	r_B, r_C, x_W, y_W, z_W	Location of the center of mass
	I_{Byy}, I_{Cxx}, I_{Czz}, I_{Wxx}, I_{Wyy}, I_{Wzz}, I_{Wzx}, I_{Wxy} I_{Wyz}	Inertia of each axis and workpiece
Friction	V_X, V_Y, V_Z, V_B, V_C	Viscous damping coefficient
	C_X, C_Y, C_Z, C_B, C_C	Coulomb friction coefficient

	S_X, S_Y, S_Z, S_B, S_C	Stribeck friction coefficient
	$vs_X, vs_Y, vs_Z, vs_B, vs_C$	Friction velocity coefficient
Ripple	R_X, R_Y, R_Z, R_B, R_C	Ripple magnitude
	$\omega_{r_X}, \omega_{r_Y}, \omega_{r_B}, \omega_{r_C}$	Ripple frequency
	$\phi_{r_X}, \phi_{r_Y}, \phi_{r_B}, \phi_{r_C}$	Ripple phase
	α_B, α_C	Ripple magnitude 2
	$\varepsilon_{r_B}, \varepsilon_{r_C}$	Ripple phase 2

The open-loop dynamics in Eqs. (3.2)-(3.6), can be rearranged into a general matrix form:

$$\boldsymbol{u} = \boldsymbol{M}(\boldsymbol{q})\ddot{\boldsymbol{q}} + \boldsymbol{h}(\boldsymbol{q}, \dot{\boldsymbol{q}}) + \boldsymbol{C}\dot{\boldsymbol{q}} + \boldsymbol{u}_f(\dot{\boldsymbol{q}}) + \boldsymbol{u}_p(\boldsymbol{q}) \tag{3.7}$$

Above, $\boldsymbol{M}(\boldsymbol{q})$ and $\boldsymbol{C}$ are the mass and viscous damping matrices, respectively. $\boldsymbol{h}(\boldsymbol{q}, \dot{\boldsymbol{q}})$ is the vector containing the Coriolis, centrifugal, and gravitational terms. $\boldsymbol{u}_f(\dot{\boldsymbol{q}})$ and $\boldsymbol{u}_p(\boldsymbol{q})$ are nonlinear friction and position-dependent ripples, respectively. $\boldsymbol{q}$ represents the measured position or angle of each drive. $\boldsymbol{u}$ is the measured motor current, which can be viewed as the equivalent motor force/torque related by the motor constant. Components of this equation can be broken down into the categories outlined below.

Multi-Rigid-Body Dynamics

The equations of multibody dynamics can be derived using the Euler-Lagrange equations. Alternatively, to avoid making mistakes in the derivation by hand, MapleSim, which is based on graph theory [111], can be applied to deriving the equations systematically. The multibody dynamics is depicted by $\boldsymbol{M}(\boldsymbol{q})$ and $\boldsymbol{h}(\boldsymbol{q}, \dot{\boldsymbol{q}})$, which are coupled and nonlinear due to the nature of Z-B-C-axis serial kinematic chain (see Figure 3-2).

Joint Friction

Friction at joints includes linear viscous damping $\boldsymbol{C}\dot{\boldsymbol{q}}$ and nonlinear friction $\boldsymbol{u}_f(\dot{\boldsymbol{q}})$. Coulomb friction, and Stribeck effect are considered in the nonlinear friction model. For the ith axis, the nonlinear friction u_{f_i} can be described as:

$$u_{f_i} = d_{n_i}(\dot{q}_i)\left[C_i + S_i e^{-|\dot{q}_i/vs_i|}\right] \tag{3.8}$$

The associated parameters, C_i, S_i, and vs_i are described in Table 3-1.

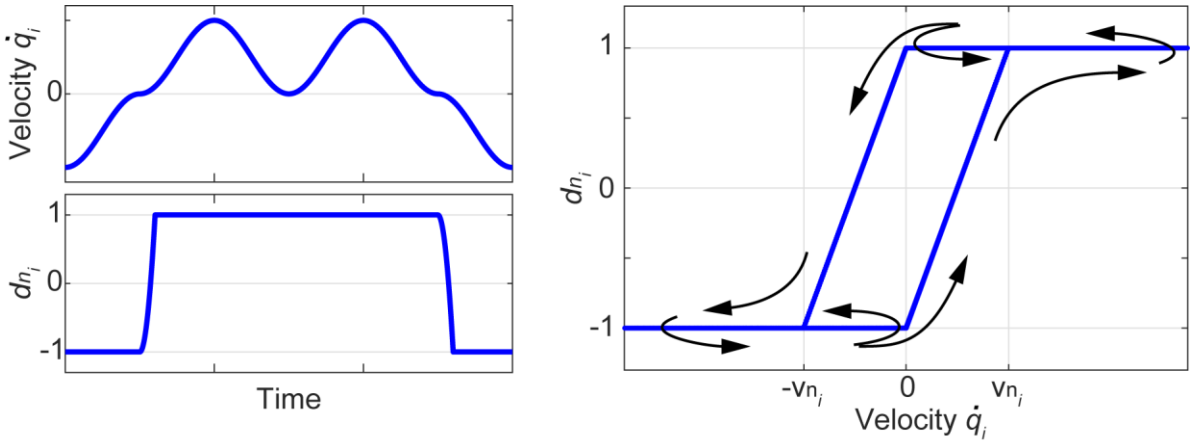

(a) Normalized friction vs. time **(b) Normalized friction vs. velocity.**

Figure 3-3 Normalized friction for the *i*th axis.

$d_{n_i}(\dot{q}_i)$ in Eq. (3.8) can be a saturation function [7] or a hyperbolic function [28] to describe a smooth transition of friction forces around zero velocity, such that numerical problems at pre-sliding region could be avoided. This thesis presents a model integrating a saturation function with a relay function shown below. At the *k*th discrete time step,

If: $sign(\ddot{q}_{i_k}) \times sign(\dot{q}_{i_k}) == -1$

$$d_{n_k} = d_{n_{k-1}} \tag{3.9}$$

Else:

$$d_{n_k} = sat_{-1}^{1}(d_{n_{k-1}} + (\dot{q}_{i_k} - \dot{q}_{i_{k-1}})/v_{n_i})$$

An example of this friction model is demonstrated in Figure 3-3. The output is bounded within ± 1 and C^1-continuous within a small velocity band, $\pm v_{n_i}$. Comparing to the conventional sign function with discontinuous binary outputs, 1 or -1, such feature can help avoid numerical noise and limit cycles when running simulation.

Due to the relay concept, it captures the effect that the friction remains constant if the feed drive stops momentarily and then moves toward the same direction, as shown in Figure 3-3 (a). This feature well-describes the friction behavior of an actual feed drive. Although the proposed normalized friction may not be the most accurate model for describing friction around near-zero velocity [35], the proposed mathematical simplification was observed to yield simpler parameter identification, better computational efficiency, and still, sufficient modeling fidelity.

Force/Torque Ripple

Direct drive motors exhibit substantial position-dependent ripple acting as an external disturbance. For the ith axis, the ripple can be described as:

$$u_{p_i} = R_i\left(1 + \alpha_{r_i}\left|sin\left(q_i + \varepsilon_{r_i}\right)\right|\right) sin\left(q_i\omega_{r_i} + \phi_{r_i}\right) \tag{3.10}$$

R_i , ω_{r_i} , and ϕ_{r_i} are the magnitude, frequency, and the phase of the ripple. The term $\left(1 + \alpha_{r_i}\left|sin\left(q_i + \varepsilon_{r_i}\right)\right|\right)$ is particularly included into the model to capture the effect of the imperfect motor assembly. In the case of linear (translational) motors, this term would be discarded.

Position-Dependent Disturbance Model by Lookup Table with Linear Interpolation

In some cases, the force/torque ripple cannot be accurately depicted by an ideal sinusoidal equation as Eq. (3.10). Additionally, there are other position-dependent disturbances. For example, the tension force from the motor cables and the varying guideway disturbance due to imperfect assembly are both position-dependent. Exact analytical expressions for the above disturbances may not exist. The author proposes a model based on a discrete lookup table, which can accommodate the position-dependent disturbances with any kind of distribution.

The traveling range of the ith axis is discretized into N_{g_i} grids with the size l_{g_i}. The grids should be sufficiently fine to describe the disturbance variation along the ith axis. The position-dependent disturbance u_{p_i} is defined as follows.

$$\begin{aligned} &\forall\, k \in 1, \dots, N_{g_i} \\ &If: \left|p_{k_i} - q_i\right| < l_{g_i}, then: w_{k_i} = 1 - \frac{\left|p_{k_i} - q_i\right|}{l_{g_i}} \\ &Else: w_{k_i} = 0 \end{aligned} \tag{3.11}$$

$$u_{p_i} = \sum_{k=1}^{N_{g_i}} m_{k_i} w_{k_i}$$

Above, m_{k_i} is disturbance magnitude coefficient for the kth grid at position p_{k_i}. w_{k_i} is the positional weighting factor. m_{1_i} … $m_{N_{g_{ii}}}$ are the parameters that have to be identified. w_{1_i} … $w_{N_{g_{ii}}}$ are dependent variables determined by the feed drive's location q_i.

To illustrate this idea, an example is shown in Figure 3-4. The position of the ith axis q_i is located between p_{k_i} and p_{k+1_i}. In this case, $w_{k_i} = 0.4$ and $w_{k+1_i} = 0.6$. The disturbance is calculated as $u_{p_i} = m_{k_i} \times 0.6 + m_{k+1_i} \times 0.4$.

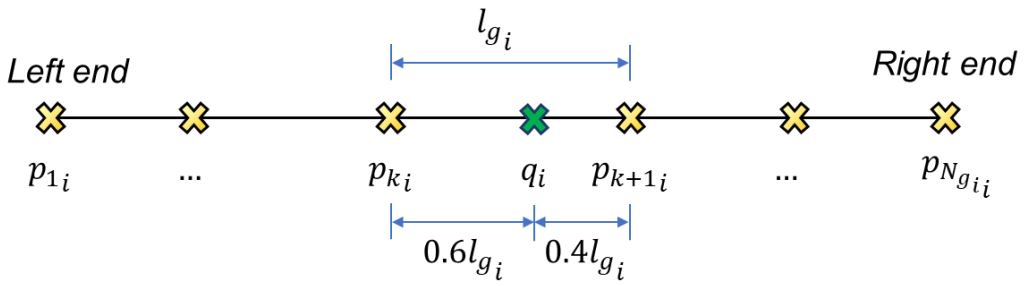

Figure 3-4 Example of position-dependent disturbance by lookup table with linear interpolation.

To achieve desirable modeling resolution, fine grids are required. This might result in an enormous number of parameters in this model. However, this is not a problem, since all the parameters $(m_{1_i}, \dots, m_{N_{g_{i_i}}})$ are linear with respect to the position variable $(w_{1_i}, \dots, w_{N_{g_{i_i}}})$. Therefore, they can be efficiently estimated by linear LS. In contrast, the force/ripple model proposed in Eq. (3.10) contains only three parameters. However, the three parameters are nonlinear and thus require nonlinear estimation techniques, leading to much higher computational cost.

This model has been applied for the case study in Section 4.3.2, whereas the case study in this chapter has used the sinusoidal force/torque ripple model in Eq. (3.10).

3.3 Parameter Identification

The strategy of parameter identification in this research has considered the accuracy of the model, the efficiency of the computation, and the feasibility for industrial implementation. Hence, the proposed identification strategy illustrated in this section has several features.

(a) Considering the feasibility for industrial implementation, the data for the identification were collected during the manufacturing process, such that the production was not interrupted.

(b) Considering model fidelity, numerous dynamic effects were included in the model, e.g., multibody dynamics, nonlinear friction, and force/torque ripple.

(c) Considering accuracy and efficiency, the parameters were identified via a tandem strategy combining linear Least Squares (LS) with nonlinear optimization.

On-the-Fly Data Collection and Data Selection

The above dynamic models are intended to be identified using the data of the measured servo position and the motor current of all the five axes collected during a real laser drilling process.

The laser drilling toolpath contains a large number of simultaneous 5-axis movements, generating rich data for model identification. The low velocity and acceleration components of the motion are less informative for identifying the inertia parameters. However, the friction phenomenon during the low velocity motion (in pre-sliding regime) is time-dependent. Considering the above issues, only the collected data with high-velocity or high-acceleration were selected by a velocity and acceleration threshold.

Parameter Identification of Open-Loop Dynamics

In order to identify parameters by a combination of linear Least Squares (LS) and nonlinear global optimization, Eqs. (3.2)-(3.6) should be first examined and expressed as the following equations. In the following, P_j^i and Q_j^i denote parameters which appear as linear and nonlinear terms, respectively. These are henceforth referred to as 'linear parameters', and 'nonlinear parameters'.

X-axis:

$$u_X = P_1^X \ddot{q}_X + P_2^X \dot{q}_X + P_3^X sign(\dot{q}_X) + P_4^X sign(\dot{q}_X) e^{-|\dot{q}_X / Q_1^X|} + P_5^X \sin(Q_2^X q_X + Q_3^X) \tag{3.12}$$

Y-axis:

$$u_Y = P_1^Y \ddot{q}_Y + P_2^Y \dot{q}_Y + P_3^Y sign(\dot{q}_Y) + P_4^Y sign(\dot{q}_Y) e^{-|\dot{q}_Y / Q_1^Y|} + P_5^Y \sin(Q_2^Y q_Y + Q_3^Y) \tag{3.13}$$

Z-axis:

$$\begin{aligned} u_Z = {} & P_1^Z \ddot{q}_Z + P_2^Z + P_3^Z \left(cos(q_B)\, \dot{q}_B{}^2 + sin(q_B)\, \ddot{q}_B \right) \\ & + P_4^Z \left(-2\, cos(q_B)\, cos(q_C)\, \dot{q}_B \dot{q}_C + \left(\dot{q}_B{}^2 + \dot{q}_C{}^2 \right) sin(q_B)\, sin(q_C) \right. \\ & \left. - sin(q_B)\, cos(q_C)\, \ddot{q}_C - cos(q_B)\, sin(q_C)\, \ddot{q}_B \right) \\ & + P_5^Z \left(2\, cos(q_B)\, sin(q_C)\, \dot{q}_B \dot{q}_C + \left(\dot{q}_B{}^2 + \dot{q}_C{}^2 \right) sin(q_B)\, cos(q_C) \right. \\ & \left. + sin(q_B)\, sin(q_C)\, \ddot{q}_C - cos(q_B)\, cos(q_C)\, \ddot{q}_B \right) + P_6^Z \dot{q}_Z + P_7^Z sign(\dot{q}_Z) \\ & + P_8^Z sign(\dot{q}_Z) e^{-|\dot{q}_Z / Q_1^Z|} \end{aligned} \tag{3.14}$$

B-axis:

$$
\begin{aligned}
u_B = {} & P_1^B \ddot{q}_B + P_2^B (\ddot{q}_Z - g)\, sin(q_B) + P_3^B \left(\dot{q}_C{}^2 \cos(q_C) + \ddot{q}_C \sin(q_C)\right) \\
& + P_4^B (2\dot{q}_B \dot{q}_C - 2\ddot{q}_B \cos(q_C) \sin(q_C) - 4\cos(q_C)^2 \dot{q}_B \dot{q}_C) \\
& + P_5^B \left(\ddot{q}_C \cos(q_C) - \dot{q}_C{}^2 \sin(q_C)\right) \\
& + P_6^B (2\cos(q_C) \sin(q_C) \dot{q}_B \dot{q}_C - \cos(q_C)^2 \ddot{q}_B) \\
& + P_7^B (g - \ddot{q}_Z) \cos(q_B) \sin(q_C) + P_8^B (g - \ddot{q}_Z) \cos(q_B) \cos(q_C) + P_9^B \dot{q}_B \\
& + P_{10}^B sign(\dot{q}_B) + P_{11}^B sign(\dot{q}_B) e^{-|\dot{q}_B / Q_1^B{}_B|} + P_{12}^B \sin(Q_2^B q_B + Q_3^B) \\
& + P_{13}^B \left|\sin(q_B + Q_4^B)\right| \sin(Q_2^B q_B + Q_3^B)
\end{aligned}
\tag{3.15}
$$

C-axis:

$$
\begin{aligned}
u_C = {} & P_1^C \ddot{q}_C + P_2^C (2\cos(q_C)^2 - 1)\dot{q}_B{}^2 + P_3^C \ddot{q}_B \sin(q_C) + P_4^C \ddot{q}_B \cos(q_C) \\
& + P_5^C \left(-\sin(q_C)\cos(q_C)\dot{q}_B{}^2\right) + P_6^C (-\ddot{q}_Z + g) \sin(q_B) \cos(q_C) \\
& + P_7^C (\ddot{q}_Z - g) \sin(q_B) \sin(q_C) + P_8^C \dot{q}_C + P_9^C sign(\dot{q}_C) \\
& + P_{10}^C sign(\dot{q}_C) e^{-|\dot{q}_C / Q_1^C|} + P_{11}^C \sin\left(Q_2^C q_C + Q_3^C\right) \\
& + P_{12}^C \left|\sin\left(q_C + Q_4^C\right)\right| \sin\left(Q_2^C q_C + Q_3^C\right)
\end{aligned}
\tag{3.16}
$$

The parameters in the above open-loop dynamic equations, Eqs. (3.12)-(3.16), are summarized in Table 3-2.

Table 3-2 Number of parameters to be estimated for open-loop dynamics.

	X	Y	Z	B	C	Total
Linear parameters P_j^i	5	5	8	13	12	43
Nonlinear parameters Q_j^i	3	3	1	4	4	15

In order to estimate linear parameters by linear LS, the observation matrix $\boldsymbol{W}$ should be derived by differentiating the equations of motion Eq. (3.7) with respect to $\boldsymbol{\chi}_L$:

$$
\boldsymbol{W}(\boldsymbol{q}, \dot{\boldsymbol{q}}, \ddot{\boldsymbol{q}}, \boldsymbol{\chi}_{NL}) = \frac{\partial}{\partial \boldsymbol{\chi}_L} \left[\boldsymbol{M}(\boldsymbol{q})\ddot{\boldsymbol{q}} + \boldsymbol{h}(\boldsymbol{q}, \dot{\boldsymbol{q}}) + \boldsymbol{C}\dot{\boldsymbol{q}} + \boldsymbol{u}_f(\dot{\boldsymbol{q}}) + \boldsymbol{u}_p(\boldsymbol{q})\right] \tag{3.17}
$$

$\boldsymbol{\chi}_L$ and $\boldsymbol{\chi}_{NL}$ are vectors of linear and nonlinear parameters, where $\forall P_j^i \in \boldsymbol{\chi}_L$ and $\forall Q_j^i \in \boldsymbol{\chi}_{NL}$.

$\boldsymbol{\chi}_L$ contains all the parameters that differentiate Eq. (3.7) without leaving the parameter itself in $\boldsymbol{W}(\boldsymbol{q}, \dot{\boldsymbol{q}}, \ddot{\boldsymbol{q}}, \boldsymbol{\chi}_{NL})$. In other words, $\boldsymbol{W}$ is independent of $\boldsymbol{\chi}_L$. On the other hand, the parameters excluded from $\boldsymbol{\chi}_L$ are placed into $\boldsymbol{\chi}_{NL}$.

Per the dynamic model presented in Section 3.2, $\boldsymbol{\chi}_L$ includes the parameters of the multibody model $\boldsymbol{M}(\boldsymbol{q})$ and $\boldsymbol{h}(\boldsymbol{q}, \dot{\boldsymbol{q}})$, viscous friction term $\boldsymbol{C}$, the Coulomb friction C_i, the stiction S_i, and the torque ripple magnitude R_i. $\boldsymbol{\chi}_{NL}$ contains ω_{r_i} and ϕ_{r_i} from the torque ripple model and vs_i from the Stribeck curve.

Eq. (3.7) can then be re-written as a linear LS problem:

$$\boldsymbol{u} = \boldsymbol{W}(\boldsymbol{q}, \dot{\boldsymbol{q}}, \ddot{\boldsymbol{q}}, \hat{\boldsymbol{\chi}}_{NL})\boldsymbol{\chi}_L + \boldsymbol{error} \tag{3.18}$$

In this thesis, $\hat{\boldsymbol{\chi}}_{NL}$ is searched using a nonlinear global optimization method, Global Search (GS) [112], which combines gradient-based optimization, yielding fast local minima convergence, with a systematic approach of trying multiple different initial values selected from a prescribed search space. In every iteration of the GS, a set of candidate $\hat{\boldsymbol{\chi}}_{NL}$ is chosen first. Then, $\boldsymbol{\chi}_L$ is estimated by the pseudo inverse of $\boldsymbol{W}$ in the form (i.e., LS solution of Eq. (3.18))

$$\hat{\boldsymbol{\chi}}_L = \boldsymbol{W}^{\dagger}\boldsymbol{u} = \left(\boldsymbol{W}^{\boldsymbol{T}}\boldsymbol{W}\right)^{-1}\boldsymbol{W}^{\boldsymbol{T}}\boldsymbol{u} \tag{3.19}$$

The predicted motor input $\hat{\boldsymbol{u}}$ can be obtained by

$$\hat{\boldsymbol{u}} = \boldsymbol{W}\hat{\boldsymbol{\chi}}_L \tag{3.20}$$

Hence in each iteration of GS, $\|\boldsymbol{u} - \hat{\boldsymbol{u}}\|_2$, which is the 2-norm of error of motor torque prediction, is minimized with the prescribed $\hat{\boldsymbol{\chi}}_{NL}$. Thus, the objective function for GS is designed as

$$\min_{\boldsymbol{\chi}_{NL}} \|\boldsymbol{u} - \hat{\boldsymbol{u}}\|_2 \tag{3.21}$$

Thus, $\hat{\boldsymbol{\chi}}_L$ and $\hat{\boldsymbol{\chi}}_{NL}$ are estimated iteratively to produce the minimal prediction error in terms of motor torque. Such an approach is capable of solving problems with nonlinear parameters with efficiency, due to the tandem application of LS with GS, reducing the number of free-search parameter dramatically, per Table 3-2.

3.4 Experiment and Results

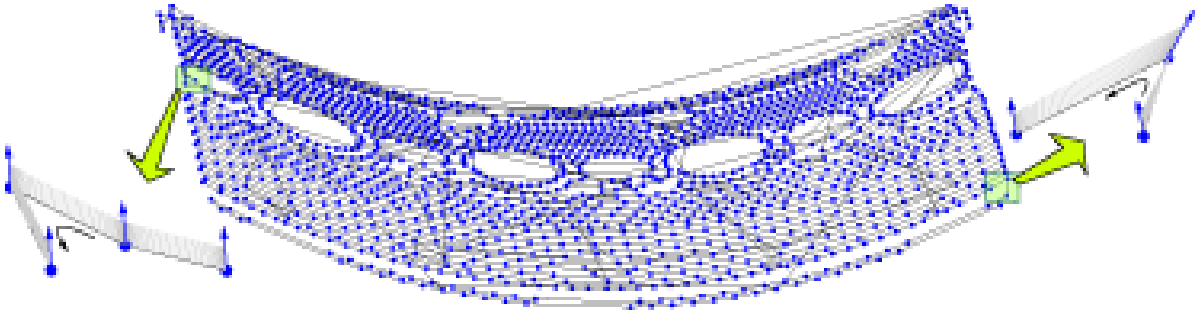

(a) Toolpath & orientation.

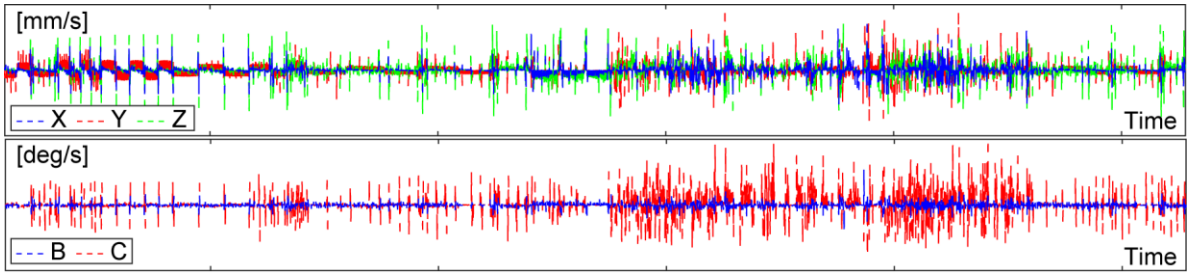

(b) Normalized axis velocity commands.

Figure 3-5 The trajectory of 5-axis laser drilling process.

The proposed method was applied to identify the model of a 5-axis laser drilling machine in industry. The motor current and measured (servo) position data were collected during a laser drilling process for producing a turbine engine component. The toolpath and the axial velocity of this drilling process are shown in Figure 3-5. For confidentiality, the data has been normalized without displaying absolute values. The toolpath contains a large number of simultaneous 5-axis movements, which can be regarded to show pseudo-random nature, thereby generating rich data for model identification.

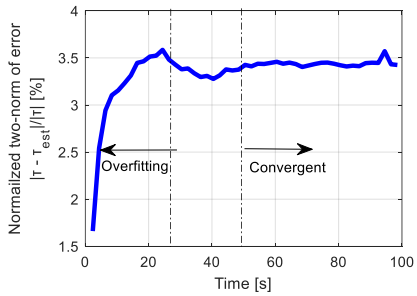

Figure 3-6 Normalized 2-norm of error.

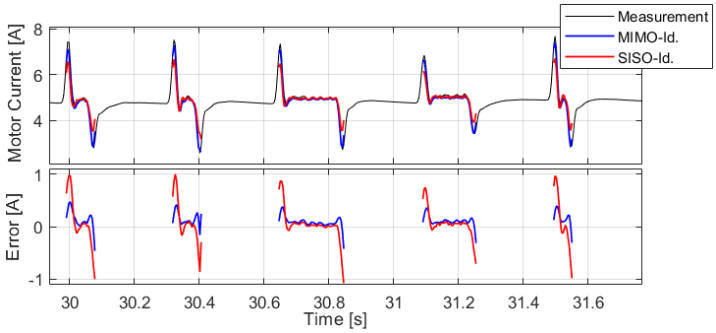

Figure 3-7 SISO vs. MIMO dynamic model, B-axis.

To prevent overfitting, the normalized 2-norm of error $\|\boldsymbol{u}-\hat{\boldsymbol{u}}\|_2/\|\boldsymbol{u}\|_2$ is plotted in Figure 3-6 to examine the convergence of the identification. The normalized 2-norm of error keeps rising in the first 20 seconds. It implies that the amount of data collected within this period could be insufficient. After around 50 seconds, the normalized 2-norm of error converges at around 3.4%, which means the collected data is sufficiently long for the identification.

To validate the superiority of the developed coupled nonlinear MIMO model, a SISO model is also identified as a baseline for comparison, which discards the dynamic coupling terms. Figure 3-7 shows the experimental data and model prediction results for the B-axis. During acceleration and deceleration periods, the SISO model has significantly larger estimation error, due to ignoring the dynamic coupling terms coming from the other axes. The result proves the advantage of using MIMO dynamic models for multi-axis machine tools with serial kinematic chains and direct drive rotary motors.

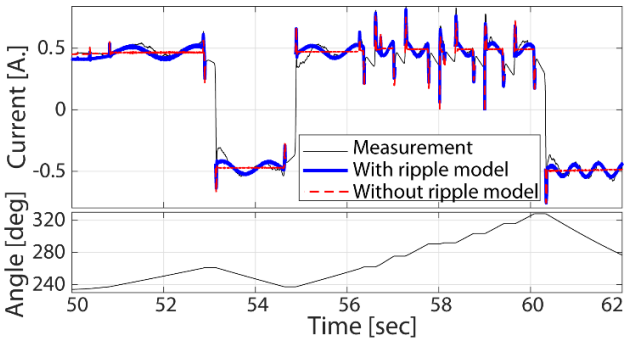

Figure 3-8 Motor current prediction, C-axis.

Figure 3-8 shows a comparison of C-axis motor current prediction with and without the torque ripple model. The position-dependent ripple is shown to be an apparent disturbance causing substantial motor current variation. Therefore, the torque ripple needs to be considered so that the estimation and simulation of other dynamic characteristics will not be corrupted due to this effect.

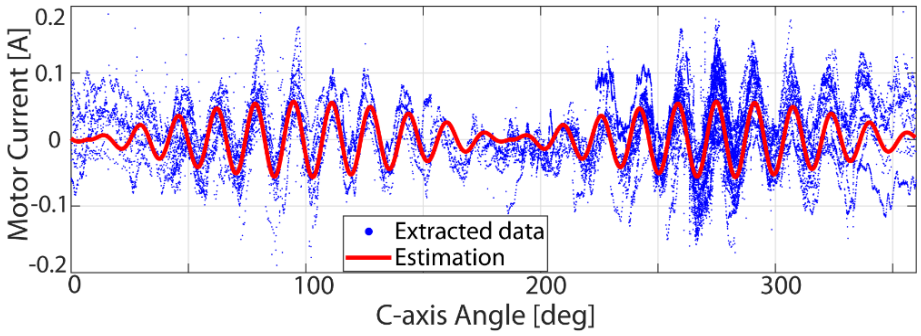

Figure 3-9 Torque ripple estimation, C-axis.

Figure 3-9 shows the estimated torque ripple overlapping with the extracted ripple data from the measured motor current. It shows that the frequency of ripples is consistent, and the magnitude varies with the angle, which is most likely due to imperfect motor assembly. This magnitude variation is also captured by the proposed model.

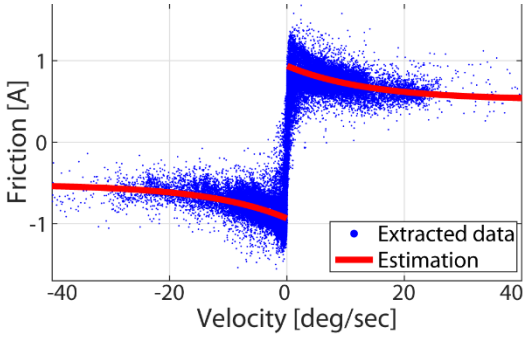

Figure 3-10 Friction estimation, B-axis.

A distinct Stribeck curve is also identified. Figure 3-10 shows the estimated friction model overlapping with the extracted friction data from the measured motor current. Due to the fact that the data was collected from a real drilling process, not from dedicated experiments, steady state condition (i.e. constant velocity) is not satisfied. Nevertheless, this result still substantially captures the friction behaviour.

3.5 Conclusion

This chapter presents the identification of the open-loop dynamics of a multi-axis feed drive system. The methodology is demonstrated using an industrial 5-axis laser drilling machine. The derived dynamic model considers multibody dynamics, nonlinear friction, and motor ripple. The model parameters are identified by combining nonlinear global optimization with linear least squares, based on the servo data collected during a real laser drilling process, which contains a large number of simultaneous multi-axis movements.

The identification results show that coupled multibody dynamics should be considered for accurate modeling of machine dynamics, especially for the acceleration and deceleration phases. Distinct Stribeck friction curve and motor ripple can also be identified from the gathered in-process data.

The established open-loop dynamic model in this chapter is an essential step prior to the identification of the complete closed-loop control system, which is presented in the next chapter.

Chapter 4
Identification of Multi-Axis Feed Drive Control System

4.1 Introduction and Motivation

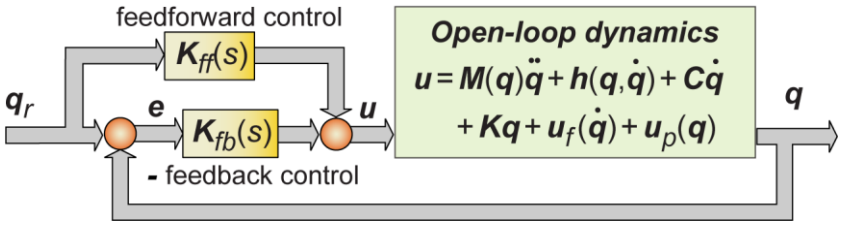

Figure 4-1 A multi-axis feed drive control system.

In Chapter 3, the open-loop dynamic model of a multi-axis feed drive system ($\boldsymbol{u} \rightarrow \boldsymbol{q}$) was built. Machine tool end users and researchers are especially interested in the control accuracy with respect to a certain manufacturing process, or being able to use the complete system dynamics for virtual process optimization or real-time signal monitoring. Therefore, the model should be extended to include the closed-loop control system ($\boldsymbol{q_r} \rightarrow \boldsymbol{q}$), which would further include the controllers for each axis (see Figure 4-1). However, the details of the commercial controllers are typically confidential and unknown to the end users. Thus, the controller dynamics, or its resulting impact on the closed-loop response, should also be identified.

There are at two main identification approaches. The first approach is identifying the controller and the open-loop dynamics (the plant) individually, in a bottom-up sense, in two separated steps. The other is identifying the closed loop control system as a whole in a top-down sense. The first approach requires more effort to investigate each component and may lead to a less accurate result, due to the accumulation of the estimation error resulting from the two separated steps.

The second approach, is also referred in CNC literature as 'rapid identification' [6] (see Section 2.3.2). Given that most of the industrial servo controllers are linear P-PI positive-velocity cascade structure with velocity and acceleration feedforward, the closed-loop control system of a single-axis feed drive can be described by a linear time-invariant (LTI) transfer function. However, when it comes to multi-axis feed drives where the multibody dynamics is coupled and nonlinear, such methodology, developed for a decoupled single-axis feed drive, becomes inaccurate.

In this chapter, the above problem is resolved by a novel decoupling formulation. An equivalent dynamic model derived through this formulation and the corresponding parameter estimation strategy is detailed in Section 4.2. Experimental validation shown in Section 4.3 demonstrates that a high-fidelity closed-loop response model for a multi-axis machine can be then established just with the knowledge of the kinematic configuration and collected CNC data.

4.2 Algorithm of MIMO Identification with Nonlinear Coupling

The proposed algorithm has two parts. First, an equivalent model representation to describe a general closed-loop control system is presented in Section 4.2.1 and Section 4.2.2. Second, the identification method of the above proposed equivalent model is presented in Section 4.2.3 and Section 4.2.4.

In Section 4.2.1, a decoupling formulation is first presented. It treats all the non-LTI open-loop dynamics as a generalized disturbance. In Section 4.2.2, the rest of the LTI open-loop dynamics and the LTI controllers constitute an LTI closed-loop control system, which is viewed as a MIMO LTI system where the generalized disturbance vector is considered among the system inputs.

Section 4.2.3 details the identification of the MIMO LTI system. Section 4.2.4 illustrates the overall model-building procedure, which utilizes and integrates the identification of the open-loop dynamics presented in Chapter 3.

4.2.1 Decoupling of the Nonlinear and Linear Open-Loop Dynamics

As discussed in Section 3.2, the open-loop dynamics of an N-axis feed drive can be modeled as:

$$\boldsymbol{u} = \boldsymbol{M}(\boldsymbol{q})\ddot{\boldsymbol{q}} + \boldsymbol{h}(\boldsymbol{q}, \dot{\boldsymbol{q}}) + \boldsymbol{C}\dot{\boldsymbol{q}} + \boldsymbol{K}\boldsymbol{q} + \boldsymbol{u}_f(\dot{\boldsymbol{q}}) + \boldsymbol{u}_p(\boldsymbol{q}) \tag{4.1}$$

$\boldsymbol{q} = \{q_1 \cdots q_i \cdots q_N\}^T$ and $\boldsymbol{u} = \{u_1 \cdots u_i \cdots u_N\}^T$ represent the actual position and control signal, respectively. $\boldsymbol{M}(\boldsymbol{q})$ is the mass matrix. $\boldsymbol{h}(\boldsymbol{q}, \dot{\boldsymbol{q}})$ is the vector containing Coriolis, centrifugal, and gravitational terms. $\boldsymbol{u}_f(\dot{\boldsymbol{q}})$ and $\boldsymbol{u}_p(\boldsymbol{q})$ are nonlinear friction and position-dependent disturbances respectively. $\boldsymbol{K}$ is the stiffness matrix if structural flexibility is considered. The examples demonstrated in this chapter (Section 4.3) are based on multi-rigid-body dynamics. Thus, while $\boldsymbol{K}$ matrix is not used in this chapter, it will be included and discussed in detail in Chapter 5. $\boldsymbol{C}$ matrix is linear viscous damping contributed by different joint interfaces, including prismatic joints (linear guideways), revolute joints (bearings), or flexible joints (in the case of a flexible structure).

The terms $\boldsymbol{M}(\boldsymbol{q})\ddot{\boldsymbol{q}}$ in Eq. (4.1) can be re-written as:

$$\boldsymbol{M}(\boldsymbol{q})\ddot{\boldsymbol{q}} = \begin{bmatrix} M_1 & & \\ & \ddots & \\ & & M_N \end{bmatrix}\ddot{\boldsymbol{q}} + \widetilde{\boldsymbol{M}}(\boldsymbol{q})\ddot{\boldsymbol{q}} = \boldsymbol{M}_{\Delta}\ddot{\boldsymbol{q}} + \widetilde{\boldsymbol{M}}(\boldsymbol{q})\ddot{\boldsymbol{q}} \tag{4.2}$$

$\boldsymbol{M}_{\boldsymbol{\Delta}}$ is a diagonal matrix which includes only the time-invariant and decoupled inertia terms. All the other nonlinear terms, such as trigonometric functions, are gathered in $\widetilde{\boldsymbol{M}}(\boldsymbol{q})$. Based on this separation, the Eq. (4.1) can be rearranged as:

$$\boldsymbol{u} = \boldsymbol{M}_{\Delta}\ddot{\boldsymbol{q}} + \boldsymbol{C}\dot{\boldsymbol{q}} + \boldsymbol{K}\boldsymbol{q} + \boldsymbol{d}(\boldsymbol{q}, \dot{\boldsymbol{q}}, \ddot{\boldsymbol{q}}) \tag{4.3}$$

$\boldsymbol{M}_{\Delta}\ddot{\boldsymbol{q}} + \boldsymbol{C}\dot{\boldsymbol{q}} + \boldsymbol{K}\boldsymbol{q}$ represents LTI dynamics, and $\boldsymbol{d}(\boldsymbol{q}, \dot{\boldsymbol{q}}, \ddot{\boldsymbol{q}})$, referred to in this thesis as the *'generalized disturbance'*, captures all significant nonlinearities, like coupled multibody dynamics, friction, and torque ripples. Considering Eqs. (4.1)-(4.3), it can be expressed as:

$$\boldsymbol{d}(\boldsymbol{q}, \dot{\boldsymbol{q}}, \ddot{\boldsymbol{q}}) = \widetilde{\boldsymbol{M}}(\boldsymbol{q})\ddot{\boldsymbol{q}} + \boldsymbol{h}(\boldsymbol{q}, \dot{\boldsymbol{q}}) + \boldsymbol{u}_f(\dot{\boldsymbol{q}}) + \boldsymbol{u}_p(\boldsymbol{q}) \tag{4.4}$$

In other words, $\boldsymbol{d}(\boldsymbol{q}, \dot{\boldsymbol{q}}, \ddot{\boldsymbol{q}})$ separates the nonlinearities from the rest of LTI dynamics.

Decoupling Derivation for the 5-Axis Laser Drilling Machine

To illustrate the above decoupling step, the 5-axis laser drilling machine introduced in Chapter 3 is used as an example. According to the multi-rigid-body dynamic equations (3.12)-(3.16), the general form of the decoupling expression Eq. (4.3) can be expressed as:

$$\begin{cases} u_X = P_1^X \ddot{q}_X + P_2^X \dot{q}_X + d_X \\ u_Y = P_1^Y \ddot{q}_Y + P_2^Y \dot{q}_Y + d_Y \\ u_Z = P_1^Z \ddot{q}_Z + P_6^Z \dot{q}_Z + d_Z \\ u_B = P_1^B \ddot{q}_B + P_9^B \dot{q}_B + d_B \\ u_C = P_1^C \ddot{q}_C + P_8^C \dot{q}_C + d_C \end{cases} \tag{4.5}$$

As mentioned earlier, since structural flexibility is not considered in this chapter (but will be studied from Chapter 5), the $\boldsymbol{K}\boldsymbol{q}$ term is excluded. The generalized disturbance $\boldsymbol{d} = [d_X\ d_Y\ d_Z\ d_B\ d_C]^T$ for each axis is then derived as follows.

X-axis:

$$d_X = P_3^X sign(\dot{q}_X) + P_4^X sign(\dot{q}_X) e^{-|\dot{q}_X / Q_1^X|} + P_5^X \sin(Q_2^X q_X + Q_3^X) \tag{4.6}$$

Y-axis:

$$d_Y = P_3^Y sign(\dot{q}_Y) + P_4^Y sign(\dot{q}_Y) e^{-|\dot{q}_Y/Q_1^Y|} + P_5^Y \sin(Q_2^Y q_Y + Q_3^Y) \tag{4.7}$$

Z-axis:

$$\begin{aligned} d_Z = {} & +P_2^Z + P_3^Z\left(cos(q_B)\,\dot{q}_B{}^2 + sin(q_B)\,\ddot{q}_B\right) \\ & + P_4^Z\left(-2\,cos(q_B)\,cos(q_C)\,\dot{q}_B\dot{q}_C + \left(\dot{q}_B{}^2 + \dot{q}_C{}^2\right) sin(q_B)\,sin(q_C)\right. \\ & \left. - sin(q_B)\,cos(q_C)\,\ddot{q}_C - cos(q_B)\,sin(q_C)\,\ddot{q}_B\right) \\ & + P_5^Z\left(2\,cos(q_B)\,sin(q_C)\,\dot{q}_B\dot{q}_C + \left(\dot{q}_B{}^2 + \dot{q}_C{}^2\right) sin(q_B)\,cos(q_C)\right. \\ & \left. + sin(q_B)\,sin(q_C)\,\ddot{q}_C - cos(q_B)\,cos(q_C)\,\ddot{q}_B\right) + P_7^Z sign(\dot{q}_Z) \\ & + P_8^Z sign(\dot{q}_Z) e^{-|\dot{q}_Z/Q_1^Z|} \end{aligned} \tag{4.8}$$

B-axis:

$$\begin{aligned} d_B = {} & P_2^B(\ddot{q}_Z - g)\,sin(q_B) + P_3^B\left(\dot{q}_C{}^2\,cos(q_C) + \ddot{q}_C\,sin(q_C)\right) \\ & + P_4^B(2\dot{q}_B\dot{q}_C - 2\ddot{q}_B\,cos(q_C)\,sin(q_C) - 4\,cos(q_C)^2\,\dot{q}_B\dot{q}_C) \\ & + P_5^B\left(\ddot{q}_C\,cos(q_C) - \dot{q}_C{}^2\,sin(q_C)\right) \\ & + P_6^B(2\,cos(q_C)\,sin(q_C)\,\dot{q}_B\dot{q}_C - cos(q_C)^2\,\ddot{q}_B) \\ & + P_7^B(g - \ddot{q}_Z)\,cos(q_B)\,sin(q_C) + P_8^B(g - \ddot{q}_Z)\,cos(q_B)\,cos(q_C) \\ & + P_{10}^B sign(\dot{q}_B) + P_{11}^B sign(\dot{q}_B) e^{-|\dot{q}_B/Q_1^B{}_B|} + P_{12}^B \sin(Q_2^B q_B + Q_3^B) \\ & + P_{13}^B \left|\sin(q_B + Q_4^B)\right| \sin(Q_2^B q_B + Q_3^B) \end{aligned} \tag{4.9}$$

C-axis:

$$\begin{aligned} d_C = {} & P_2^C(2\,cos(q_C)^2 - 1)\dot{q}_B{}^2 + P_3^C\ddot{q}_B\,sin(q_C) + P_4^C\ddot{q}_B\,cos(q_C) \\ & + P_5^C\left(-sin(q_C)\,cos(q_C)\dot{q}_B{}^2\right) + P_6^C(-\ddot{q}_Z + g)\,sin(q_B)\,cos(q_C) \\ & + P_7^C(\ddot{q}_Z - g)\,sin(q_B)\,sin(q_C) + P_9^C sign(\dot{q}_C) + P_{10}^C sign(\dot{q}_C) e^{-|\dot{q}_C/Q_1^C|} \\ & + P_{11}^C \sin\left(Q_2^C q_C + Q_3^C\right) + P_{12}^C \left|\sin\left(q_C + Q_4^C\right)\right| \sin\left(Q_2^C q_C + Q_3^C\right) \end{aligned} \tag{4.10}$$

4.2.2 MIMO LTI System Representation

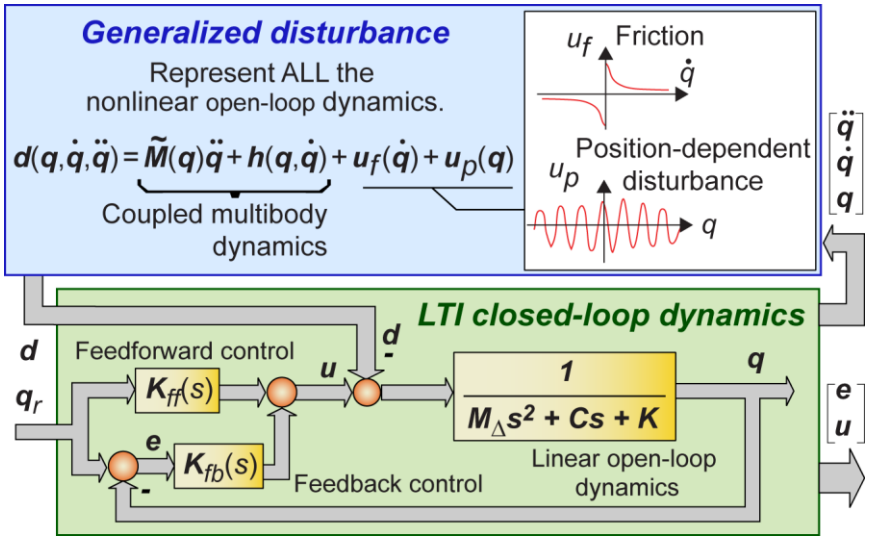

Figure 4-2 LTI closed-loop dynamics and the generalized disturbance.

The structure of an industrial servo controller could be PID or P-PI position-velocity cascade control with optional feedforward terms and filters, which in general fits the LTI framework. Nonlinear effects, like sensor quantization or actuator saturation, are either negligible or avoided through careful trajectory planning. Hence, a general controller with an LTI feedback and feedforward control law ($\boldsymbol{K_{fb}}$ and $\boldsymbol{K_{ff}}$) can be expressed as

$$\boldsymbol{u = K_{ff} q_r + K_{fb} e} \tag{4.11}$$

$\boldsymbol{e}$ is the tracking error, i.e., $\boldsymbol{e = q_r - q}$. Then, the open-loop dynamics (comprising LTI and nonlinear portions) and the LTI controller, i.e., Eq. (4.3), Eq. (4.4), and Eq. (4.11), can be combined as the block diagram shown in Figure 4-2, where the bottom green block represents LTI closed-loop dynamics, and the blue block on top represents the nonlinear effects, captured by the generalized disturbance $\boldsymbol{d}$.

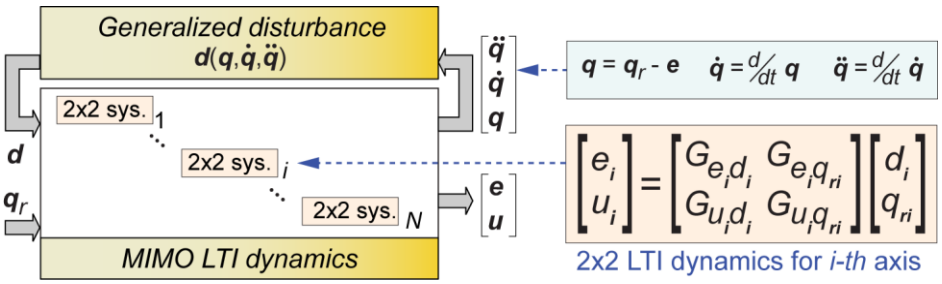

Figure 4-3 A general equivalent representation of a multi-axis feed drive control system.

Signals which are directly measurable from CNCs, such as tracking error $\boldsymbol{e}$ and motor force/torque $\boldsymbol{u}$, are selected as the outputs of the system. Also, these signals are highly relevant for monitoring the dynamic positioning accuracy and machine / process condition.

The LTI closed-loop dynamics, shown as the green block in Figure 4-2, can be viewed as a MIMO LTI system, where each axis is a 2×2 LTI subsystem, as shown in Figure 4-3. For the ith axis, the outputs are the servo error (e_i) and motor torque (u_i), and inputs are the generalized disturbance (d_i) and trajectory position command (q_{r_i}).

The calculation of the generalized disturbance $\boldsymbol{d}$ requires mechanical states variables $[\boldsymbol{q}, \dot{\boldsymbol{q}}, \ddot{\boldsymbol{q}}]$, which can be determined by Eq. (4.12) as additional outputs of the MIMO LTI closed-loop dynamics

$$\begin{cases} \boldsymbol{q} = \boldsymbol{q_r} - \boldsymbol{e} \\ \dot{\boldsymbol{q}} = \dfrac{d}{dt}\boldsymbol{q} \\ \ddot{\boldsymbol{q}} = \dfrac{d}{dt}\dot{\boldsymbol{q}} \end{cases} \tag{4.12}$$

For the ith axis, the LTI closed-loop dynamics is a 2×2 subsystem expressed as

$$\begin{cases} e_i(s) = G_{e_i d_i}(s) d_i(s) + G_{e_i q_{r_i}}(s) q_{r_i}(s) \\ u_i(s) = G_{u_i d_i}(s) d_i(s) + G_{u_i q_{r_i}}(s) q_{r_i}(s) \end{cases} \tag{4.13}$$

$$G_{e_i d_i}(s) = \frac{N_{e_i d_i}(s)}{D_i(s)};\ \ G_{e_i q_{r_i}}(s) = \frac{N_{e_i q_{r_i}}(s)}{D_i(s)};\ \ G_{u_i d_i}(s) = \frac{N_{u_i d_i}(s)}{D_i(s)};\ \ G_{u_i q_{r_i}}(s) = \frac{N_{u_i q_{r_i}}(s)}{D_i(s)}$$

The four transfer functions share the same characteristic polynomial $D_i(s)$:

$$D_i(s) = \boldsymbol{\Pi}_{m=1}^{n_{r_i}} \boldsymbol{\Pi}_{k=1}^{n_{c_i}} \left(s + p_{m,i}\right) \left(s^2 + 2\zeta_{k,i}\omega_{n_{k,i}} s + {\omega_{n_{k,i}}}^2\right) \tag{4.14}$$

n_{r_i} and n_{c_i} are the numbers of real poles and complex pole pairs. $n_{p_i} = n_{r_i} + 2 \times n_{c_i}$ is the total number of poles, i.e., the order of the linear closed-loop dynamic model. $N_{e_i d_i}(s)$, $N_{e_i q_{r_i}}(s)$, $N_{u_i d_i}(s)$, and $N_{u_i q_{r_i}}(s)$ are numerator polynomials of which the order and structure can be determined by deriving each of the symbolic transfer functions. For generality, the following equations represent the full-order expressions.

$$\begin{cases} N_{e_i d_i}(s) = b_0^{e_i d_i} s^{n_{p_i}} + b_1^{e_i d_i} s^{n_{p_i}-1} + \cdots + b_{n_{p_i}-1}^{e_i d_i} s^1 + b_{n_{p_i}}^{e_i d_i} s^0 \\ N_{e_i q_{r_i}}(s) = b_0^{e_i q_{r_i}} s^{n_{p_i}} + b_1^{e_i q_{r_i}} s^{n_{p_i}-1} + \cdots + b_{n_{p_i}-1}^{e_i q_{r_i}} s^1 + b_{n_{p_i}}^{e_i q_{r_i}} s^0 \\ N_{u_i d_i}(s) = b_0^{u_i d_i} s^{n_{p_i}} + b_1^{u_i d_i} s^{n_{p_i}-1} + \cdots + b_{n_{p_i}-1}^{u_i d_i} s^1 + b_{n_{p_i}}^{u_i d_i} s^0 \\ N_{u_i q_{r_i}}(s) = b_0^{u_i q_{r_i}} s^{n_{p_i}} + b_1^{u_i q_{r_i}} s^{n_{p_i}-1} + \cdots + b_{n_{p_i}-1}^{u_i q_{r_i}} s^1 + b_{n_{p_i}}^{u_i q_{r_i}} s^0 \end{cases} \quad (4.15)$$

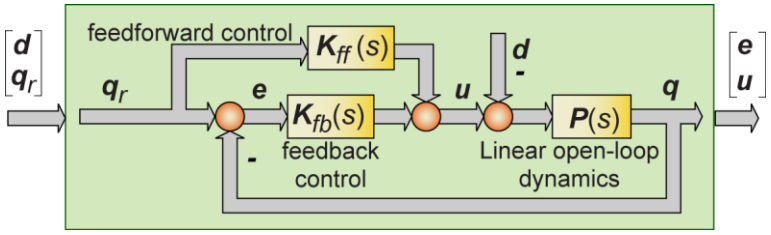

Figure 4-4 LTI closed-loop dynamics.

The LTI closed-loop dynamics (green block) in Figure 4-2 can, in a more general case, also be presented in Figure 4-4, where the linear open-loop dynamics is denoted as $\boldsymbol{P}(s)$. Then, the transfer functions of the 2×2 system can be derived as follows.

$$G_{e_i d_i}(s) = \frac{P_i(s)}{1 + K_{fb_i}(s)P_i(s)} \quad G_{e_i q_{r_i}}(s) = \frac{1 - K_{ff_i}(s)P_i(s)}{1 + K_{fb_i}(s)P_i(s)}$$
$$G_{u_i d_i}(s) = \frac{K_{fb_i}(s)P_i(s)}{1 + K_{fb_i}(s)P_i(s)} \quad G_{u_i q_{r_i}}(s) = \frac{K_{fb_i}(s) + K_{ff_i}(s)}{1 + K_{fb_i}(s)P_i(s)} \quad (4.16)$$

Considering a typical industrial controller and plant, several assumptions can be made as listed in Table 4-1. The numbers of poles of each component are determined accordingly.

Table 4-1 System assumption and the resulting number of poles.

	No. of poles	Assumption
$K_{fb_i}(s)$	1	Considering an integral controller, one pole is assigned.
$K_{ff_i}(s)$	2	Velocity and acceleration feedforward is included. To realize a causal system, two high-frequency poles are configured.
$P_i(s)$	2+2×n	One rigid body motion is 2nd-order. If further considering n vibratory modes, 2×n poles can be added into the system.

According to the above assumptions, the general expressions of the numerator polynomial and characteristic polynomial, Eq. (4.14) and Eq. (4.15), can be determined and simplified. The following sections illustrate a rigid body case and a flexible structure with one vibratory mode respectively.

Rigid Body Case

The rigid body motion and the integral control can be arranged as one real pole and one complex pole pair. The complex pair would automatically be identified as two real poles, in the case that the true servo system demonstrates overdamped behavior. The feedforward control contributes two real poles in the high-frequency region, in order to realize a causal system (i.e., low-pass filter implementation together with derivative). In total, the characteristic polynomial $D_i(s)$ can be configured as a *5*th-order system with three real poles ($n_{r_i} = 3$) and one complex pole pair ($n_{c_i} = 1$.) The respective characteristic polynomial and numerator polynomial structure can be derived and simplified as:

$$\begin{cases} D_i(s) = \mathbf{\Pi}_{m=1}^{3}\mathbf{\Pi}_{k=1}^{1}\left(s + p_{m,i}\right)\left(s^2 + 2\zeta_{k,i}\omega_{n_{k,i}}s + {\omega_{n_{k,i}}}^2\right) \\ N_{e_i d_i}(s) = b_1^{e_i d_i}s^1 + b_2^{e_i d_i}s^0 \\ N_{e_i q_{r_i}}(s) = b_1^{e_i q_{r_i}}s^5 + b_2^{e_i q_{r_i}}s^4 + b_3^{e_i q_{r_i}}s^3 + b_4^{e_i q_{r_i}}s^2 + b_5^{e_i q_{r_i}}s^1 \\ N_{u_i d_i}(s) = b_1^{u_i d_i}s^2 + b_2^{u_i d_i}s^1 + \mathbf{\Pi}_{m=1}^{3}\mathbf{\Pi}_{k=1}^{1}p_{m,i}{\omega_{n_{k,i}}}^2 \\ N_{u_i q_{r_i}}(s) = b_1^{u_i q_{r_i}}s^5 + b_2^{u_i q_{r_i}}s^4 + b_3^{u_i q_{r_i}}s^3 + b_4^{u_i q_{r_i}}s^2 + b_5^{u_i q_{r_i}}s^1 \end{cases} \tag{4.17}$$

It should be noted that the two real poles coming from the feedforward control, due to their fast response, will not cause significant impact on the overall dynamic responses. Hence, they can be preassigned as certain high-frequency values (such as a fraction of the Nyquist frequency) and do not need to be treated as unknown variables.

Flexible Structure with One Vibratory Mode

If taking one vibratory mode into account, the number of complex pole pairs n_{c_i} can be configured as two, leading to a *7*th-order system. The respective numerator polynomial can be derived as:

$$\begin{cases} D_i(s) = \mathbf{\Pi}_{m=1}^{3}\mathbf{\Pi}_{k=1}^{2}\left(s + p_{m,i}\right)\left(s^2 + 2\zeta_{k,i}\omega_{n_{k,i}}s + {\omega_{n_{k,i}}}^2\right) \\ N_{e_i d_i}(s) = b_1^{e_i d_i}s^3 + b_2^{e_i d_i}s^2 + b_3^{e_i d_i}s^1 + b_4^{e_i d_i}s^0 \\ N_{e_i q_{r_i}}(s) = b_1^{e_i q_{r_i}}s^7 + b_2^{e_i q_{r_i}}s^6 + b_3^{e_i q_{r_i}}s^5 + b_4^{e_i q_{r_i}}s^4 + b_5^{e_i q_{r_i}}s^3 + b_6^{e_i q_{r_i}}s^2 + b_7^{e_i q_{r_i}}s^1 \\ N_{u_i d_i}(s) = b_1^{u_i d_i}s^4 + b_2^{u_i d_i}s^3 + b_3^{u_i d_i}s^2 + b_4^{u_i d_i}s^1 + \mathbf{\Pi}_{m=1}^{3}\mathbf{\Pi}_{k=1}^{2}p_{m,i}{\omega_{n_{k,i}}}^2 \\ N_{u_i q_{r_i}}(s) = b_1^{u_i q_{r_i}}s^7 + b_2^{u_i q_{r_i}}s^6 + b_3^{u_i q_{r_i}}s^5 + b_4^{u_i q_{r_i}}s^4 + b_5^{u_i q_{r_i}}s^3 + b_6^{u_i q_{r_i}}s^2 + b_7^{u_i q_{r_i}}s^1 \end{cases} \tag{4.18}$$

4.2.3 Parameter Identification of MIMO LTI System

In the last section, the equivalent model of a multi-axis feed drive control system was derived, comprising a MIMO LTI portion and the nonlinear dynamics. In this section, the identification of the MIMO LTI system is illustrated.

There are two main steps in this identification. First, the predicted generalized disturbance is reconstructed from the estimated open-loop dynamic model. Second, the predicted generalized disturbance and the collected CNC data are used to identify the MIMO LTI system. The pole locations and numerator coefficients are iteratively estimated by constrained global optimization in conjunction with linear LS. This strategy accelerates and improves the convergence of the model identification.

Generalized Disturbance Reconstruction

In Section 3.3, the parameters of the open-loop dynamic model, i.e., $\widehat{\boldsymbol{\chi}}_L$ and $\widehat{\boldsymbol{\chi}}_{NL}$, were estimated. By plugging $\widehat{\boldsymbol{\chi}}_L$ and $\widehat{\boldsymbol{\chi}}_{NL}$ into Eq. (4.4), the predicted generalized disturbance $\widehat{\boldsymbol{d}}$ can be reconstructed by the collected CNC data, $\boldsymbol{q}$, $\dot{\boldsymbol{q}}$, and $\ddot{\boldsymbol{q}}$, per the following equation:

$$\widehat{\boldsymbol{d}}(\boldsymbol{q}, \dot{\boldsymbol{q}}, \ddot{\boldsymbol{q}}, \widehat{\boldsymbol{\chi}}_L, \widehat{\boldsymbol{\chi}}_{NL}) = \widetilde{\boldsymbol{M}}(\boldsymbol{q}, \widehat{\boldsymbol{\chi}}_L)\ddot{\boldsymbol{q}} + \widetilde{\boldsymbol{h}}(\boldsymbol{q}, \dot{\boldsymbol{q}}, \widehat{\boldsymbol{\chi}}_L) + \boldsymbol{u}_f\left(\dot{\boldsymbol{q}}, \widehat{\boldsymbol{X}}_L, \widehat{\boldsymbol{X}}_{NL}\right) + \boldsymbol{u}_p\left(\boldsymbol{q}, \widehat{\boldsymbol{X}}_L\right) \qquad (4.19)$$

Pole Search with LS Projection Method

Numerous approaches can be used to identify the parameters of the proposed closed-loop MIMO LTI model. Identifying all the parameters by least squares (LS) method can be very computationally efficient. However, since there is no constraint, this approach could lead to unstable poles due to noisy observed data. On the other hand, if all the parameters were found by constrained nonlinear optimization methods, this approach may require a high computational cost.

Pole search with LS projection method [7][8] is a middle ground strategy that resolves the above dilemma. Essentially, it is a hybrid strategy where the poles are searched by constrained optimization, while the numerator coefficients are dependently solved for each candidate pole set using LS . In this thesis, a specific version of this approach has been derived for a 2×2 system, representing the *i*th axis.

Considering the general full-order numerator polynomial in Eq. (4.15), the 2×2 LTI subsystem in Eq. (4.13) can be rearranged as:

$$\begin{cases} e_i(s) = \left(\dfrac{\hat{d}_i(s)s^{n_{p_i}}}{D_i(s)}b_0^{e_i d_i} + \cdots + \dfrac{\hat{d}_i(s)s^0}{D_i(s)}b_{n_{p_i}}^{e_i d_i}\right) + \left(\dfrac{q_{r_i}(s)s^{n_{p_i}}}{D_i(s)}b_0^{e_i q_{r_i}} + \cdots + \dfrac{q_{r_i}(s)s^0}{D_i(s)}b_{n_{p_i}}^{e_i q_{r_i}}\right) \\ u_i(s) = \left(\dfrac{\hat{d}_i(s)s^{n_{p_i}}}{D_i(s)}b_0^{u_i d_i} + \cdots + \dfrac{\hat{d}_i(s)s^0}{D_i(s)}b_{n_{p_i}}^{u_i d_i}\right) + \left(\dfrac{q_{r_i}(s)s^{n_{p_i}}}{D_i(s)}b_0^{u_i q_{r_i}} + \cdots + \dfrac{q_{r_i}(s)s^0}{D_i(s)}b_{n_{p_i}}^{u_i q_{r_i}}\right) \end{cases} \quad (4.20)$$

Eq. (4.20) is a general full-order expression. Depending on the model assumptions, this can be simplified as, for example, Eq. (4.17) or (4.18). To keep the derivation general, the following illustration is based on the full-order expression.

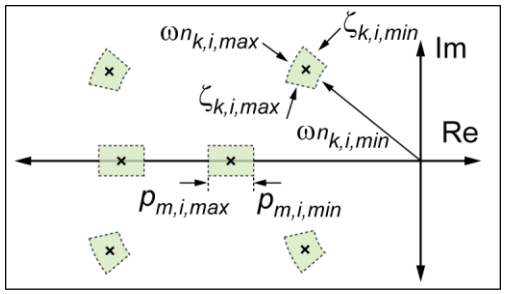

Figure 4-5 Pole search scheme.

As seen in Figure 4-5, a candidate pole vector $\boldsymbol{\chi}_{P_i} = \left[p_{1,i}, \ldots, p_{n_{r_i},i}, \omega_{n1,i}, \ldots, \omega_{n_{n_{c_i},i}}, \zeta_{1,i}, \ldots, \zeta_{n_{c_i},i}\right]^T$ can be searched within prescribed boundaries by constrained global optimization methods. The candidate characteristic polynomial $D_i(s)$ is constructed according to the candidate pole vector $\boldsymbol{\chi}_{P_i}$.

After constructing a candidate characteristic polynomial $D_i(s)$, $\hat{d}_i$ and q_{r_i} are used to compute $w_k^{d_i}(s)$ and $w_k^{q_{r_i}}(s)$ via the filter $\frac{s^k}{D_i(s)}$.

$$\begin{cases} w_k^{d_i}(s) = \dfrac{s^k}{D_i(s)}\hat{d}_i(s) \\ w_k^{q_{r_i}}(s) = \dfrac{s^k}{D_i(s)}q_{r_i}(s) \end{cases}; k \in \left[0, \ldots, n_{p_i}\right] \quad (4.21)$$

$w_k^{d_i}(s)$ and $w_k^{q_{r_i}}(s)$ are called 'filtered' versions of inputs by the candidate characteristic polynomial. By plugging in $w_k^{d_i}(s)$ and $w_k^{q_{r_i}}(s)$, Eq. (4.20) can be derived as

$$\begin{cases} e_i(s) = \left(w_{n_{p_i}}^{d_i}(s)b_0^{e_i d_i} + \cdots + w_0^{d_i}(s)b_{n_{p_i}}^{e_i d_i}\right) + \left(w_{n_{p_i}}^{q_i}(s)b_0^{e_i q_{r_i}} + \cdots + w_0^{q_{r_i}}(s)b_{n_{p_i}}^{e_i q_{r_i}}\right) \\ u_i(s) = \left(w_{n_{p_i}}^{d_i}(s)b_0^{u_i d_i} + \cdots + w_0^{d_i}(s)b_{n_{p_i}}^{u_i d_i}\right) + \left(w_{n_{p_i}}^{q_{r_i}}(s)b_0^{u_i q_{r_i}} + \cdots + w_0^{q_{r_i}}(s)b_{n_{p_i}}^{u_i q_{r_i}}\right) \end{cases} \quad (4.22)$$

The numerator coefficients $b_k^{e_i d_i}$, $b_k^{e_i q_{r_i}}$, $b_k^{u_i d_i}$, and $b_k^{u_i q_{r_i}}$ are unknown and can be viewed as the participation factors of the filtered inputs $w_k^{d_i}(s)$ and $w_k^{q_{r_i}}(s)$ on the outputs $e_i(s)$ and $u_i(s)$. The unknown numerator coefficients are linearly arranged and therefore can be estimated by linear LS via the known signals of $w_k^{d_i}$, $w_k^{q_{r_i}}$, e_i, and u_i.

While collecting the identification dataset, Eq. (4.22) can be constructed as an overdetermined system:

$$\begin{Bmatrix} \boldsymbol{e}_i \\ \boldsymbol{u}_i \end{Bmatrix} = \begin{bmatrix} \boldsymbol{W_i} & \boldsymbol{O} \\ \boldsymbol{O} & \boldsymbol{W_i} \end{bmatrix} \boldsymbol{\chi}_{B_i} + \boldsymbol{\varepsilon}_i \tag{4.23}$$

$\boldsymbol{e}_i$ and $\boldsymbol{u}_i$ are N_t samples of tracking error and motor current data, $\begin{cases} \boldsymbol{e}_i = [e_i(1) \quad \cdots \quad e_i(N_t)]_{1\times N_t}^T \\ \boldsymbol{u}_i = [u_i(1) \quad \cdots \quad u_i(N_t)]_{1\times N_t}^T \end{cases}$

$\boldsymbol{W_i}$ is the observation matrix composed of N_t samples of filtered inputs $w_k^{d_i}$ and $w_k^{q_{r_i}}$:

$$\boldsymbol{W_i} = \begin{bmatrix} w_{n_{p_i}}^{d_i}(1) & \cdots & w_0^{d_i}(1) & w_{n_{p_i}}^{q_{r_i}}(1) & \cdots & w_0^{q_{r_i}}(1) \\ \vdots & \cdots & \vdots & \vdots & \cdots & \vdots \\ w_{n_{p_i}}^{d_i}(N_t) & \cdots & w_0^{d_i}(N_t) & w_{n_{p_i}}^{q_{r_i}}(N_t) & \cdots & w_0^{q_{r_i}}(N_t) \end{bmatrix}_{N_t\times(2n_{p_i}+2)}$$

$\boldsymbol{\chi}_{B_i}$ is the numerator coefficient vector:

$$\boldsymbol{\chi}_{B_i} = \begin{bmatrix} b_0^{e_i d_i} & \cdots & b_{n_{p_i}}^{e_i d_i} & b_0^{e_i q_{r_i}} & \cdots & b_{n_{p_i}}^{e_i q_{r_i}} & b_0^{u_i d_i} & \cdots & b_{n_{p_i}}^{u_i d_i} & b_0^{u_i q_{r_i}} & \cdots & b_{n_{p_i}}^{u_i q_{r_i}} \end{bmatrix}_{1\times(4n_{p_i}+4)}^T$$

Thus, for each candidate pole set $\boldsymbol{\chi}_{P_i}$, the numerator coefficient vector $\boldsymbol{\chi}_{B_i}$ is estimated by the pseudo inverse of $\boldsymbol{W_i}$ in the form:

$$\widehat{\boldsymbol{\chi}_{B_i}} = \begin{bmatrix} (\boldsymbol{W_i^T W_i})^{-1}\boldsymbol{W_i^T} & \boldsymbol{O} \\ \boldsymbol{O} & (\boldsymbol{W_i^T W_i})^{-1}\boldsymbol{W_i^T} \end{bmatrix} \begin{Bmatrix} \boldsymbol{e}_i \\ \boldsymbol{u}_i \end{Bmatrix} \tag{4.24}$$

The best estimate for $\boldsymbol{X}_{B_i}$ and $\boldsymbol{X}_{P_i}$ are iteratively found by using a constrained global optimization method that minimizes the following objective function:

$$\min_{\boldsymbol{\chi}_{P_i}} \left\| \begin{Bmatrix} \boldsymbol{e}_i \\ \boldsymbol{u}_i \end{Bmatrix} - \begin{bmatrix} \boldsymbol{W_i} & \boldsymbol{O} \\ \boldsymbol{O} & \boldsymbol{W_i} \end{bmatrix} \widehat{\boldsymbol{\chi}_{B_i}} \right\|_2 \tag{4.25}$$

4.2.4 Proposed Model Estimation Procedure

Table 4-2 Parameter classification.

Machine model	Independent parameters	Dependent parameters
Closed-loop MIMO LTI dynamics	Pole locations $\boldsymbol{\chi}_P$	Numerator coefficients $\boldsymbol{\chi}_B$
Open-loop dynamics	Nonlinear parameters $\boldsymbol{\chi}_{NL}$	Linear parameters $\boldsymbol{\chi}_L$
Method of parameter estimation	Estimated by constrained global optimization	Estimated by linear LS

Per the classification shown in Table 4-2, the proposed entire machine model has two parts, MIMO LTI system and open-loop (generally nonlinear) dynamics, with four distinct sets of parameters $\boldsymbol{\chi}_P$, $\boldsymbol{\chi}_B$, $\boldsymbol{\chi}_L$, and $\boldsymbol{\chi}_{NL}$. $\boldsymbol{\chi}_P$ and $\boldsymbol{\chi}_{NL}$ are independent parameters which have to be found by constrained global optimization. Once $\boldsymbol{\chi}_P$ and $\boldsymbol{\chi}_{NL}$ are determined, $\boldsymbol{\chi}_B$ and $\boldsymbol{\chi}_L$ are dependently estimated by linear LS.

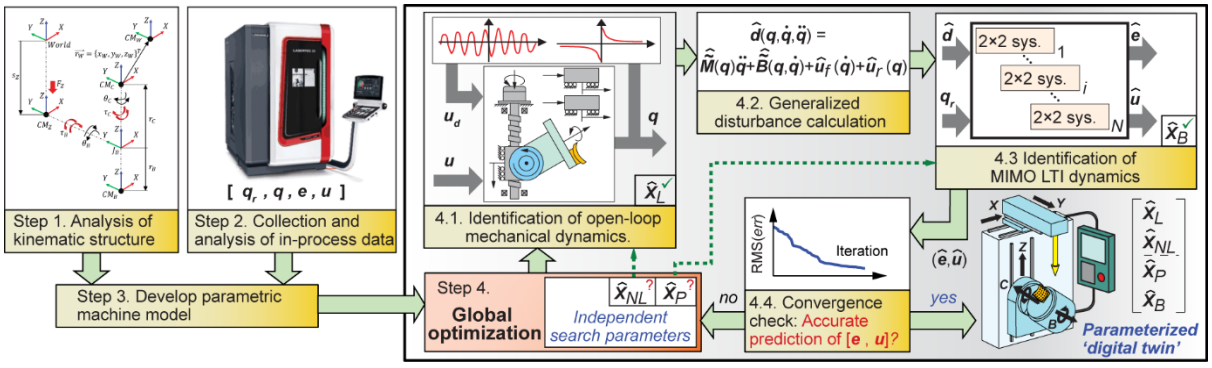

Figure 4-6 An overview of the proposed model-building approach via in-process data.

The complete model estimation procedure is presented in Figure 4-6. The multibody dynamics is derived based on the given machine kinematic configuration (Step 1). Field data collection and analysis (Step 2) helps detect vibratory dynamics, inter-axis coupling, friction, and ripple effects. The parametric dynamic model is configured and derived according to the above information in Step 3. The parameters are iteratively solved in Step 4. In each iteration, at first, global search [112], which is a constrained global optimization method, is performed to find candidate independent parameters, $\boldsymbol{\chi}_P$ and $\boldsymbol{\chi}_{NL}$. In Step 4.1, identification of open-loop dynamics is performed to estimate $\boldsymbol{\chi}_L$ (see Section 3.3). In Step 4.2, the predicted generalized disturbance $\widehat{\boldsymbol{d}}$ is constructed based on the estimated $\widehat{\boldsymbol{\chi}_L}$ and the candidate $\widehat{\boldsymbol{\chi}_{NL}}$ (see Section 4.2.1). In Step 4.3, the identification of MIMO LTI system is performed to estimate

the numerator coefficients χ_B (see Section 4.2.3). Lastly. Step 4.4 monitors estimation error and terminates the iteration of global optimization when the optimum is found, or given search duration is exceeded.

4.2.5 Novel Points and Advantages of the Proposed Algorithm

The proposed idea has numerous novelties listed below:

A. By separating the nonlinear and linear terms, both the nonlinear multibody dynamic model as well as the linear controller model can be identified together.
B. The stability of the identified closed-loop system is guaranteed by using a constrained optimization method to search for the poles in the stable region. This approach is superior to linear least squares, where the parameters solution is unbounded. Additionally, the pole locations for the control systems in industrial machine tools are normally located within a certain range. This information facilitates easier bounding of the pole locations.
C. The separation of the parameters into independent and dependent parameters greatly balances model accuracy and computational efficiency for identification. For example, as shown in Section 4.3.1, an overall machine model with 143 parameters can be identified with this systematic solution, while requiring the simultaneous search of no more than 4-8 independent parameters at a time.
D. In earlier methods [6][7][8][9], the disturbance only included Coulomb friction. In this work, the generalized disturbance additionally includes inter-axis coupling and/or ripple effects, which improves the persistence of excitation for the LTI model identification.
E. The developed algorithm is systematic, and the model can be configured conveniently by the given machine kinematics, which is easily accessible documentation. Hence, this method is conducive to automated digital twin estimation for machine tool drive systems.
F. The model can be extended for multi-axis drives with structural flexibility. This extension is discussed in Chapter 5 through Chapter 8.

4.3 Experimental Validation

The proposed model estimation method has been implemented and validated using the 5-axis laser drilling machine, introduced in Chapter 3, and an in-house 3-axis trunnion unit. The results are illustrated in the following subsections.

4.3.1 Five-Axis Laser Drilling Machine

The parametric machine model was developed considering all the dynamic effects mentioned in Section 3.2. Table 4-3 is a summary of all the parameters in the developed model. There are 143 parameters in total, where 34 (15+19) parameters are independent search parameters. However, as a main strength of the proposed systematic identification strategy, the number of simultaneously searched independent parameters for each axis remains only in the range of 4-8, which renders the proposed solution highly efficient.

Table 4-3 Parameter number statistics for laser drilling machine model.

			X	Y	Z	B	C	Total
Open-loop dynamics	χ_{NL}	Stribeck Friction velocity const. v_s	1	1	1	1	1	15
		Torque ripple spatial freq. ω_r	1	1	-	1	1	
		Torque ripple phase shift ϕ_r	1	1	-	1	1	
		Ripple amplitude phase ϵ_r	-	-	-	1	1	
	χ_L	Diagonal inertia	1	1	1	1	1	43
		Diagonal damping	1	1	1	1	1	
		Coupled multibody dynamics	-	-	4	7	6	
		Torque ripple amplitude R	1	1	-	1	1	
		Ripple amplitude modulation α_r	-	-	-	1	1	
		Stribeck and Coulomb friction	2	2	2	2	2	
Closed-loop LTI dynamics	χ_P	Rigid body motion poles p_1, ω_{n1}, ζ_1	3	3	3	3	3	19
		Vibratory response poles ω_{n2}, ζ_2	2	2	-	-	-	
	χ_B	Numerator terms for $N_{e_i d_i}(s)$	4	4	2	2	2	84
		Numerator terms for $N_{e_i q_{r_i}}(s)$	6	6	5	5	5	
		Numerator terms for $N_{u_i d_i}(s)$	4	4	2	2	2	
		Numerator terms for $N_{u_i q_{r_i}}(s)$	7	7	5	5	5	
Independent parameters χ_{NL} & χ_P			8	8	4	7	7	34
Dependent parameters χ_L & χ_B			26	26	22	27	26	127
Total number of parameters			34	34	26	34	33	161

The data was collected during the operation of the 5-axis laser drilling machine to produce a turbine engine component as shown in Figure 3-5. In total, estimating the full model took 623 seconds on a 3.6 GHz personal computer. The model achieved 2.38% root mean square (RMS) error in predicting the servo errors and motor torques. The prediction results are presented in the following sections.

Linear X and Y Axes

The X and Y axes were observed to exhibit a vibratory mode, and therefore their 2×2 LTI models were configured as 7th-order systems with 3 real poles and 2 complex pole pairs following Eq. (4.18).

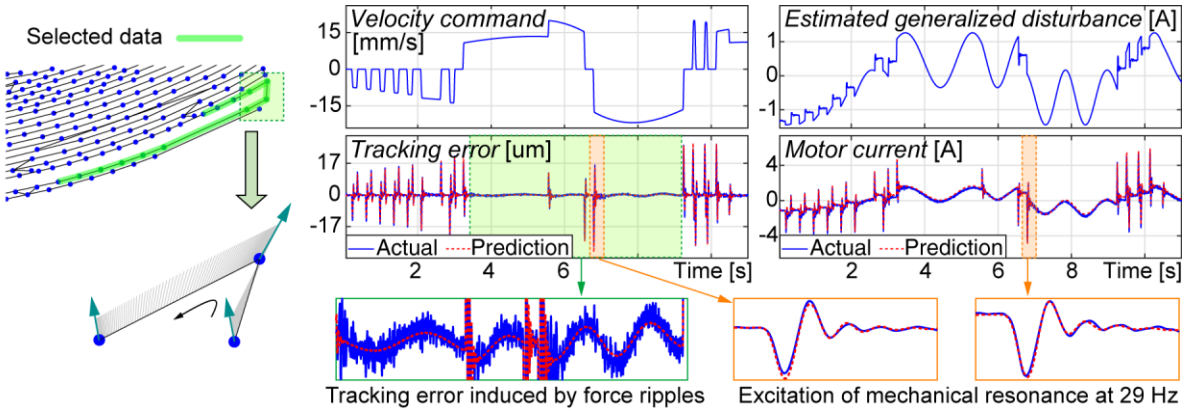

Figure 4-7 Predicted and experimental result for the X-axis servo control system.

From the entire collected data, a 12-second data packet was adopted to identify the models for the X and Y axes. The prediction of tracking error and motor current in the X axis are shown in Figure 4-7. This linear axis feed drive is equipped with a direct linear drive motor. Strong force ripple is therefore taken into account. The green zone demonstrates the influence of the force ripple disturbance on the tracking error during sustained velocity motion. The wavy variation of the tracking error corresponds to the pattern of the force ripple disturbance. On the other hand, the orange zone highlights vibratory behavior resulting from the 29 Hz natural mode during a high-acceleration motion.

The estimated generalized disturbance $\hat{d}_X$ containing the nonlinear friction and force ripple is also shown in the top right figure in Figure 4-7. This term is critical for correct estimation of the LTI dynamics. The response to the force ripple and the structural resonance are both similar wavy patterns in the time domain. They are distinguished and identified separately by introducing a position-dependent force ripple model in the generalized disturbance, and adding an additional pole pair in the LTI system. Otherwise, the response to the force ripple could be erroneously estimated as structural resonance.

Coupled Z-B-C Axes

The Z-B-C axes are considered a coupled dynamic system due to the nature of its kinematic configuration. No significant structural resonance was observed in the collected data, therefore, the Z,

B, and C axes are consequently considered rigid body. Their 2×2 LTI models were configured as 5th-order following Eq. (4.17). The ball screw driven Z axis does not exhibit significant torque ripples. However, the direct drive B, and C axes do, which is accounted for in their models.

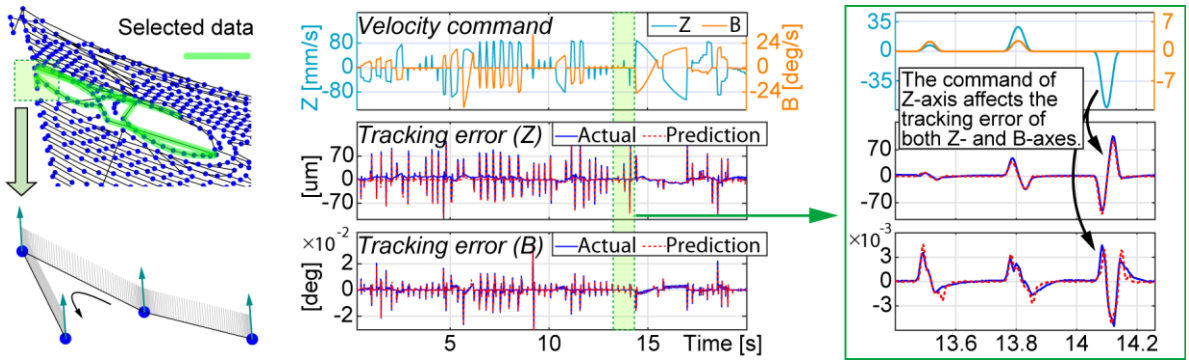

Figure 4-8 Predicted and experimental servo errors for coupled Z-B-axes.

A 20-second data packet was adopted to identify the models. The prediction results are shown in Figure 4-8. It shows the proposed model's ability to correctly estimate and predict the inter-axis coupling effects due to the coupled multibody dynamics. For example, described by the term $P_2^B \ddot{q}_Z \sin(q_B)$ in Eq. (3.15), the Z axis acceleration strongly influences the B axis motion. This relation can be observed during the time window in the highlighted green zone, corresponding to 14.0-14.2 s. Only the Z axis has a nonzero velocity command. However, the Z axis motion also causes considerable tracking error in the B axis, which is successfully predicted by the proposed model.

Overall, this is a significant improvement over earlier top-down LTI approaches [6][7][8][9], which fall short of capturing such coupled multibody effects and various disturbances.

4.3.2 Experimental Trunnion Table

An in-house trunnion table in the author's laboratory was also used to validate the proposed method. The feed drive is controlled by an ETEL controller, which contains a PID controller and feedforward velocity and acceleration compensation for the position control. As shown in Figure 4-9, the tilting axis is mounted on top of the linear axis, forming a coupled multibody dynamic system. Both linear and tilting axes are equipped with direct drive motors. Hence, the dynamic model takes position-dependent ripple into account. The tilting axis is supported by a pair of air bearings, and therefore no Stribeck effect is observed.

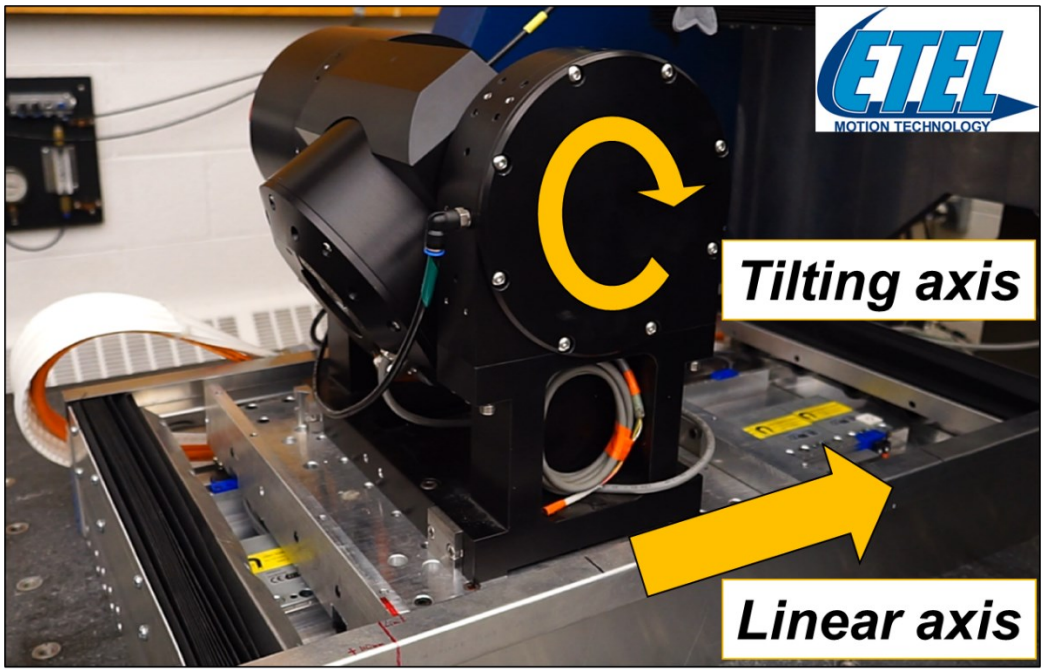

Figure 4-9 In-house linear-tilt-rotary feed drive.

Considering the mechanical features mentioned above, the dynamic models of the linear and tilting axes are derived as follows.

$$u_1 = \chi_{L_1}\ddot{q}_1 + \chi_{L_2}\left(\ddot{q}_2\cos(q_2) - \dot{q}_2{}^2\sin(q_2)\right) + \chi_{L_3}\dot{q}_1 + \chi_{L_4}sign(\dot{q}_1) + \chi_{L_5}sign(\dot{q}_1)e^{-|\dot{q}_1/\chi_{NL_1}|} + u_{p_1} \tag{4.26}$$

$$u_2 = \chi_{L_6}\ddot{q}_2 + \chi_{L_2}(\ddot{q}_1\cos(q_2) + g\sin(q_2)) + \chi_{L_7}\dot{q}_2 + \chi_{L_8}sign(\dot{q}_2) + u_{p_2} \tag{4.27}$$

u_1, u_2, q_1 and q_2 are the force/torque and the position of linear and tilting axis respectively. χ_{L_1}, …, $\chi_{L_8} \in \boldsymbol{\chi}_L$ are the linear parameters. $\chi_{NL_1} \in \boldsymbol{\chi}_{NL}$ is the nonlinear Stribeck friction velocity coefficient for the linear axis.

u_{p_1} and u_{p_2} represent all the position-dependent disturbance including motor force/torque ripple. In this case, the look up table approach, Eq. (3.11), proposed in Section 3.2 was employed. The sizes of grid are 1mm and 1 degree for the linear and tilting axis, respectively. A velocity threshold is applied so that the servo data in which the velocity of the linear axis is below 3 mm/s is excluded from the model identification.

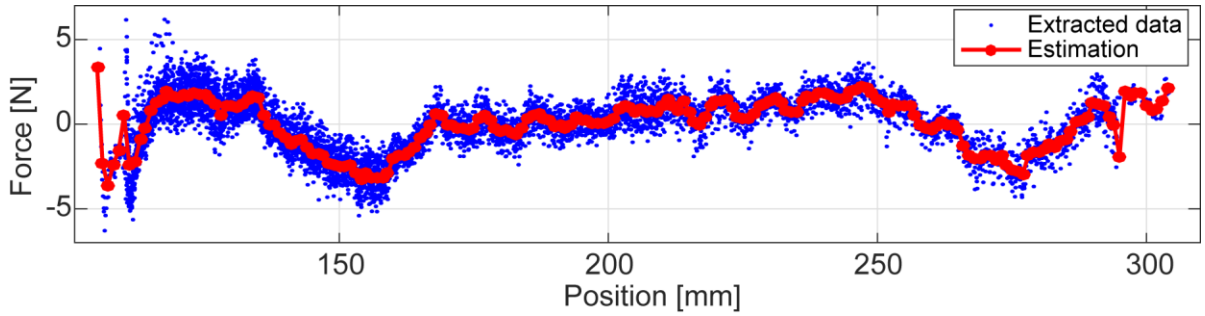

Figure 4-10 Position-dependent disturbance estimation, the linear axis.

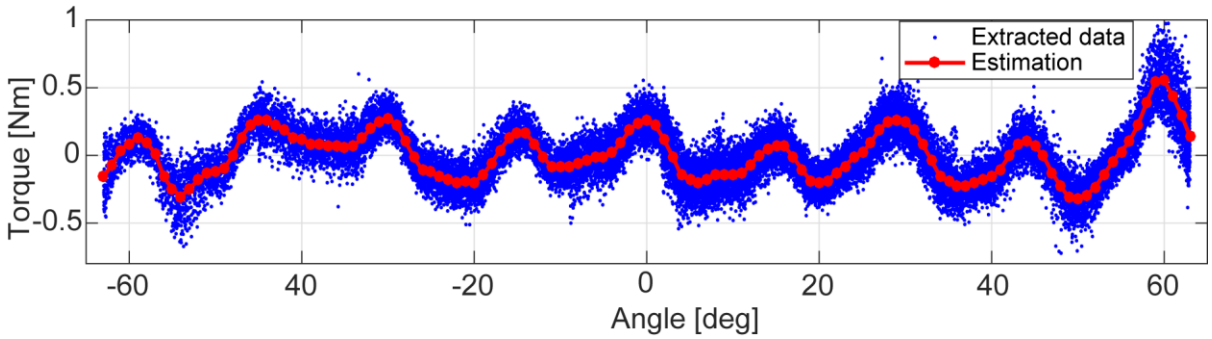

Figure 4-11 Position-dependent disturbance estimation, the tilting axis.

To demonstrate the proposed position-dependent disturbance model, the estimated disturbance (red line) overlapping with the extracted disturbance (blue dots) are shown in Figure 4-10 and Figure 4-11. The disturbance data were extracted from the motor force/torque signals by removing all other dynamic terms. As can be seen, the estimation well describes the extracted data. The pattern of the estimated force/torque ripple is not easy to describe with a simple analytical sinusoidal function. Irregular position-dependent disturbances at the travel ends of both axes are also observed. This could be attributed to the bent or stretched motor cable at these locations. This example shows that the proposed lookup table-based model is capable of estimating repeatable position-dependent disturbance with any arbitrary pattern. Since no structural resonance is observed, the mechanical structure is assumed rigid, and the MIMO LTI portion of the linear and tilting axes are both configured as a 5th-order 2×2 systems following Eq. (4.17).

The experimental and prediction results are shown in Figure 4-12. The 11-second implemented trajectory contains consecutive random back-and-forth simultaneous motion, which induces inter-axis dynamic effects. The data of commanded and actual motion as well as the motor signal were collected via the ETEL control system. The sampling rate is 250 Hz. The original motor signal is electrical current. Since it is an in-house experimental feed drive, the toque/force constant are known parameters.

Thus, the electrical current signal was converted to force and torque. The collected data was used to identify the machine model.

The pole locations estimated by the proposed pole search with LS projection method are listed in Table 4-4. The identified model is used to predict the system responses, which are overlaid with the measured data in Figure 4-12. The prediction errors are listed in Table 4-5. The average of the normalized RMS prediction error is 5.26%.

Table 4-4 Pole locations estimated by pole search with LS projection.

	Pole locations		Search bounds	
			Min.	Max.
Linear axis (1)	$p_{1,1}$ [Hz]	62.96	1	100
	$\omega_{n_{1,1}}$ [Hz]	10.86	1	100
	$\zeta_{1,1}$ []	0.6739	0.1	1.5
	$p_{2,1}$ & $p_{3,1}$ [Hz]	250, 250	Pre-assigned	
Tilting axis (2)	$p_{1,2}$ [Hz]	52.15	1	100
	$\omega_{n_{1,2}}$ [Hz]	7.61	1	100
	$\zeta_{1,2}$ []	0.8471	0.1	1.5
	$p_{2,2}$ & $p_{3,2}$ [Hz]	250, 250	Pre-assigned	

Table 4-5 Error of prediction.

	Linear axis		Tilting axis	
	Tracking error	Motor force	Tracking error	Motor torque
RMS error	1.490 [um]	2.631 [N]	2.228×10^{-3} [deg]	1.128×10^{-1} [Nm]
Normalized RMS error	7.12%	5.12%	6.15%	2.63%

Normalized RMS error = RMS error ÷ RMS magnitude

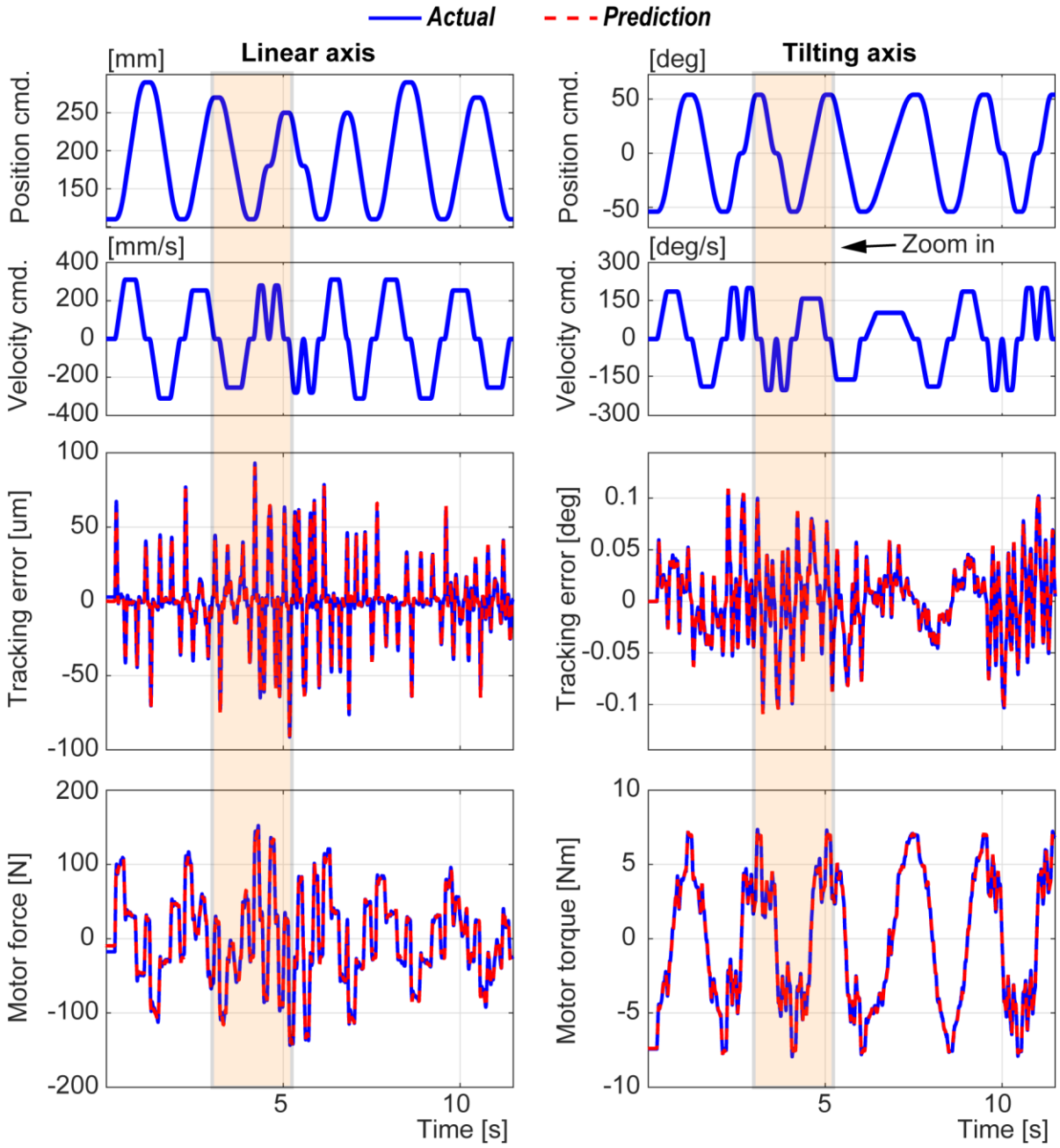

Figure 4-12 Prediction of tracking error and motor force/torque by the identified model.

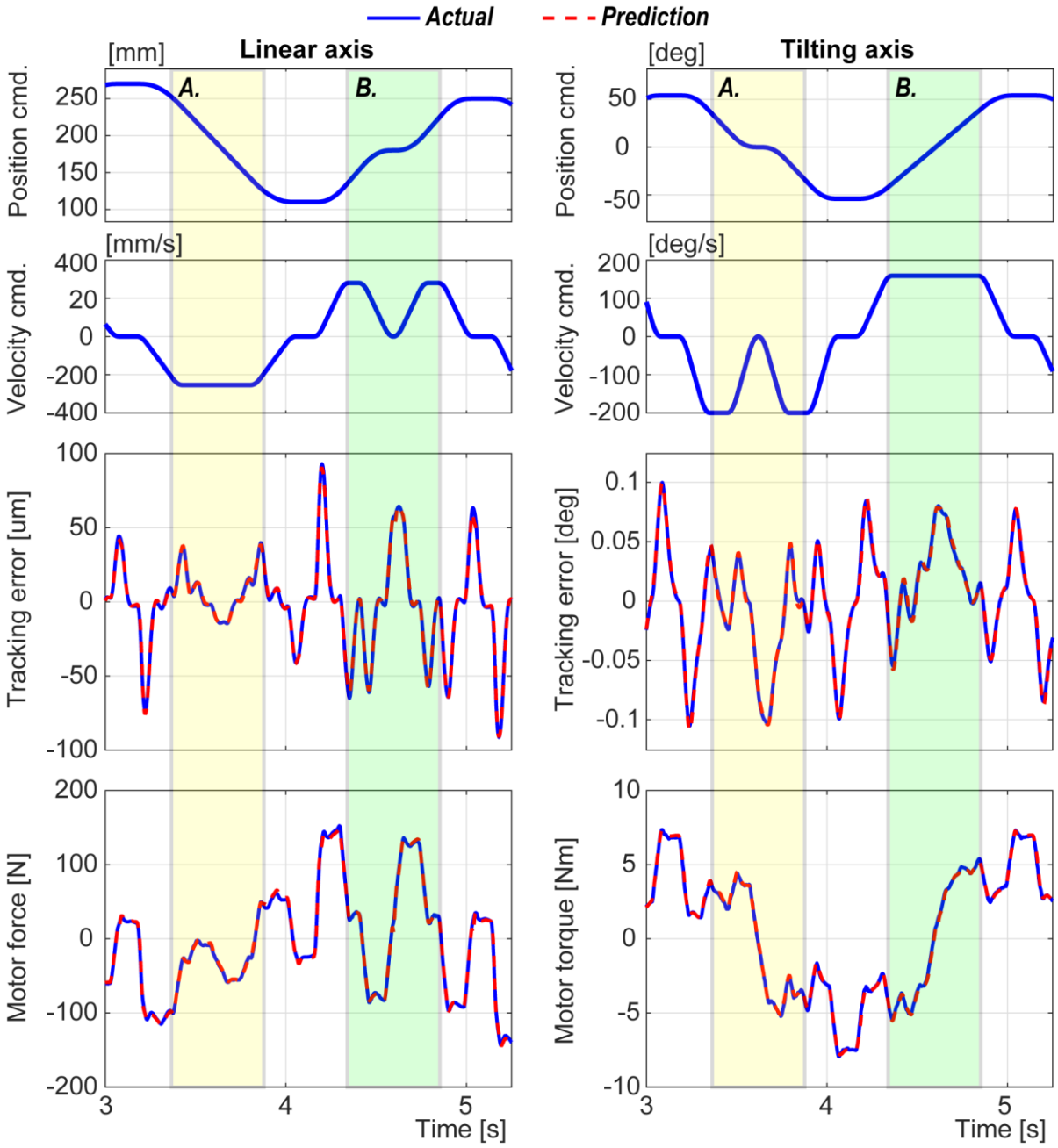

Figure 4-13 Experimental result and prediction (zoom-in 3~5.3 [s]).

Figure 4-13 is the highlighted orange zone in Figure 4-12. This figure showcases the capability of the proposed model to describe inter-axis coupled dynamics. In zone A (shown in yellow), linear axis velocity command is constant, which should have led to steady-state constant responses if it were a decoupled system. The tilting axis during this period is decelerating, then accelerating. The inertial

forces from the tilting axis, due to the coupled multibody dynamics, disturbs the tracking error and motor force in the linear axis. In zone B (shown in green), it is the opposite situation, where the inertial forces from the linear axis excites the tracking error and motor torque in the tilting axis.

As the illustration in Figure 4-14, since the proposed physics-based model is derived based on the machine configuration and other considered mechanical factors (friction, ripples, etc.), the generalized disturbance model can actually be decomposed such that the disturbances from each mechanical factor can be calculated individually (as $d1_i, d2_i$, ... in Figure 4-14). By integrating the identified transfer functions, the tracking error caused by each disturbance, as well as the position command, can be decomposed and calculated individually (as $e_{\dot{q}_{ri}}, e_{d1_i}, e_{d2_i}$, ... in Figure 4-14).

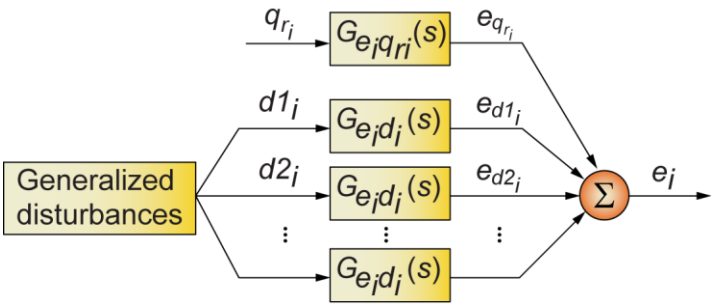

Figure 4-14 Decomposition of disturbances and the resultant tracking error.

Thus, each of the predicted disturbances and the resulting tracking error are plotted in Figure 4-15. The integration of the absolute values of each tracking error can also be displayed in pie charts (see Figure 4-16). Three types of disturbances are shown in the figures. It should be noted that position-dependent disturbance in the tilting axis includes not only the motor ripple but also the gravity torque, which is also purely position-dependent. The small and jerky spikes are motor ripple, while the slowly varying wave is gravity torque.

These figures become a useful tool for root cause analysis. For example, in Figure 4-15, at 3.2 seconds when both axes just start moving, the friction and the command tracking contribute almost the same amount of tracking error in the linear axis. In contrast, in the tilting axis, the command tracking is the dominant source of tracking error. Viewing the pie chart in Figure 4-16, for the tilting axis, friction is estimated to contribute very small (less than 1%) tracking error due to the air bearing mechanism, and position-dependent disturbance is comparatively a major source.

This example showcases the value of modeling and identification to provide insight into the machine and the process for facilitating machine troubleshooting and process modification. Furthermore, such

an approach can also be used to dynamically analyze and budget the sources of positioning errors in machine tools and other precision positioning systems, similar to the concept and benefits of dynamic error budgeting [113], but also with extension to multibody dynamics.

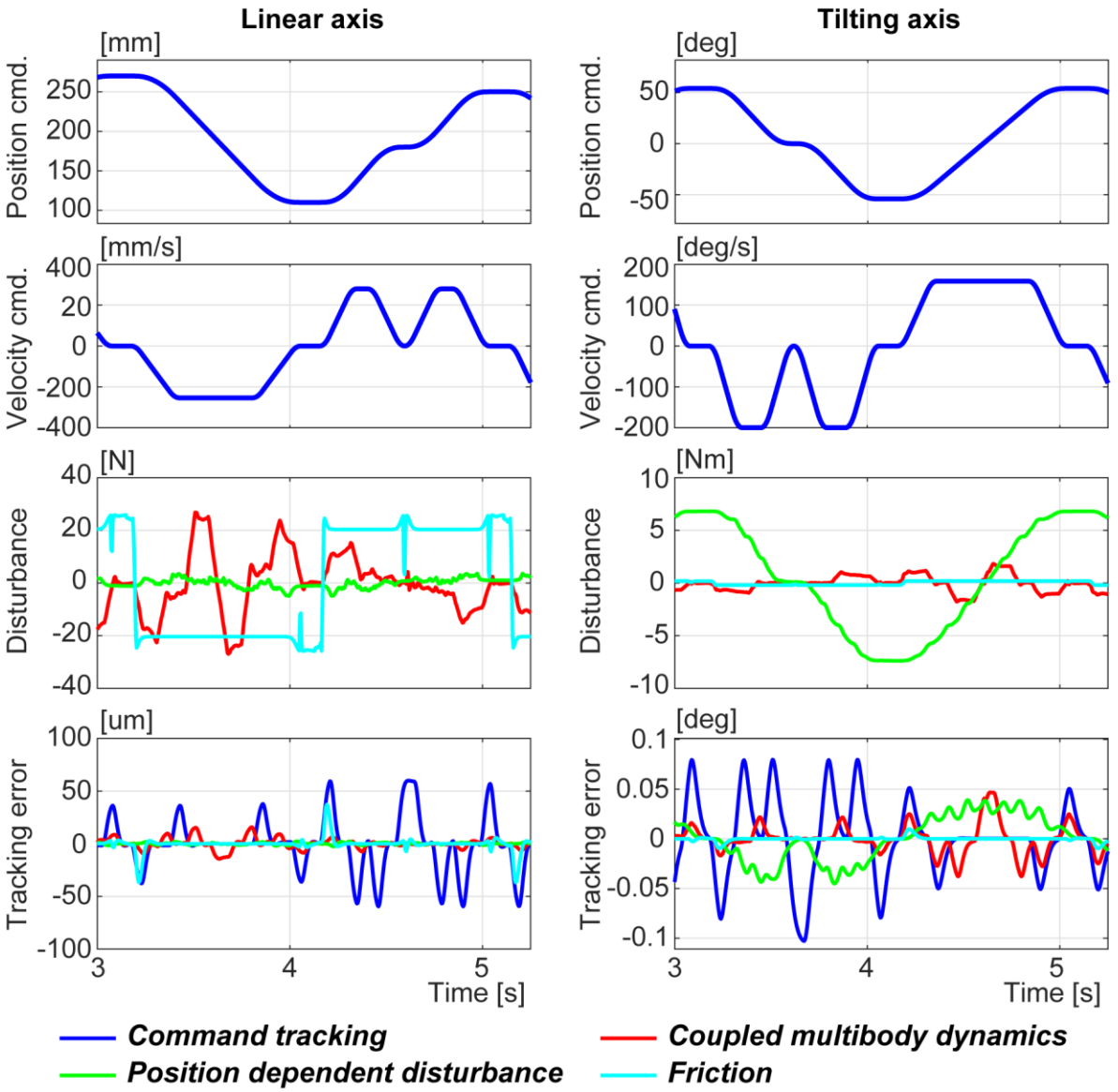

Figure 4-15 Decoupled predicted disturbances and tracking error (3~5.3 [s] section).

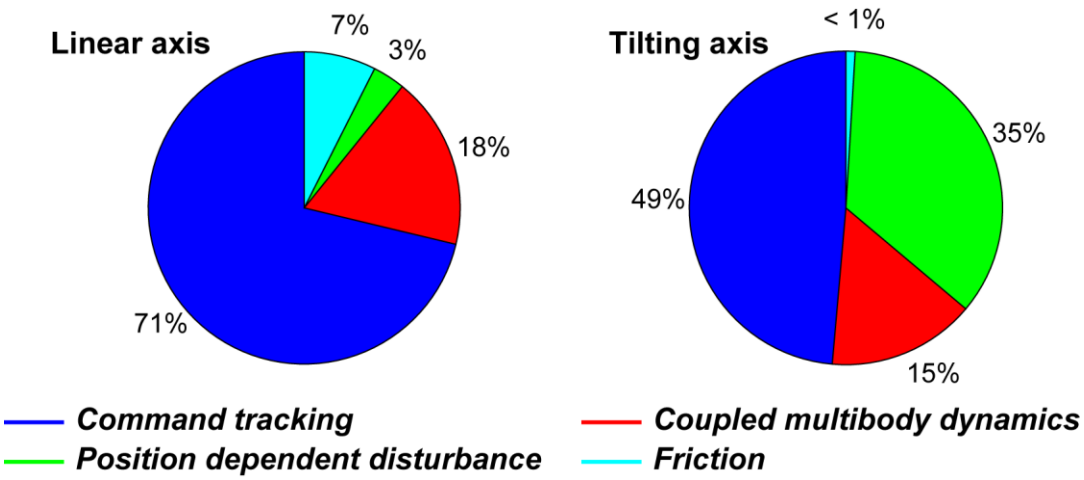

Figure 4-16 Tracking error statistics during 3~5.3 [s] section.

4.4 Conclusion

This chapter has introduced a new approach to build high-fidelity dynamic models of coupled multibody feed drive systems. The proposed model is configurable so that it is applicable to a broad class of machine tools and robots, for example with serial kinematics. The model estimation is highly efficient and accurate, due to the proposed decoupling of nonlinear and linear dynamics. The new approach has been demonstrated for digital twin estimation for a 5-axis laser drilling machine, via short packets of in-process CNC data. The tracking error due to inter-axis coupling effect is accurately modeled. Another validation was performed using an in-house trunnion table. The tracking error and motor signal in relation to the command input, multibody dynamics, motor ripple, and nonlinear friction were accurately simulated. In addition, the tracking error resulting from each individual disturbance source can be decoupled. This analysis can also provide useful insights into the machine and the process, to facilitate machine troubleshooting and process improvements.

Chapter 5
Identification of Multi-Axis Feed Drive Control System Considering Mechanical Flexibility

5.1 Introduction

The experimental validation presented in Chapter 4 assumes that the coupled multi-axis drives are rigid. However, this assumption may not be valid in situation where structural resonances are excited by the servo forces, especially in large-sized machine tools. This chapter illustrates how to extend the method proposed in Chapter 4 to further take into consideration the vibratory dynamics.

Figure 5-1 6-axis robot manipulators [114].

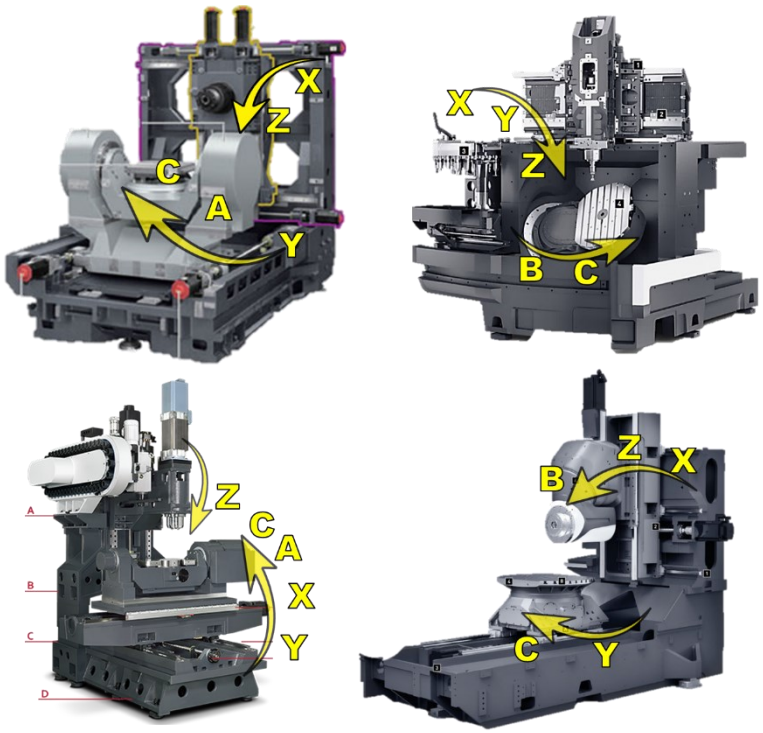

Figure 5-2 5-axis machines with different kinematic chains [45].

The modeling and identification of multibody dynamics considering structural flexibility have been studied in the field of robotics. An articulated robot, as shown Figure 5-1, is typically composed of consecutive revolute joints and arms. Thus, their mechanical flexibility can be systematically modeled by the flexible joint model and/or Euler–Bernoulli beams [57].

In contrast, the configuration of industrial machine tool is much more diverse. By observing existing 5-axis machines, as shown in Figure 5-2, characteristics specific to the 5-axis machines can be found. These observations define the scope of the study on this topic.

(a) In terms of the sequence of the kinematic chain of a multi-axis machine feed drive assembly, the rotary axes are normally placed on top of linear axes or just mounted on the fixed machine base frame.

(b) Rotary axes are either trunnion table carrying the workpiece or swivel head carrying the spindle. Both units may contain only one or two consecutive rotary axes.

(c) Rotary axes, whether they are a trunnion table unit or swivel head unit, are relatively rigid compared to the linear axes and machine frame. In other words, multi-axis machine tool drives can be assumed as flexible linear drives coupled with rigid rotary drives. This assumption corresponds to a recent study [115][116] which achieves accurate dynamic modeling by assuming rigid rotary axes, flexible linear axes, and a flexible machine base frame (see Figure 5-3).

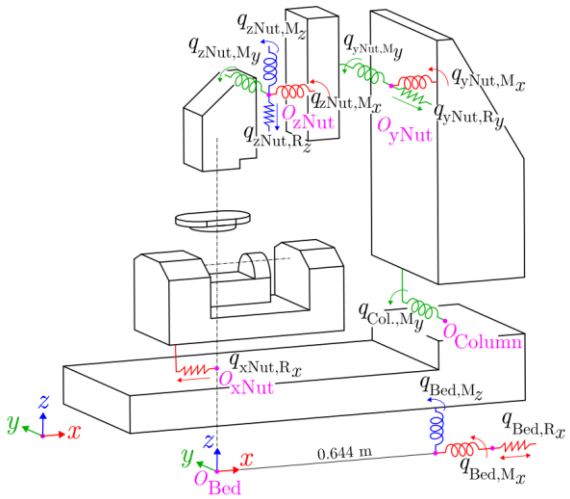

Figure 5-3 Multibody model with flexible joints of a 5-axis machine [115].

According to the above observations, in Section 5.2, a general linear feed drive structure is considered, where the vibratory dynamics can be classified into four different types. In Section 5.3, two cases of a flexible linear drive coupled with a rotary drive are discussed. Case 1, discussed in Section 5.3.1, covers the first three types studied in Section 5.2, and Case 2, discussed in Section 5.3.2, covers the fourth. It is found that if there is significant mechanical flexibility within the connection of a linear drive and a rotary drive, then the position data from CNC is insufficient for the proposed model identification method. An extra motion sensor is required to capture the relative vibration between the linear and

rotary axes. The case requiring an extra motion sensor is further studied and verified in the later chapters.

5.2 Classification of Vibratory Dynamics of a General Linear Feed Drive

A general flexible linear feed drive has four types of typical vibratory dynamics [117] which can be excited by the servo force (see Figure 5-4). u_L and q_L represent the servo force and the position measurement for the feedback control, respectively.

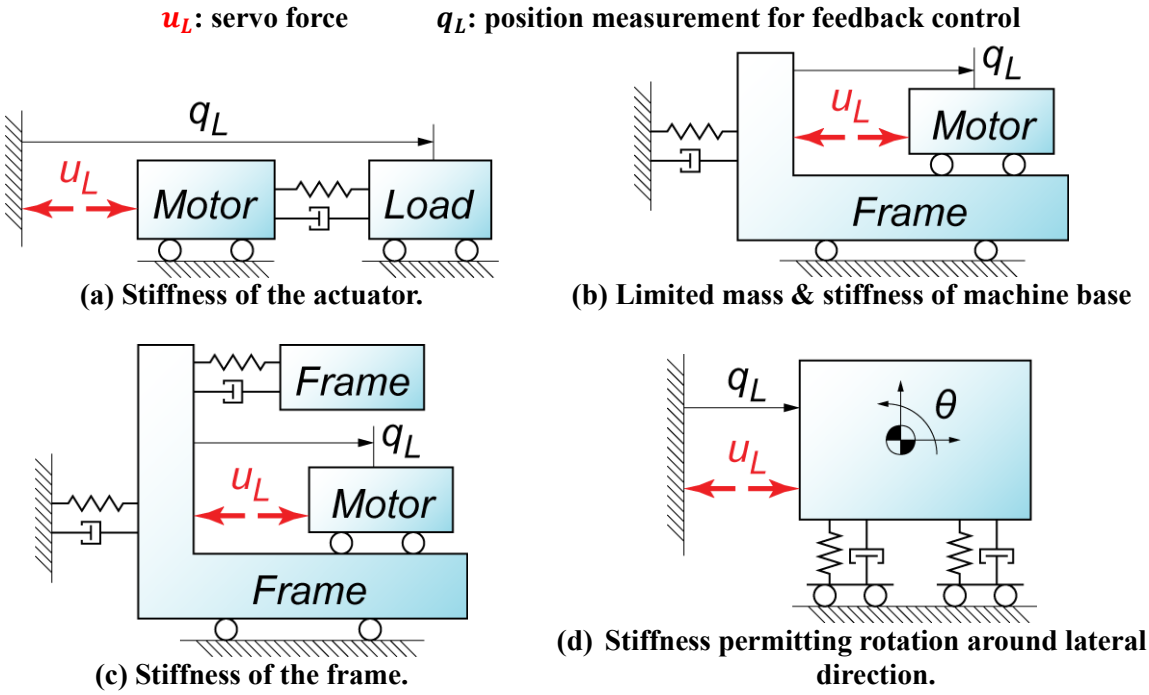

Figure 5-4 Four types of vibratory dynamics for a general linear feed drive [117].

Type (a.): Stiffness of the actuator. This case refers to the stiffness of the structure connecting the motor and the load (table or spindle). The spring in the figure could refer to a ball screw, gear, or belt [118]. If the position of the load side is chosen to be the measurement feedback, such additional vibratory dynamics between the motor and the load may lead to 180-degree phase lag without anti-resonance.

Type (b.): Limited mass & stiffness of machine base. When a machine tool is placed on the ground and supported by the leveling feet, its own weight is the normal force creating the contact stiffness. Then, such stiffness together with the entire machine mass lead to low-frequency vibratory mode, where the machine as a whole vibrates with respect to the ground.

Type (c.): Stiffness of the frame. The machine frame as an overhang structure carries the kinematic chains for the tool and the workpiece. Typically, larger workspace is achieved by a longer or higher overhang structure, thus leading to lower rigidity. Such resonance can be excited by the reaction of the servo force acting on the machine frame.

Type (d.): Stiffness permitting rotation around lateral direction. If the servo force is not aligned with the center of mass (COM) of the moving part, such off-centered force generates a torque that could excite the rotational vibration mode. The stiffness to resist the applied torque could be the stiffness of the guideway or the stiffness of overhang structure of the moving part. Figure 5-5 is an example highlighting the off-centered servo force. The principle of Drive at the Center of Gravity (DCG) [120] is a way to circumvent this issue. Box-in-box design, as shown in Figure 5-6, is a design following this concept to generate the resultant driving force close to the COM, however, with the cost of one more servo system.

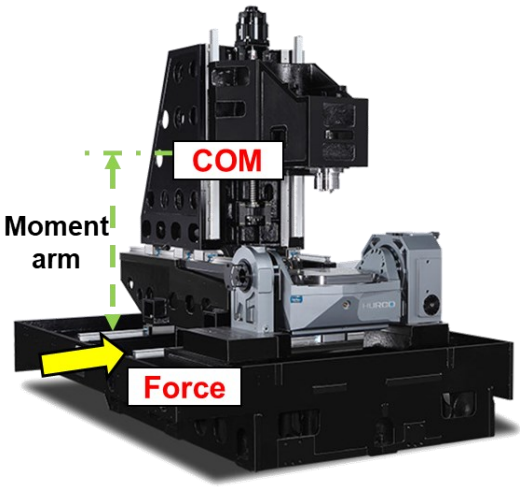

Figure 5-5 Moving column design [119].

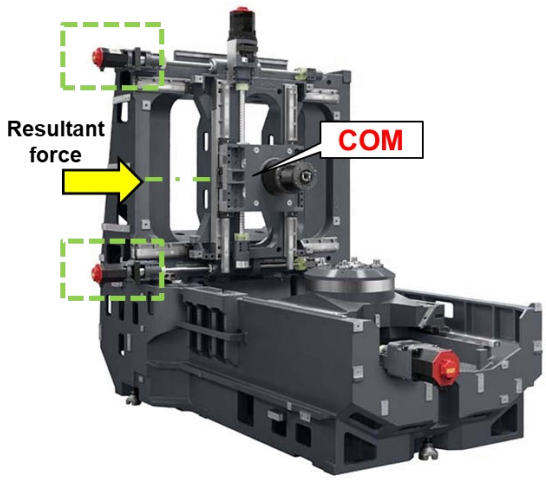

Figure 5-6 Box-in-box design [45].

5.3 Cases Studies on a Linear Drive Coupled with a Rotary Drive

In this section, a rotary drive is added onto the general linear drive illustrated in Section 5.2. Type (a), (b), and (c) are discussed in Section 5.3.1. Type (d) is particularly discussed in Section 5.3.2 since it requires an extra motion sensor for the model identification.

5.3.1 Case 1: Flexible Linear Drive Rigidly Coupled with a Rotary Drive (Generalization of Type a, b, and c)

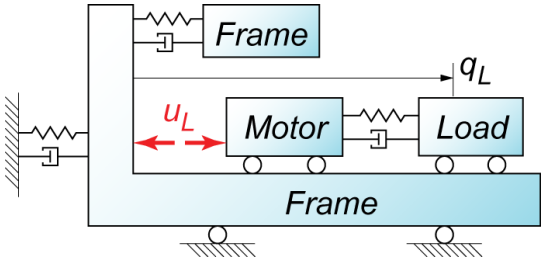

Figure 5-7 A general expression of type (a), (b), and (c) vibratory dynamics.

The vibratory dynamics of the type (a), (b), and (c) in Section 5.2 can be generally presented as Figure 5-7. This flexible linear drive can be transformed into a equivalent N-degrees of freedom (DOF) (denoted as $1,2,\dots,L,\dots N$) mass-spring-damper system, as conceptually shown in Figure 5-8. q_L is the position measured by the linear encoder for the feedback control. If a translational mass m_L is rigidly attached with a rotary drive (denoted as R), the equations of motions can be derived as follows.

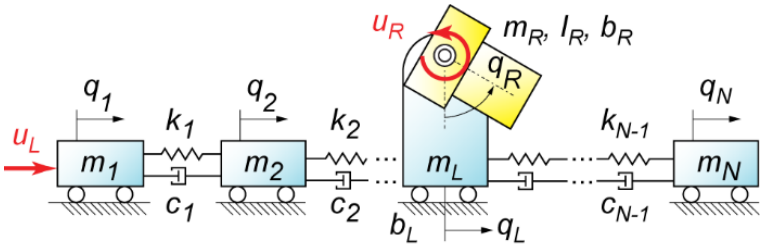

Figure 5-8 Expression of a linear flexible drive coupled with a rotary drive.

$$\begin{cases} u_L = m_1\ddot{q}_1 + c_1(\dot{q}_1 - \dot{q}_2) + k_1(q_1 - q_2) \\ \quad\vdots \\ 0 = m_L\ddot{q}_L + b_L\dot{q}_L - c_{L-1}(\dot{q}_{L-1} - \dot{q}_L) - k_{L-1}(q_{L-1} - q_L) + c_L(\dot{q}_L - \dot{q}_{L+1}) + k_L(q_L - q_{L+1}) + d_L \\ \quad\vdots \\ 0 = m_N\ddot{q}_N - c_{N-1}(\dot{q}_{N-1} - \dot{q}_N) - k_{N-1}(q_{N-1} - q_N) \\ u_R = m_R\ddot{q}_R + b_R\dot{q}_R + d_R \end{cases} \tag{5.1}$$

The generalized disturbances, d_L and d_R, capturing all the nonlinear and coupling terms such as coupled multibody dynamics and friction, can be derived as

$$\begin{cases} d_L = \chi_R\left(\ddot{q}_R \cos(q_R) - \dot{q}_R{}^2 \sin(q_R)\right) + u_{f_L}(\dot{q}_L) + u_{p_L}(q_L) \\ d_R = \chi_R(\ddot{q}_L \cos(q_R) + g \sin(q_R)) + u_{f_R}(\dot{q}_R) + u_{p_R}(q_R) \end{cases} \tag{5.2}$$

χ_R is an inertial parameter, and u_{f_L}, u_{f_R}, u_{p_L}, and u_{p_R} are nonlinear friction and position-dependent disturbance respectively. Eq. (5.1) and Eq. (5.2) can be visualized as the block diagram shown in Figure 5-9 (a). The generalized disturbance block represents Eq. (5.2), where the inputs q_L and q_R can be measured via the feed drives' encoders. Since the N-DOF mass-spring-damper system are linear, the relation between u_L and q_L can be expressed by a high-order transfer function $P_L(s)$. The same expression applies to the rotary axis, denoted as $P_R(s)$. Then, Figure 5-9 (a) can be rearranged as Figure 5-9 (b).

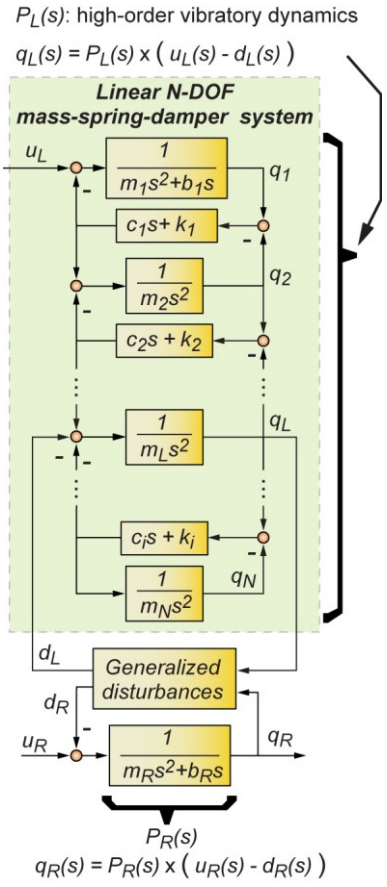

(a) Open-loop dynamics.

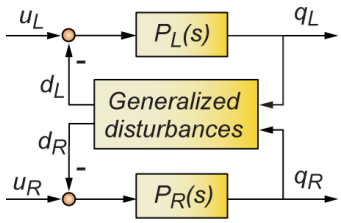

(b) Open-loop dynamics expressed by $P_L(s)$, $P_R(s)$, and generalized disturbance.

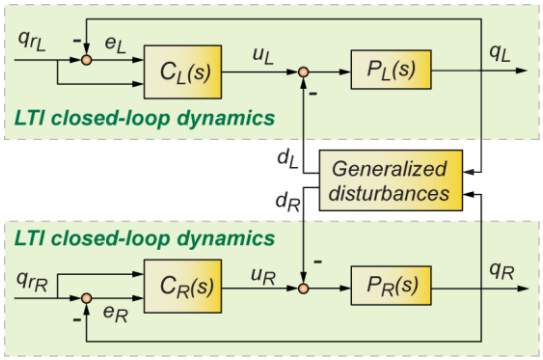

(c) LTI closed-loop dynamics coupled with generalized disturbance.

Figure 5-9 Block diagram for Case 1: flexible linear drive rigidly coupled with a rotary drive.

The open-loop dynamic model can be integrated with LTI feedback and feedforward controllers $C_L(s)$ and $C_R(s)$, as shown in Figure 5-9 (c), where the generalized disturbance is isolated from the LTI

closed-loop dynamics. This framework fits the proposed equivalent model representation illustrated as Figure 4-2 where the order of MIMO LTI model can be configured depending on the number of the observed vibratory modes.

The model can be identified following the procedure illustrated in Section 4.2.4. Step one is the parameter identification of the open-loop dynamics, Eq. (5.1) and Eq. (5.2). If applying smooth (low-jerk) trajectory where structural vibration would not be excited, Eq. (5.1) and Eq. (5.2) can be simplified as a rigid body model:

$$\begin{cases} u_L = m_L'\ddot{q}_L + b_L\dot{q}_L + \chi_R\left(\ddot{q}_R\cos(q_R) - \dot{q}_R{}^2\sin(q_R)\right) + u_{f_L}(\dot{q}_L) + u_{p_L}(q_L) \\ u_R = m_R\ddot{q}_R + b_R\dot{q}_R + \chi_R(\ddot{q}_L\cos(q_R) + g\sin(q_R)) + u_{f_R}(\dot{q}_R) + u_{p_R}(q_R) \end{cases} \quad (5.3)$$

Then, step one can be done by simply using the servo data q_L, q_R, u_L, and u_R collected from the CNC. Step two is to build the predicted generalized disturbance $\hat{\boldsymbol{d}}$ by the collected data and Eq. (5.2). The identification of the MIMO LTI model, step 3, can be performed using the predicted $\hat{\boldsymbol{d}}$ along with the collected signals of q_{r_L}, q_{r_R}, e_L, e_R, u_L, and u_R from the CNC. Therefore, in this case, no extra sensor is required. The servo data from the CNC is sufficient to build the feed drive's model.

5.3.2 Case 2: Linear Drive and Rotary Drive Connected by Flexible Structure (Type d)

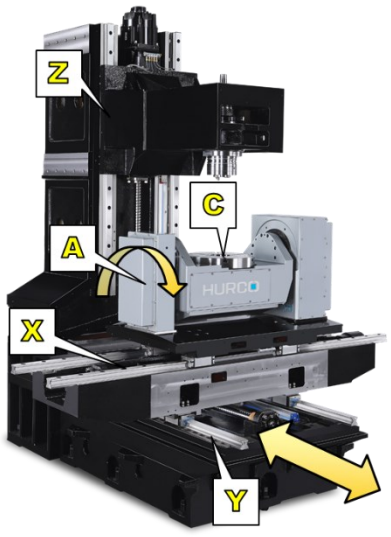

Figure 5-10 5-axis machining center with a moving trunnion unit [119].

A typical example of Case 2 is shown as Figure 5-10. A trunnion unit (A & C axes) together with a linear X axis are mounted on top of a linear Y axis driven by a ball screw at the bottom. Such driving

force is far away from the COM of the entire moving part. Additionally, Y-X-A axes are linked by two sets of linear guideways, causing considerable structural compliance. Therefore, the linear Y axis and the rotary A axis constitute a coupled multibody system with flexible connection, which falls into this category.

This case can be expressed as a lumped mass-spring-damper model shown in Figure 5-11. The linear Y axis comprises a linear mass m_Y attached to a rigid link by a torsional spring-damper (k_δ and c_δ). The rotary drive (A axis) is attached to the link by a revolute joint. The deflection angle of the spring-damper joint is denoted as q_δ. To avoid confusion, please note that δ is not Kronecker delta from tensor notation.

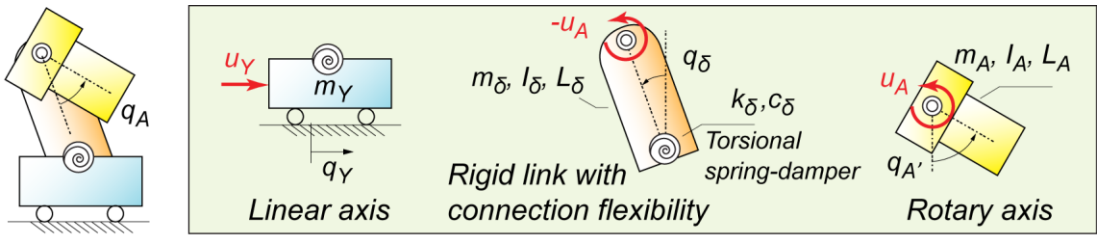

u_Y: linear motor input u_Y: rotary motor input

q_Y: linear encoder q_A: rotary encoder $q_{A'} = q_A + q_\delta$

q_δ: missing state. Require extra motion sensor.

Figure 5-11 A linear drive and a rotary drive connected by a rigid link with connection flexibility.

The motion of the linear drive q_Y and the rotary drive relative to its support (rigid link) q_A are measured by the encoders for the feedback control. However, the deflection angle of the rigid link q_δ is not detected. The angle of the rotary drive in a global inertial frame $q_{A'}$ is also not known, i.e., $q_{A'} = q_\delta + q_A$. Based on Figure 5-11, the dynamic equations of the three bodies can be derived as:

$$\begin{cases} u_Y = m_Y \ddot{q}_Y + b_Y \dot{q}_Y + d_Y \\ -u_A = I_\delta \ddot{q}_\delta + c_\delta \dot{q}_\delta + k_\delta q_\delta - b_A \dot{q}_A + d_\delta \\ u_A = I_A \ddot{q}_{A'} + b_A \dot{q}_A + d_A \end{cases} \tag{5.4}$$

The generalized disturbances $\boldsymbol{d} = [d_Y \; d_\delta \; d_A]^{\boldsymbol{T}}$ are derived as

$$\begin{cases} d_Y = \mu\left(\dot{q}_\delta{}^2 \sin(q_\delta) - \ddot{q}_\delta \cos(q_\delta)\right) + \rho\left(\ddot{q}_{A'} \cos(q_{A'}) - \dot{q}_{A'}{}^2 \sin(q_{A'})\right) + u_{f_Y} + u_{p_Y} \\ d_\delta = \lambda\left(-\ddot{q}_{A'} \cos(q_A) + \dot{q}_{A'}{}^2 \sin(q_A)\right) - \mu \ddot{q}_Y \cos(q_\delta) - \varphi \sin(q_\delta) - u_{f_A} - u_{p_A} \\ d_A = \lambda\left(-\ddot{q}_\delta \cos(q_A) - \dot{q}_\delta{}^2 \sin(q_A)\right) + \rho \ddot{q}_Y \cos(q_{A'}) + \psi \sin(q_{A'}) + u_{f_A} + u_{p_A} \end{cases} \tag{5.5}$$

The physical significance of the parameters are listed in Table 5-1. Eq. (5.4) is the linear open-loop dynamics. Eq. (5.5) is d_Y, d_δ, and d_A associated with each of the three bodies. They represent generalized disturbances containing the rest of nonlinear open-loop dynamics.

Table 5-1 Descriptions of the parameters in Eq. (5.4) and Eq. (5.5).

μ, ρ, λ, ψ, and φ	Machine inertial parameters
c_δ and k_δ	Coefficients of the torsional spring-damper
b_Y and b_A	Viscous damping at the joints
u_{f_Y} and u_{f_A}	Nonlinear friction at the joints
u_{p_Y} and u_{p_A}	Position-dependent disturbances, Eq. (3.11)
m_Y, m_δ, and m_A	Mass
I_δ and I_A	Diagonal inertia

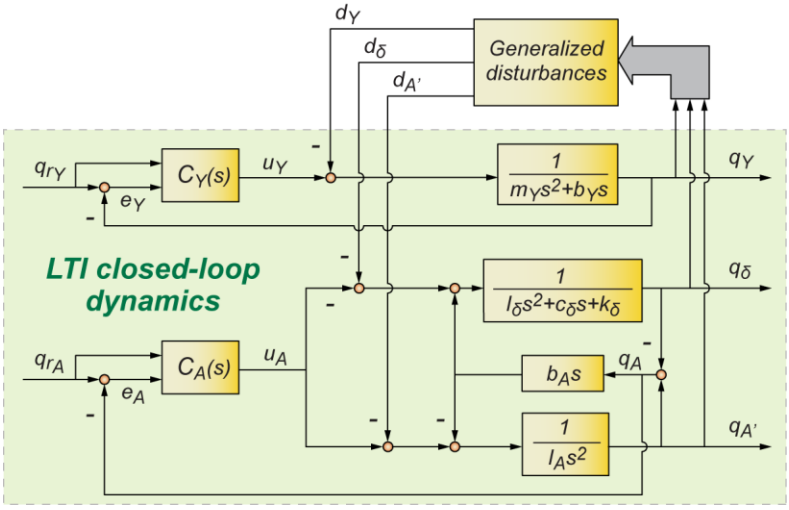

Figure 5-12 Block diagram for Case 2: linear drive and rotary drive connected by flexible structure.

After integrating general LTI feedback and feedforward controllers, $C_Y(s)$ and $C_A(s)$, as Eq. (4.11), the system can be visualized by the block diagram shown in Figure 5-12. As can be seen, the motor torque of the rotary drive u_A is computed by the controller $C_A(s)$. Then, this torque and its reaction are applied to the motor shaft I_A and the rigid link I_δ fixed by the torsional spring-damper (k_δ and c_δ) respectively. Their relative motion at the revolute joint generates viscous damping torque, feeding back to these two bodies.

As the identification procedure elaborated in Section 4.2.4, step 4.1 utilizes the collected data to perform the identification of open-loop dynamics. Viewing the dynamic equations Eq. (5.4) and Eq. (5.5), the required data are the motor inputs $[u_Y, u_A]$ as well as the joint variables $[q_Y, q_\delta, q_A, q_{A'}]$ and

their *1*st *2*nd time derivative terms. On the other hand, step 4.2 calculates the predicted generalized disturbance $\widehat{\boldsymbol{d}}$ as Eq. (5.5), which again requires the joint variables $[q_Y, q_\delta, q_A, q_{A\prime}]$ and their time derivatives.

q_Y and q_A are the axis encoder readings and can be directly accessed from the CNC. However, it is not possible to determine q_δ and $q_{A\prime}$ by $q_A = q_{A\prime} - q_\delta$ if only q_A is given. Hence, unlike the previous Case 1, the identification of this closed-loop system requires an extra motion sensor to measure q_δ and/or $q_{A\prime}$. For this purpose, an IMU will be used to reconstruct the angular velocity and acceleration of the structural deflection angle, $\dot{q}_\delta$ and $\ddot{q}_\delta$. Details of the measurement procedure will be presented in the next chapter.

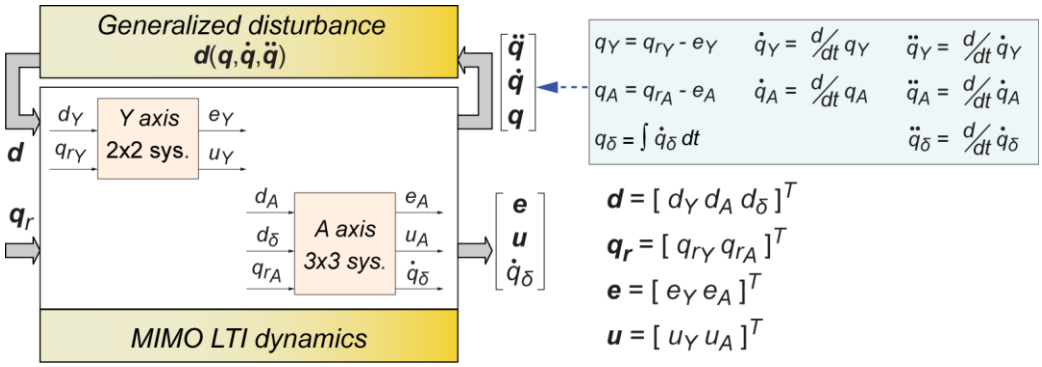

Figure 5-13 Equivalent model: MIMO LTI system coupled with generalized disturbance.

According to the above discussion, the equivalent expression of this multi-axis control system can be expressed as Figure 5-13. The generalized disturbance block represents Eq. (5.5), containing the nonlinear dynamics of the three bodies. The MIMO LTI block contains the subsystems for the Y and A axes. Since there are two bodies (I_δ, and I_A) in the A-axis control loop, the disturbance inputs become d_A and d_δ for each body. $\dot{q}_\delta$ is configured as an extra output of the A-axis subsystem. By integrating and differentiating $\dot{q}_\delta$, then q_δ and $\ddot{q}_\delta$ can also be derived for the computation of $\boldsymbol{d}$.

The closed-loop LTI portion of the dynamics for the Y-axis is a 2×2 system as

$$\begin{cases} e_Y(s) = G_{e_Y d_Y}(s) d_Y(s) + G_{e_Y q_{r_Y}}(s) q_{r_Y}(s) \\ u_Y(s) = G_{u_Y d_Y}(s) d_Y(s) + G_{u_Y q_{r_Y}}(s) q_{r_Y}(s) \end{cases} \tag{5.6}$$

$$G_{ij}(s) = {}^{N_{ij}(s)}\!/_{D_Y(s)};\ \ i \in [e_Y\ u_Y];\ \ j \in \left[d_Y\ q_{r_Y}\right]$$

Regarding the order of the system (see the assumptions listed in Table 4-1), considering the velocity and acceleration feedforward control, two high-frequency real poles are pre-assigned. The integral control along with a rigid body contributes one complex pole pair and one real pole. In total, the characteristic polynomial $D_Y(s)$ of the Y-axis subsystem can be configured as a *5*th-order system with three real poles and one complex pole pair. According to the block diagram shown in Figure 5-12, the respective characteristic polynomials $D_Y(s)$ and numerator polynomials $N_{ij}(s)$ of each transfer function can be derived as:

$$\begin{cases} D_Y(s) = \mathbf{\Pi}_{m=1}^{3}\mathbf{\Pi}_{k=1}^{1}\left(s + p_{m,Y}\right)\left(s^2 + 2\zeta_{k,Y}\omega_{n_{k,Y}}s + {\omega_{n_{k,Y}}}^2\right) \\ N_{e_Y d_Y}(s) = b_1^{e_Y d_Y}s^1 + b_2^{e_Y d_Y}s^0 \\ N_{e_Y q_{r_Y}}(s) = b_1^{e_Y q_{r_Y}}s^5 + b_2^{e_Y q_{r_Y}}s^4 + b_3^{e_Y q_{r_Y}}s^3 + b_4^{e_Y q_{r_Y}}s^2 + b_5^{e_Y q_{r_Y}}s^1 \\ N_{u_Y d_Y}(s) = b_1^{u_Y d_Y}s^2 + b_2^{u_Y d_Y}s^1 + \mathbf{\Pi}_{m=1}^{3}\mathbf{\Pi}_{k=1}^{1}p_{m,Y}{\omega_{n_{k,Y}}}^2 \\ N_{u_Y q_{r_Y}}(s) = b_1^{u_Y q_{r_Y}}s^5 + b_2^{u_Y q_{r_Y}}s^4 + b_3^{u_Y q_{r_Y}}s^3 + b_4^{u_Y q_{r_Y}}s^2 + b_5^{u_Y q_{r_Y}}s^1 \end{cases} \tag{5.7}$$

On the other hand, due to the additional d_δ and $\dot{q}_\delta$, the A-axis can be defined as a 3×3 system:

$$\begin{cases} e_A(s) = G_{e_A d_A}(s)d_A(s) + G_{e_A d_\delta}(s)d_\delta(s) + G_{e_A q_{r_A}}(s)q_{r_A}(s) \\ u_A(s) = G_{u_A d_A}(s)d_A(s) + G_{u_A d_\delta}(s)d_\delta(s) + G_{u_A q_{r_A}}(s)q_{r_A}(s) \\ \dot{q}_\delta(s) = G_{\dot{q}_\delta d_A}(s)d_A(s) + G_{\dot{q}_\delta d_\delta}(s)d_\delta(s) + G_{\dot{q}_\delta q_{r_A}}(s)q_{r_A}(s) \end{cases} \tag{5.8}$$

$$G_{ij}(s) = {N_{ij}(s)}/{D_A(s)};\ \ i \in [e_A\ u_A\ \dot{q}_\delta];\ \ j \in \left[d_A\ d_\delta\ q_{r_A}\right]$$

Compared to the Y-axis, the A-axis contains one more body (the rigid link and the rotary drive), resulting in one more complex pole pair. Hence, the characteristic polynomial $D_A(s)$ of A-axis subsystem is configured as a *7*th-order system with three real poles and two complex pole pairs. According to the block diagram shown in Figure 5-12, the respective characteristic polynomials $D_A(s)$ and numerator polynomials $N_{ij}(s)$ of each transfer function can be derived as:

$$
\begin{cases}
D_A(s) = \mathbf{\Pi}_{m=1}^{3}\mathbf{\Pi}_{k=1}^{2}\left(s + p_{m,A}\right)\left(s^2 + 2\zeta_{k,A}\omega_{n_{k,A}}s + {\omega_{n_{k,A}}}^2\right) \\
N_{e_A d_A}(s) = b_1^{e_A d_A}s^3 + b_2^{e_A d_A}s^2 + b_3^{e_A d_A}s^1 + b_4^{e_A d_A}s^0 \\
N_{e_A d_\delta}(s) = b_1^{e_A d_\delta}s^3 + b_2^{e_A d_\delta}s^2 + b_3^{e_A d_\delta}s^1 \\
N_{e_A q_{r_A}}(s) = b_1^{e_A q_{r_A}}s^7 + b_2^{e_A q_{r_A}}s^6 + b_3^{e_A q_{r_A}}s^5 + b_4^{e_A q_{r_A}}s^4 + b_5^{e_A q_{r_A}}s^3 + b_6^{e_A q_{r_A}}s^2 + b_7^{e_A q_{r_A}}s^1 \\
N_{u_A d_A}(s) = b_1^{u_A d_A}s^4 + b_2^{u_A d_A}s^3 + b_3^{u_A d_A}s^2 + b_4^{u_A d_A}s^1 + \mathbf{\Pi}_{m=1}^{3}\mathbf{\Pi}_{k=1}^{2}p_{m,A}{\omega_{n_{k,A}}}^2 \\
N_{u_A d_\delta}(s) = b_1^{u_A d_\delta}s^4 + b_2^{u_A d_\delta}s^3 + b_3^{u_A d_\delta}s^2 + b_4^{u_A d_\delta}s^1 \\
N_{u_A q_{r_A}}(s) = b_1^{u_A q_{r_A}}s^7 + b_2^{u_A q_{r_A}}s^6 + b_3^{u_A q_{r_A}}s^5 + b_4^{u_A q_{r_A}}s^4 + b_5^{u_A q_{r_A}}s^3 + b_6^{u_A q_{r_A}}s^2 + b_7^{u_A q_{r_A}}s^1 \\
N_{\dot{q}_\delta d_A}(s) = b_1^{\dot{q}_\delta d_A}s^3 + b_2^{\dot{q}_\delta d_A}s^2 + b_3^{\dot{q}_\delta d_A}s^1 \\
N_{\dot{q}_\delta d_\delta}(s) = b_1^{\dot{q}_\delta d_\delta}s^4 + b_2^{\dot{q}_\delta d_\delta}s^3 + b_3^{\dot{q}_\delta d_\delta}s^2 + b_4^{\dot{q}_\delta d_\delta}s^1 \\
N_{\dot{q}_\delta q_{r_A}}(s) = b_1^{\dot{q}_\delta q_{r_A}}s^6 + b_2^{\dot{q}_\delta q_{r_A}}s^5 + b_3^{\dot{q}_\delta q_{r_A}}s^4 + b_4^{\dot{q}_\delta q_{r_A}}s^3 + b_5^{\dot{q}_\delta q_{r_A}}s^2
\end{cases}
\tag{5.9}
$$

In the later chapters, the identification of this case will be particularly studied and validated with the use of an IMU to capture the coupled feed drive structural vibration ($\dot{q}_\delta$ and $\ddot{q}_\delta$).

5.4 Conclusion

This chapter introduces structural flexibility into the model and identification method proposed in Chapter 4. By reviewing the 5-axis machine kinematics and the vibratory dynamics of a general linear drive, two cases of a linear drive coupled with a rotary drive are studied. It is found that if a rotary drive is rigidly attached to a flexible linear drive (Case 1), then the servo data from the CNC are sufficient to identify the dynamic model of this multi-axis feed drive control system. The machine flexibility is considered by a higher-order MIMO LTI model.

However, if there is significant mechanical flexibility between a linear drive and a rotary drive (Case 2), then the servo data from the CNC is insufficient for the proposed identification method. An extra motion sensor is required to capture the vibration between the linear and rotary axis, $\dot{q}_\delta$.

Case 2 which requires an extra motion sensor will be particularly studied in the following chapters. Chapter 6 will present the application of an IMU to capture the missing internal structural vibration. In Chapter 7, the servo data from CNC along with the vibration measured by the IMU will be applied to identify the dynamic model of the feed drive control system developed in this chapter.

Chapter 6
Use of IMUs for Capturing the Vibration of Multi-Axis Drives

6.1 Introduction

The identification method proposed in Chapter 4 considers rigid multi-axis drives which, in reality, could be flexible. According to the analysis of Case 2 in Section 5.3.2, if there is significant mechanical flexibility between a linear drive and a rotary drive, the servo data from the CNC is insufficient for the proposed model identification method. The internal vibration between the linear and rotary drives are necessary information as well. Case 2 in Section 5.3.2 is experimentally studied in Chapter 6 and Chapter 7. In this chapter, a methodology to capture the internal vibration by an IMU is proposed and verified.

This chapter is organized as follows. Section 6.2 introduces an experimental setup prepared for this study. Section 6.3 introduces fundamental data processing techniques for MEMS IMUSs, e.g., strapdown integration and sensor fusion. Section 6.4 describes the procedure of reconstructing the internal structural vibration by incorporating the collected IMU data and encoder data. The implementation results are presented in Section 6.5. In the next chapter, the reconstructed vibration will be used in the identification for building the dynamic model of multi-axis flexible drives.

6.2 Experimental Setup

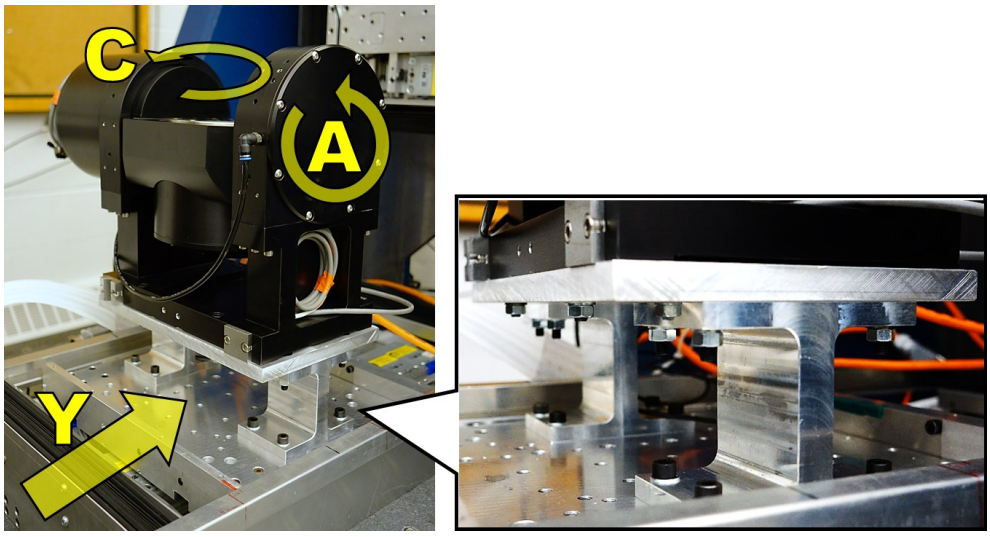

Figure 6-1 Experimental feed drive.

Figure 6-1 shows the experimental setup built for this study. The design and analysis of this setup are reported in Appendix A. It is a linear feed drive (Y-axis) connected with a trunnion unit (A- and C-axis) by an I-shaped flexible structure. Such configuration induces a 35 Hz flexible bending mode with a 19 Hz anti-resonance. These values are similar to the characteristics of a medium- to large-sized industrial machine tool.

This setup replicates the machine configuration of Case 2 discussed in Section 5.3.2 where significant flexibility exists between the linear drive and the rotary drive. Since the C-axis is a symmetrically cylindrical rotor which can be viewed as an independent dynamic system, therefore, the dynamic model in this case study considers only the coupled linear Y- and tilting A-axes. On the other hand, since the IMU is mounted on the table (C-axis), the kinematic model built in this case study includes the Y-A-C axes, in order to demonstrate successful vibration reconstruction even during Y-A-C axes simultaneous motion.

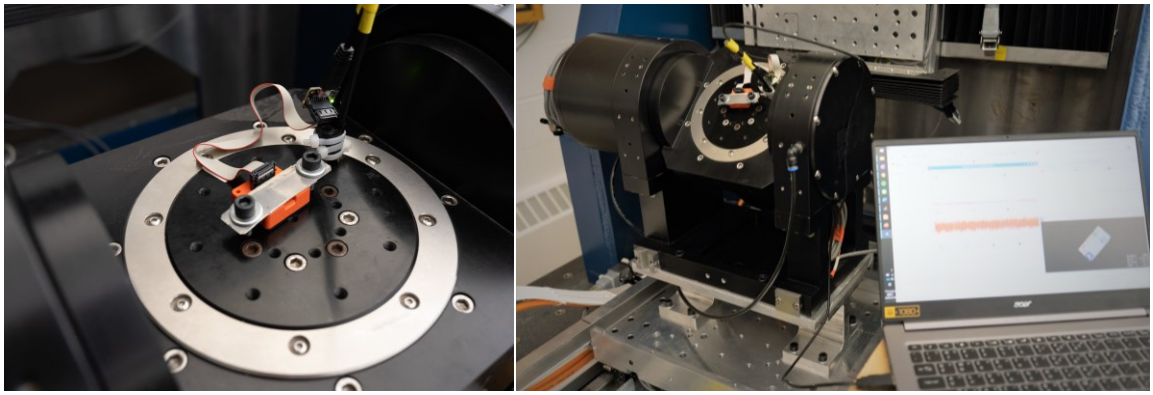

Figure 6-2 Installation of an IMU.

As shown in Figure 6-2, a Xsens MTi-630 IMU is firmly attached to the machine table. The IMU data is transferred via an USB cable to a laptop. While the feed drive is operating, both the servo data and IMU data are collected. The following items are the reasons for using an IMU for this application:

(1) *No kinematic constraint*: position measurement instruments, for example, a grid encoder (KGM) or laser vibrometer, can only measure within limited travelling range along a specific direction. Measuring 3D simultaneous motion is not possible. In contrast, tri-axial accelerometers are non-intrusive, easy to be attached/installed, and are without kinematic constraints.

(2) *Reliable static response*: AC accelerometers inherently behave as high-pass filter which are not suitable for measuring feed drive motion which primarily lies in low frequency region. In contrast,

DC accelerometers, for example, MEMS IMUs, have stable static (0 Hz) response, which is ideal for this application.

(3) *6-DOF measurement*: with the integration of a tri-axial accelerometer and a tri-axial gyroscope, an IMU can measure both the orientation and translational acceleration, fully capturing the motion of multi-axis feed drives.

(4) *Future potential:* IMUs made by MEMS technology are relatively inexpensive, and its performance has been improving over the past decade [93]. It is therefore foreseeable that high-accuracy and cost-effective MEMS IMUs can be realized in the coming future. Hence, it is time to explore its application to precision control engineering.

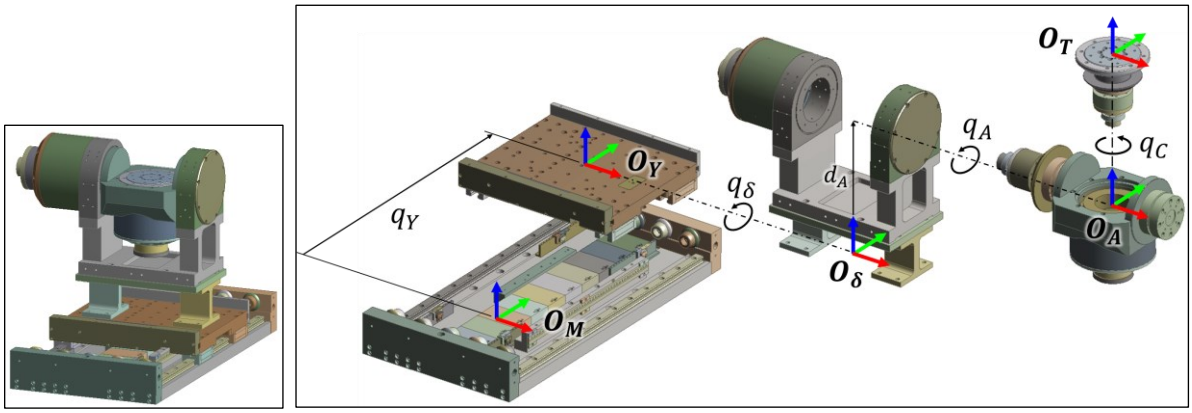

Figure 6-3 The kinematics of the experimental drive assembly.

The machine kinematics can be represented by Figure 6-3. $\boldsymbol{O}_M$ is the fixed machine inertial frame. $\boldsymbol{O}_Y$, $\boldsymbol{O}_\delta$, $\boldsymbol{O}_A$, and $\boldsymbol{O}_T$ are the local moving frames attached to the linear table, the flexible machine frame, the tilting rotary feed drive, and the rotary table, respectively. The displacement of each feed drive is defined as q_Y, q_A, and q_C, which can be directly measured by the axis encoders. The I-shaped flexible structure is modeled by a torsional spring-damper of which q_δ is the deflection angle.

Machine Kinematics

The machine kinematics from $\boldsymbol{O}_M$ to $\boldsymbol{O}_T$ can be described by a 4×4 transformation matrix $\boldsymbol{H}_{T/M}$:

$$\boldsymbol{H}_{T/M} = \begin{bmatrix} \boldsymbol{R}_{T/M} & \boldsymbol{T}_{T/M} \\ \boldsymbol{0}_{1\times3} & 1 \end{bmatrix} \tag{6.1}$$

$\boldsymbol{R}_{T/M}$ is a 3×3 rotation matrix, and $\boldsymbol{T}_{T/M}$ is a 3×1 translational vector.

Following the machine kinematic chain, the transformation matrix $\boldsymbol{H}_{T/M}$ can be derived as:

$$\boldsymbol{H}_{T/M} = \boldsymbol{H}_{T/A}\boldsymbol{H}_{A/\delta}\boldsymbol{H}_{\delta/Y}\boldsymbol{H}_{Y/M} \tag{6.2}$$

The corresponding rotation matrices are $\boldsymbol{R}_{T/A} = \begin{bmatrix} cos\, q_C & sinq_C & 0 \\ -sinq_C & cos\, q_C & 0 \\ 0 & 0 & 1 \end{bmatrix}$, $\boldsymbol{R}_{A/\delta} = \begin{bmatrix} 1 & 0 & 0 \\ 0 & cos\, q_A & sinq_A \\ 0 & -sinq_A & cosq_A \end{bmatrix}$, $\boldsymbol{R}_{\delta/Y} = \begin{bmatrix} 1 & 0 & 0 \\ 0 & cos\, q_\delta & sinq_\delta \\ 0 & -sinq_\delta & cosq_\delta \end{bmatrix}$, and $\boldsymbol{R}_{Y/M} = \begin{bmatrix} 1 & 0 & 0 \\ 0 & 1 & 0 \\ 0 & 0 & 1 \end{bmatrix}$ respectively.

As translational vectors $\boldsymbol{T}$ are not necessary for the reconstruction of the machine vibration, $\boldsymbol{T}$ are not illustrated in this section.

If only considering the rigid body kinematics, i.e., q_δ is neglected, then the transformation matrix $\boldsymbol{H}_{T/M}$ becomes:

$$\boldsymbol{H}_{T/M} = \boldsymbol{H}_{T/A}\boldsymbol{H}_{A/Y}\boldsymbol{H}_{Y/M} \tag{6.3}$$

$\boldsymbol{O}_\delta$ is neglected and $\boldsymbol{R}_{A/Y} = \begin{bmatrix} 1 & 0 & 0 \\ 0 & cos\, q_A & sinq_A \\ 0 & -sinq_A & cosq_A \end{bmatrix}$. In the following sections, the above kinematic models covered from Eq. (6.1) to Eq. (6.3) have been applied to reconstruct the machine vibration with the collected data.

6.3 Measuring the Orientation by IMUs

The raw measurement data from an IMU are the linear acceleration (containing gravity) and angular velocity expressed in the sensor frame. Then, the sensor orientation, gravity-free linear acceleration, and angular velocity expressed in the global frame can be estimated by strapdown integration and sensor fusion. This section details these computation processes.

6.3.1 Predicting Orientation by Strapdown Integration

Definition of the Global Frame

When an IMU starts operating, it establishes a fixed inertial global frame $\boldsymbol{O}_G$ as a reference for expressing the orientation of the sensor frame $\boldsymbol{O}_S$ attached to the IMU (see Figure 6-4.) Since the gravity direction can be indicated by the triaxial accelerometer, the vertical axis of $\boldsymbol{O}_G$ is defined to be parallel to the gravity direction, and the other two unreferenced horizontal axes of $\boldsymbol{O}_G$ are aligned with

the sensor frame $\boldsymbol{O_S}$ at the beginning of the measurement. In other words, $\boldsymbol{O_G}$ is dependent on the initial sensor orientation.

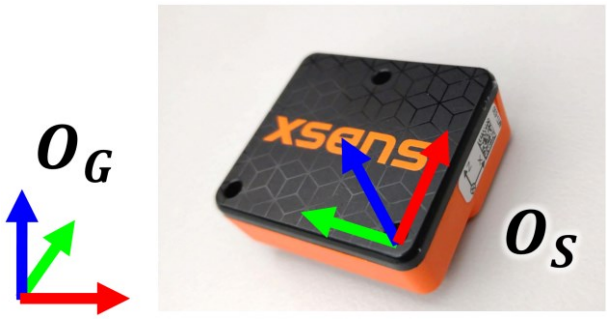

Figure 6-4 Global frame $\boldsymbol{O_G}$ and sensor frame $\boldsymbol{O_S}$ defined by an IMU.

Orientation Expression

The orientation of frame $\boldsymbol{O_S}$ with respect to frame $\boldsymbol{O_G}$ can be expressed by a 3×3 rotation matrix $\boldsymbol{R_{S/G}}$, which is also called direction cosine matrix (DCM). More details about orientation expression can be found in [107]. An arbitrary position u in space can be represented by vectors $\boldsymbol{u^G}$ and $\boldsymbol{u^S}$ with respect to $\boldsymbol{O_G}$ and $\boldsymbol{O_S}$ respectively. The vectors can be converted by $\boldsymbol{R_{S/G}}$ as:

$$\boldsymbol{u^S} = \boldsymbol{R_{S/G}}\boldsymbol{u^G} \tag{6.4}$$

Strapdown Integration

The orientation $\boldsymbol{R_{S/G}}$ cannot be directly measured. Instead, the triaxial gyroscope measures the angular velocity of the sensor, $\boldsymbol{\omega_{S/G}^S} = [\omega_x \quad w_y \quad w_z]^T$, with respect to the global frame (as the subscript S/G) and expressed in the sensor frame (as the superscript S). $\dot{\boldsymbol{R}}_{S/G}$ can be computed by $\boldsymbol{\omega_{S/G}^S}$ as:

$$\dot{\boldsymbol{R}}_{S/G} = -\boldsymbol{\Omega}\boldsymbol{R}_{S/G} \tag{6.5}$$

and

$$\boldsymbol{\Omega} = \begin{bmatrix} 0 & -\omega_z & \omega_y \\ \omega_z & 0 & -\omega_x \\ -\omega_y & \omega_x & 0 \end{bmatrix} \tag{6.6}$$

$\boldsymbol{\Omega}$ is the skew-symmetric matrix for rate angle $\boldsymbol{\omega_{S/G}^S}$. The complete derivation of Eq. (6.5) and (6.6) can be found in [94]. We can notice that Eq. (6.5) is essentially nine scalar *1*st-order differential equations.

Since gyroscopes provide discretized data at a fixed sampling period t_s, the predicted DCM at the $(k+1)$th time step is:

$$\boldsymbol{R}_{S/G_{k+1}} = \boldsymbol{R}_{S/G_k} + \dot{\boldsymbol{R}}_{S/G_k} t_s \tag{6.7}$$

By plugging in Eq. (6.5) and Eq. (6.6), then $\boldsymbol{R}_{S/G_{k+1}}$ becomes

$$\boldsymbol{R}_{S/G_{k+1}} = (\boldsymbol{I}_3 - \boldsymbol{\Omega}_k t_s)\boldsymbol{R}_{S/G_k} \tag{6.8}$$

$\boldsymbol{\Omega}_k$ is built by the kth sampled angular velocity. Eq. (6.8) is strapdown integration indicating that the orientation in the next time step is a function of the orientation and angular velocity at the current time step.

6.3.2 Sensor Fusion

Sensor Model

As discussed in the introduction in Section 2.6.2, the output of a triaxial gyroscope

$$\boldsymbol{y}_G = \boldsymbol{\omega}^S_{S/G} + \boldsymbol{v}_G + \boldsymbol{b}_G \tag{6.9}$$

is the sum of the true angular velocity $\boldsymbol{\omega}^S_{S/G}$, the noise $\boldsymbol{v}_G$, and the bias $\boldsymbol{b}_G$ [96]. If using an IMU just for a short period of time, for example, the experiment in Section 6.5 where the total duration is 6.12 seconds, $\boldsymbol{b}_G$ can be assumed constant, and therefore can be calibrated when the sensor is at rest. However, gyroscope noise $\boldsymbol{v}_G$ will lead to angle random walk (ARW) behavior while performing strapdown integration.

On the other hand, the output of a triaxial accelerometer

$$\boldsymbol{y}_A = \boldsymbol{a}^S_{S/G} + \boldsymbol{g}^S_{S/G} + \boldsymbol{v}_A + \boldsymbol{b}_A \tag{6.10}$$

is the sum of the true sensor linear acceleration $\boldsymbol{a}^S_{S/G}$, the gravity $\boldsymbol{g}^S_{S/G}$, the noise $\boldsymbol{v}_A$, and the bias $\boldsymbol{b}_A$ [96]. When $\boldsymbol{a}^S_{S/G}$ is small enough to be negligible, the orientation predicted by gyroscope measurement can be corrected by fusing it with the accelerometer output since $\boldsymbol{g}^S_{S/G}$ also indicates the inclination, i.e., the orientation except the rotation around the vertical (gravity) axis.

Sensor Fusion Algorithm

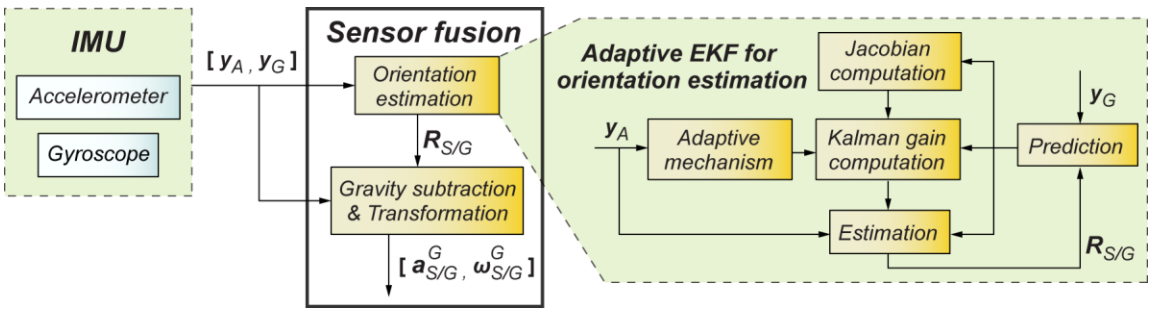

Figure 6-5 Sensor fusion algorithm adopted from [102].

As the review presented in Section 2.6.3, various sensor fusion algorithms for orientation estimation have been developed. The differences between those algorithms are primarily the required computational costs and dynamic bias estimation. As the application in this thesis is off-line and short, such differences are rather minor. However, since the experimental trajectory is complex multi-axis simultaneous motion, rejecting the sensor acceleration from the gravity is more critical to this application. Therefore, an adaptive extended Kalman filter (EKF) [102] is adopted in this research (see Figure 6-5.) Jacobian computation is performed due to the nonlinear nature of the orientation. The estimated orientation $\boldsymbol{R}_{S/G}$ is then used to convert the measured angular velocity and linear acceleration in the sensor frame into the global frame, $\boldsymbol{\omega}^G_{S/G}$ and $\boldsymbol{a}^G_{S/G}$. Since there is no way to distinguish the sensor acceleration $\boldsymbol{a}^S_{S/G}$ from the gravity $\boldsymbol{g}^S_{S/G}$ within the accelerometer outputs $\boldsymbol{y}_A$, the orientation estimation adopts an adaptive scheme to reject the impact of sensor acceleration $\boldsymbol{a}^S_{S/G}$ such that the estimation with accelerometer measurement is enabled only when the magnitude of $\boldsymbol{a}^S_{S/G}$ is negligible, i.e., $|\boldsymbol{y}_A| \cong 9.8\, m/s^2$. This step unfortunately makes the estimation solely rely on the gyroscope measurement when the sensor is in motion.

As a side note, although most commercial IMUs have been equipped with embedded sensor fusion algorithms, the details are normally kept confidential. Due to not knowing how their body acceleration rejection scheme works, the above known sensor fusion algorithm is applied to process the raw data instead.

Averaging vs. the Standard Deviation

If simply numerically integrating gyroscope data to obtain the angle without the correction by accelerometer measurement, then after time t, the gyroscope noise v_G may lead to angle random walk (ARW) behavior. The standard deviation of the drift is

$$\sigma_{arw} = \sigma_G \sqrt{t_s t} \tag{6.11}$$

t_s is the sampling period, and σ_G is the standard deviation of the gyroscope noise.

To mitigate the above negative impact, it is possible to reduce the standard deviation of the gyroscope noise by taking the average of n repeating measurements. The standard deviation of the averaged data $\sigma_{G_{avg}}$ becomes $1/\sqrt{n}$ times of that of a single measurement, i.e., $\sigma_{G_{avg}} = \sigma_G/\sqrt{n}$.

To improve the root mean square (RMS) error due to the noise, the tests in this research have taken the average of the 22 repeating measurements to reduce the signal noise variance.

6.3.3 Summary

Overall, the data that can be accessed from the IMU and the sensor fusion algorithm are listed in Table 6-1. In the next section, the data will be used to reconstruct machine local vibration.

Table 6-1 A summary of available data from the IMU and the sensor fusion algorithm.

$\boldsymbol{y}_A$	Accelerometer output
$\boldsymbol{y}_G$	Gyroscope output
$\boldsymbol{R}_{S/G}$	DCM. Orientation of the sensor with respect to the global frame
$\boldsymbol{\omega}_{S/G}^{G}$	Angular velocity of the sensor with respect to the global frame, expressed in the global frame
$\boldsymbol{a}_{S/G}^{G}$	Gravity-free linear acceleration of the sensor with respect to the global frame, expressed in the global frame

6.4 Data Mapping between CNC Data and IMU Data

Before utilizing the CNC servo data and IMU data, they first have to be synchronized since they are collected by separated data acquisition systems. Section 6.4.1 presents a strategy to synchronize these two sources of data.

Next, as described in the introduction in Section 6.3, the IMU provides the sensor motion expressed in its own global frame $\boldsymbol{O}_G$. However, the goal is to capture the structural vibration q_δ expressed in machine local frame $\boldsymbol{O}_\delta$ as shown in the machine kinematic diagram, Figure 6-3. Therefore, there is a

need to transform the IMU data into the local frame. The proposed methodology for this purpose is illustrated in Section 6.4.2.

6.4.1 Data Synchronization

Since most of the commercial CNCs do not allow customized real-time data acquisition, the IMU measurement has to be taken by a separated data acquisition system. Therefore, there is a need to synchronize the data from the different acquisition systems.

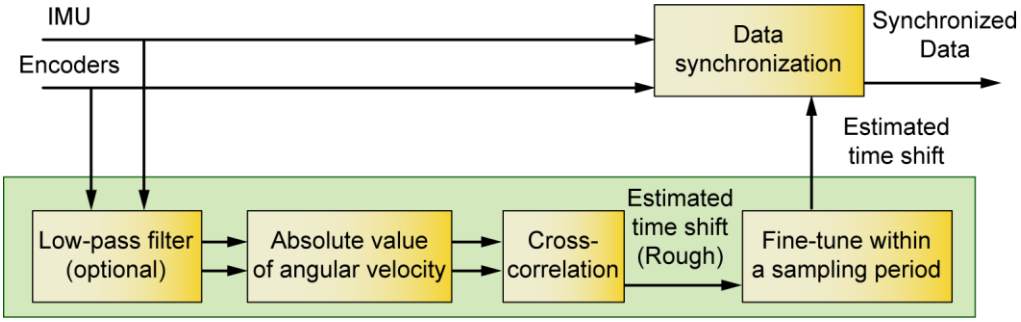

Figure 6-6 Data synchronization flowchart.

Cross-correlation is used to synchronize the data. It is one of the most common synchronization approaches and has been used in various fields of science and engineering [121]. The proposed approach assumes that the rigid body motion is the dominant behavior exhibited in both the IMU and encoder data. The main discrepancy is the transient relative vibration between the two measurement locations. The vibration is assumed negligible, or it could be optionally removed by low-pass filters.

The flowchart is shown in Figure 6-6. The absolute magnitude of angular velocity is chosen as the fitting variable to synchronize the two datasets. The magnitude of angular velocity measured by the IMU, $\left|\boldsymbol{\omega}_{S/G}^{S}\right|$, should be equal to the magnitude of angular velocities measured by the rotary encoders. Considering the machine kinematic diagram in Figure 6-3, the magnitude of angular velocity is $\sqrt{\dot{q_A}^2 + \dot{q_C}^2}$.

Then, the synchronization time shift is estimated by the following two steps. First, a rough estimation is done by performing discrete cross-correlation of the two angular velocity magnitudes. The index with the highest correlation indicates the estimated time shift.

However, the resolution of the time shift estimation is confined to the length of sampling period of the data acquisition. For example, the sampling period of Xsens MTi-630 is 2.5 [ms]. This may lead to

erroneous estimation of phase response of a closed-loop control system. This problem can be mitigated by fine-tuning the time shift with the following procedures.

(1) Up-sample the two datasets by spline fitting to reduce the length of discrete time interval.
(2) The estimated time shift is refined by performing the cross-correlation only over a unit sampling period.
(3) Down-sample the datasets to the original sampling period.

After finding the estimated time shift, this is used to shift the IMU data and CNC data so that they are synchronized.

6.4.2 Reconstruction of the Local Vibration Using an IMU

An IMU records the motion of the sensor frame $\boldsymbol{O}_S$ with respect to the global frame $\boldsymbol{O}_G$ while our interest is the structural vibration defined in local frames, i.e., q_δ in $\boldsymbol{O}_\delta$ shown in Figure 6-3. This section presents a methodology to reconstruct such local vibration used for flexible joint model identification.

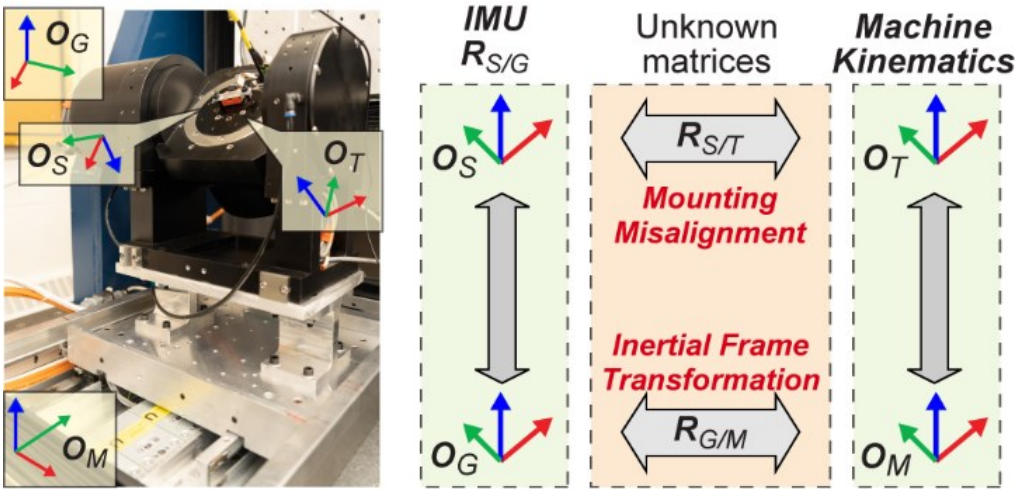

Figure 6-7 Coordinate frames of the machine and the IMU.

When an IMU is attached to the machine table, the relevant coordinates frames are shown in Figure 6-7. There are two kinematic chains from $\boldsymbol{O}_M$ to $\boldsymbol{O}_T$. One chain is via the machine kinematics, which has been illustrated in Section 6.2. The variables of the rigid body kinematics, $[q_Y, q_A, q_C]$, can be measured by the machine encoders. The local structural vibration q_δ is the unknown variable.

The other chain is via the IMU measurements from the global inertial frame $\boldsymbol{O}_G$ to the sensor frame $\boldsymbol{O}_S$, which is rigidly attached to the table frame $\boldsymbol{O}_T$. To relate the IMU and the machine kinematics, there are two unknown rotation matrices, $\boldsymbol{R}_{G/M}$ and $\boldsymbol{R}_{S/T}$ which must be solved.

$\boldsymbol{R}_{G/M}$ is the inertial frame transformation representing the orientation between $\boldsymbol{O}_G$ and $\boldsymbol{O}_M$. These two inertial frames are not identical because $\boldsymbol{O}_G$ is defined depending on the initial sensor orientation. On the other hand, $\boldsymbol{R}_{S/T}$ is the mounting misalignment of the IMU with respect to the table frame.

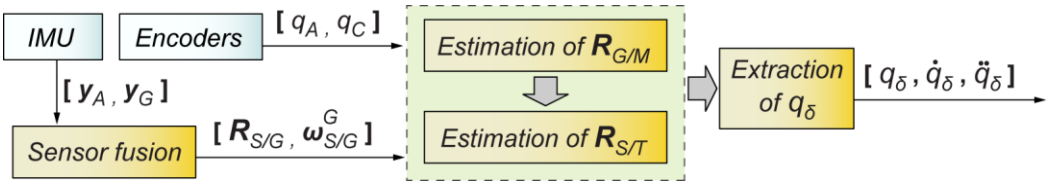

Figure 6-8 The flowchart of estimating structural vibration q_δ.

Following the flowchart in Figure 6-8, the following sections present the methods for estimating $\boldsymbol{R}_{G/M}$ and $\boldsymbol{R}_{S/T}$ by utilizing the collected data from the machine encoders and the IMU. Once $\boldsymbol{R}_{G/M}$ and $\boldsymbol{R}_{S/T}$ are estimated, the local structural vibration q_δ can be reconstructed.

Estimation of Inertial Frame Transformation $R_{G/M}$

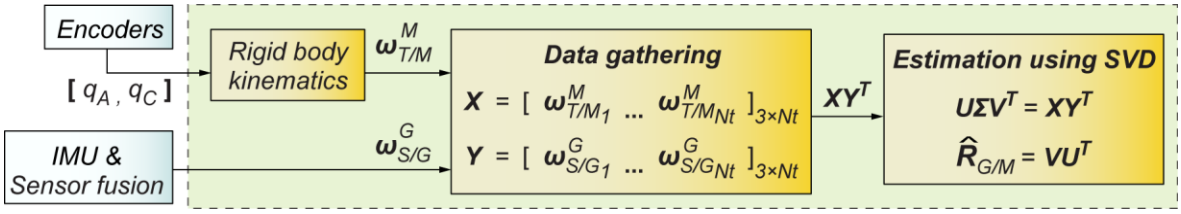

Figure 6-9 Estimation of $R_{G/M}$.

Figure 6-9 shows the flowchart for estimating $\boldsymbol{R}_{G/M}$. Considering the machine rigid body kinematics in Section 6.2, the angular velocity of the table frame $\boldsymbol{O}_T$ expressed in the machine inertial frame $\boldsymbol{O}_M$ can be derived as:

$$\boldsymbol{\omega}^M_{T/M} = \begin{bmatrix} \dot{q}_A \\ 0 \\ 0 \end{bmatrix} + \left(\boldsymbol{R}_{A/Y}\boldsymbol{R}_{Y/M}\right)^T \begin{bmatrix} 0 \\ 0 \\ \dot{q}_C \end{bmatrix} = \begin{bmatrix} \dot{q}_A \\ 0 \\ 0 \end{bmatrix} + \begin{bmatrix} 1 & 0 & 0 \\ 0 & cos\, q_A & -sinq_A \\ 0 & sinq_A & cosq_A \end{bmatrix} \begin{bmatrix} 0 \\ 0 \\ \dot{q}_C \end{bmatrix} \tag{6.12}$$

Computing $\boldsymbol{\omega}^M_{T/M}$ via Eq. (6.12) requires $[q_A, q_C, \dot{q}_A, \dot{q}_C]$, which are available data from the encoders of the rotary A and C axes. Since the IMU is rigidly attached to the rotary table, the angular velocities of $\boldsymbol{O}_S$ and $\boldsymbol{O}_T$ with respect to an arbitrary inertial frame, for example $\boldsymbol{O}_M$, should be identical, i.e.,

$$\boldsymbol{\omega}_{T/M}^{M} = \boldsymbol{\omega}_{S/M}^{M} \tag{6.13}$$

On the other hand, the estimated $\boldsymbol{\omega}_{S/G}^{G}$ remains the same if changing the referenced inertial frame, i.e.,

$$\boldsymbol{\omega}_{S/G}^{G} = \boldsymbol{\omega}_{S/M}^{G} \tag{6.14}$$

Combining Eq. (6.13) and Eq. (6.14) and introducing $\boldsymbol{R}_{G/M}$, the following equation is derived as:

$$\boldsymbol{\omega}_{S/G}^{G} = \boldsymbol{\omega}_{S/M}^{G} = \boldsymbol{R}_{G/M}\boldsymbol{\omega}_{S/M}^{M} = \boldsymbol{R}_{G/M}\boldsymbol{\omega}_{T/M}^{M} \tag{6.15}$$

By gathering N_t samples of data from the encoders and the IMU, the following $\boldsymbol{X}$ and $\boldsymbol{Y}$ data matrices can be built.

$$\begin{cases} \boldsymbol{X} = \left[\boldsymbol{\omega}_{T/M}^{M}{}_{1} \quad \cdots \quad \boldsymbol{\omega}_{T/M}^{M}{}_{k} \quad \cdots \quad \boldsymbol{\omega}_{T/M}^{M}{}_{N_t}\right]_{3\times N_t} \\ \boldsymbol{Y} = \left[\boldsymbol{\omega}_{S/G}^{G}{}_{1} \quad \cdots \quad \boldsymbol{\omega}_{S/G}^{G}{}_{k} \quad \cdots \quad \boldsymbol{\omega}_{S/G}^{G}{}_{N_t}\right]_{3\times N_t} \end{cases} \tag{6.16}$$

$\boldsymbol{X}$ is built by the encoder data while $\boldsymbol{Y}$ is built by the IMU data. According to Eq. (6.15), the estimation of the rotation matrix $\boldsymbol{R}_{G/M}$ can be formulated as the following optimization problem:

$$\underset{\boldsymbol{R}_{G/M}\in SO(3)}{\text{Min}} \sum_{k=1}^{N_t} \left\| \boldsymbol{\omega}_{S/G}^{G}{}_{k} - \left(\boldsymbol{R}_{G/M}\boldsymbol{\omega}_{T/M}^{M}{}_{k}\right)\right\|^2 \tag{6.17}$$

This can be solved in a least squares sense [122] by taking the singular value decomposition (SVD) of $\boldsymbol{XY^T}$,

$$\boldsymbol{U\Sigma V^T} = \boldsymbol{XY^T} \tag{6.18}$$

Then, the rotation matrix $\boldsymbol{R}_{G/M}$ can be estimated by

$$\widehat{\boldsymbol{R}}_{G/M} = \left(\boldsymbol{UV^T}\right)^{\boldsymbol{T}} = \boldsymbol{VU^T} \tag{6.19}$$

Estimation of Mounting Misalignment $\boldsymbol{R_{S/T}}$

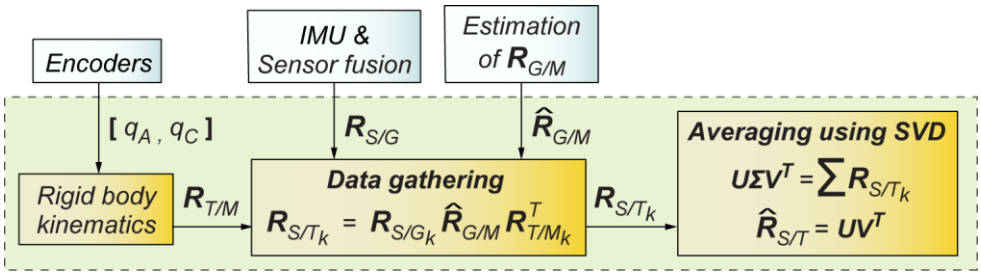

Figure 6-10 The flowchart for estimating $\boldsymbol{R_{S/T}}$.

Figure 6-10 shows the flowchart for estimating $\boldsymbol{R_{S/T}}$. Considering the machine rigid body kinematics demonstrated in Section 6.2, the orientation of the table $\boldsymbol{O_T}$ with respect to machine inertial frame $\boldsymbol{O_M}$ can be derived from Eq. (6.3) as

$$\boldsymbol{R_{T/M}} = \boldsymbol{R_{T/A}R_{A/Y}R_{Y/M}} = \begin{bmatrix} cos\, q_C & sinq_C & 0 \\ -sinq_C & cos\, q_C & 0 \\ 0 & 0 & 1 \end{bmatrix}\begin{bmatrix} 1 & 0 & 0 \\ 0 & cos\, q_A & sinq_A \\ 0 & -sinq_A & cosq_A \end{bmatrix}\begin{bmatrix} 1 & 0 & 0 \\ 0 & 1 & 0 \\ 0 & 0 & 1 \end{bmatrix} \tag{6.20}$$

On the other hand, by incorporating $\boldsymbol{R_{S/G}}$ from the IMU and $\boldsymbol{\hat{R}_{G/M}}$ estimated by Eq. (6.19), $\boldsymbol{R_{T/M}}$ can be derived as

$$\boldsymbol{R_{T/M}} = \boldsymbol{R_{T/S}R_{S/G}\hat{R}_{G/M}} \tag{6.21}$$

Combining Eq. (6.20) and Eq. (6.21), the unknown $\boldsymbol{R_{S/T}}$ can be expressed as

$$\boldsymbol{R_{S/T}} = \boldsymbol{R_{S/G}\hat{R}_{G/M}R^T_{T/M}} \tag{6.22}$$

Since $\boldsymbol{R_{S/G}}$ and $\boldsymbol{R_{T/M}}$ are given, and $\boldsymbol{\hat{R}_{G/M}}$ has been estimated by Eq. (6.19), $\boldsymbol{R_{S/T}}$ can then be estimated. By gathering N_t samples of data from the IMU and the encoders, $\boldsymbol{R_{S/T_k}}$ for the *kth* sample can be computed as

$$\boldsymbol{R_{S/T_k}} = \boldsymbol{R_{S/G_k}\hat{R}_{G/M}R_{Y/A_k}R_{A/T_k}} \tag{6.23}$$

Taking the SVD of the sum of $\boldsymbol{R_{S/T_k}}$,

$$\boldsymbol{U\Sigma V^T} = \sum_{k=1}^{N_t} \boldsymbol{R_{S/T_k}} \tag{6.24}$$

then $\boldsymbol{R_{S/T}}$ can be estimated by normalizing the above summation as

$$\widehat{\boldsymbol{R}}_{S/T} = \boldsymbol{U}\boldsymbol{V}^{\boldsymbol{T}} \tag{6.25}$$

This approach is taking the average of the estimation from each sample.

Extraction of Structural Vibration q_δ

Now, introducing the structural vibration $\boldsymbol{R}_{\delta/Y}$ into Eq. (6.20), $\boldsymbol{R}_{T/M}$ becomes

$$\begin{aligned}\boldsymbol{R}_{T/M} &= \boldsymbol{R}_{T/A}\boldsymbol{R}_{A/\delta}\boldsymbol{R}_{\delta/Y}\boldsymbol{R}_{Y/M} \\ &= \begin{bmatrix} cos\, q_C & sinq_C & 0 \\ -sinq_C & cos\, q_C & 0 \\ 0 & 0 & 1 \end{bmatrix}\begin{bmatrix} 1 & 0 & 0 \\ 0 & cos\, q_A & sinq_A \\ 0 & -sinq_A & cosq_A \end{bmatrix}\begin{bmatrix} 1 & 0 & 0 \\ 0 & cos\, q_\delta & sinq_\delta \\ 0 & -sinq_\delta & cosq_\delta \end{bmatrix}\begin{bmatrix} 1 & 0 & 0 \\ 0 & 1 & 0 \\ 0 & 0 & 1 \end{bmatrix}\end{aligned} \tag{6.26}$$

Combining Eq. (6.26), Eq. (6.21), and the estimated $\widehat{\boldsymbol{R}}_{S/T}$, $\boldsymbol{R}_{\delta/Y}$ can be reconstructed as

$$\boldsymbol{R}_{\delta/Y} = \boldsymbol{R}_{A/\delta}^{T}\boldsymbol{R}_{T/A}^{T}\widehat{\boldsymbol{R}}_{S/T}^{T}\boldsymbol{R}_{S/G}\widehat{\boldsymbol{R}}_{G/M}\boldsymbol{R}_{Y/M}^{T} \tag{6.27}$$

If representing $\boldsymbol{R}_{\delta/Y}$ by Z-Y-X Euler angles:

$$\begin{aligned}\boldsymbol{R}_{\delta/Y}(q_\delta, q_\theta, q_\psi) &= \boldsymbol{R}_x(q_\delta)\boldsymbol{R}_y(q_\theta)\boldsymbol{R}_z(q_\psi) \\ &= \begin{pmatrix} 1 & 0 & 0 \\ 0 & cos\, q_\delta & sin\, q_\delta \\ 0 & -sin\, q_\delta & cos\, q_\delta \end{pmatrix}\begin{pmatrix} cos\, q_\theta & 0 & -sin\, q_\theta \\ 0 & 1 & 0 \\ sin\, q_\theta & 0 & cos\, q_\theta \end{pmatrix}\begin{pmatrix} cos\, q_\psi & sin\, q_\psi & 0 \\ -sin\, q_\psi & cos\, q_\psi & 0 \\ 0 & 0 & 1 \end{pmatrix}\end{aligned} \tag{6.28}$$

the deflection angles attributed to the connection of the tilt stage to the linear stage, q_δ can be solved (see Figure 6-11).

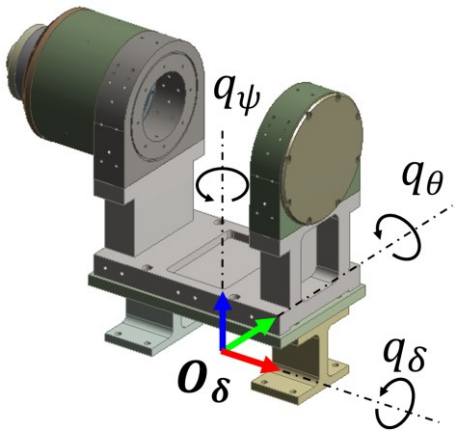

Figure 6-11 Coordinate system representing the structural deflection.

q_θ and q_ψ are rotations along the other two orthogonal directions, which are assumed to be negligible for the I-beam connection, due to the corresponding rotational stiffnesses being much higher. The consideration of simultaneous vibrations in the additional degrees of freedom (i.e., q_θ and q_ψ) is also believed to be possible, but is considered as future research.

6.5 Experimental Validation

A simple command trajectory (Figure 6-12) was designed to test whether the proposed model estimation concept of fusing IMU and CNC signals is able to reconstruct the unknown internal vibration while the Y-A-C axes are moving simultaneously. The trajectory reaches high acceleration and high jerk (see Table 6-2) to excite the structural vibration, such that vibratory inter-axis dynamic coupling effects between the Y- and A- axes can also be observed. The commanded position $\boldsymbol{q_r} = [q_{r_Y}\ q_{r_A}\ q_{r_C}]$, actual position $\boldsymbol{q} = [q_Y\ q_A\ q_C]$, tracking error $\boldsymbol{e} = [e_Y\ e_A\ e_C]$, and motor inputs $\boldsymbol{u} = [u_Y\ u_A\ u_C]$ were collected at a sampling rate of 400 Hz. Time derivative terms $[\dot{\boldsymbol{q}}_r\ \ddot{\boldsymbol{q}}_r\ \dot{\boldsymbol{q}}\ \ddot{\boldsymbol{q}}]$ are also derived.

Table 6-2 Kinematic limits of the experimental trajectory.

	Speed [mm/s] or [°/s]	Acceleration [mm/s^2] or [°/s^2]	Jerk [mm/s^3] or [°/s^3]
Y	2.77E+02	1.38E+03	1.06E+05
A	1.10E+02	1.23E+03	7.67E+04
C	6.76E+01	2.70E+02	2.70E+03

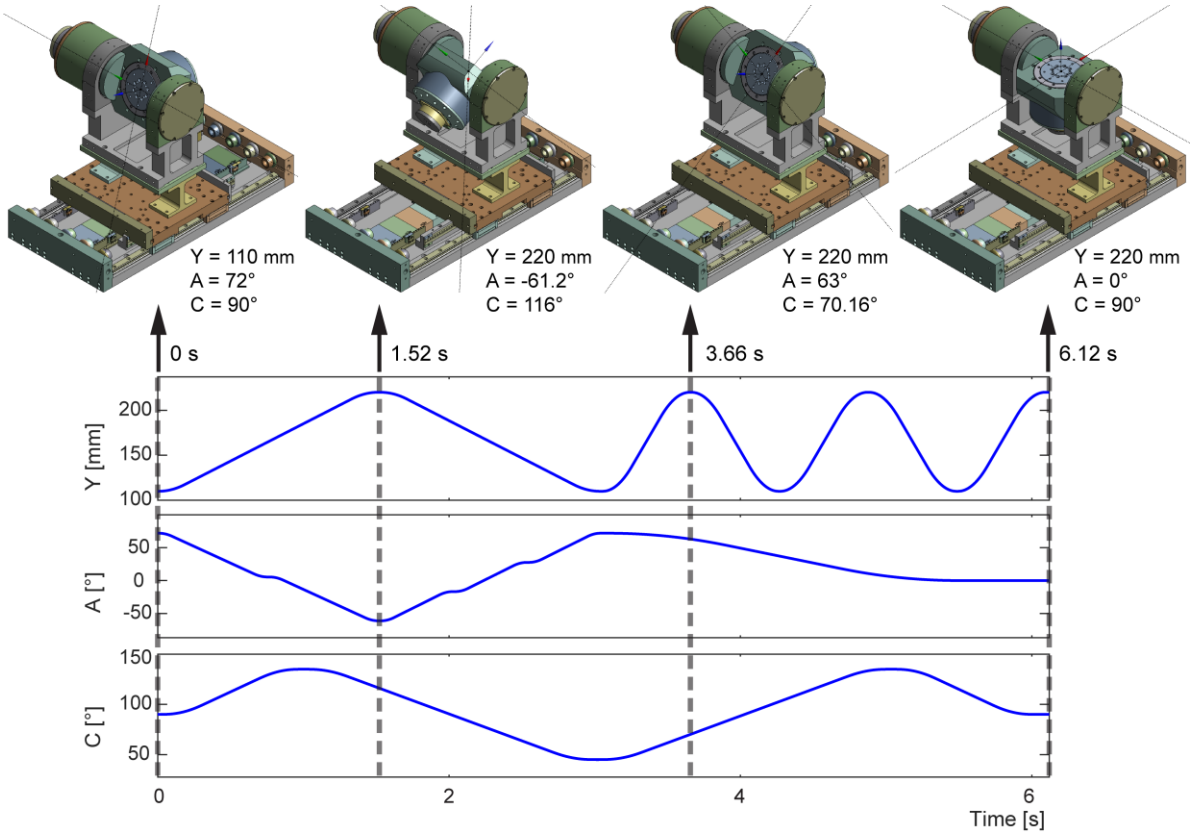

Figure 6-12 Simultaneous motion trajectory.

An Xsens MTi-630 IMU is firmly attached to the rotary table. Table 6-3 lists the signal noise and bias estimated when the sensor was at rest. The sampling rate is 400 Hz. Considering the vibration to be captured is below 50 Hz, a low-pass filter with 100 Hz bandwidth is applied to reduce high-frequency noise. Other critical sensor specifications about the gyro of the Xsens MTi-630 IMU from the product manuals are listed in Table 6-4. It should be noted that the gyro biases have to be recompensated for each of the measurements. Otherwise, significant drifts will occur.

Table 6-3 Estimated signal property of the Xsens MTi-630 IMU.

Sampling rate 400 Hz		X	Y	Z
Gyro	Bias $[°/s]$	1.329E-01	4.537E-02	9.289E-02
	RMS noise $[°/s]$	8.493E-02	7.997E-02	8.274E-02
Accelerometer	RMS noise $[mm/s^2]$	8.165	7.291	5.651

Table 6-4 Critical specifications of the gyro from the product datasheet [99].

Scale Factor variation []	Non-orthogonality [°]	Bias stability $[°/s]$	G-sensitivity $[°/s/G]$

0.5%	5E-02	2E-03	1E-03

In order to reduce the impact of random noise, the experiment was repeated 22 times. Statistically, the RMS noise and ARW of the averaged results become only 21% ($1/\sqrt{22}$) of the original signal properties as listed in Table 6-5. The raw measurement data of the IMU is shown in Figure 6-13. The accelerometer data $\boldsymbol{y}_A$ contain the gravity component overlapping with body acceleration.

Table 6-5 RMS noise reduction by averaging 22 repeated tests.

	X	Y	Z
Gyro $[°/s]$	1.674E-02	1.571E-02	1.617E-02
Accelerometer $[mm/s^2]$	1.741	1.554	1.205

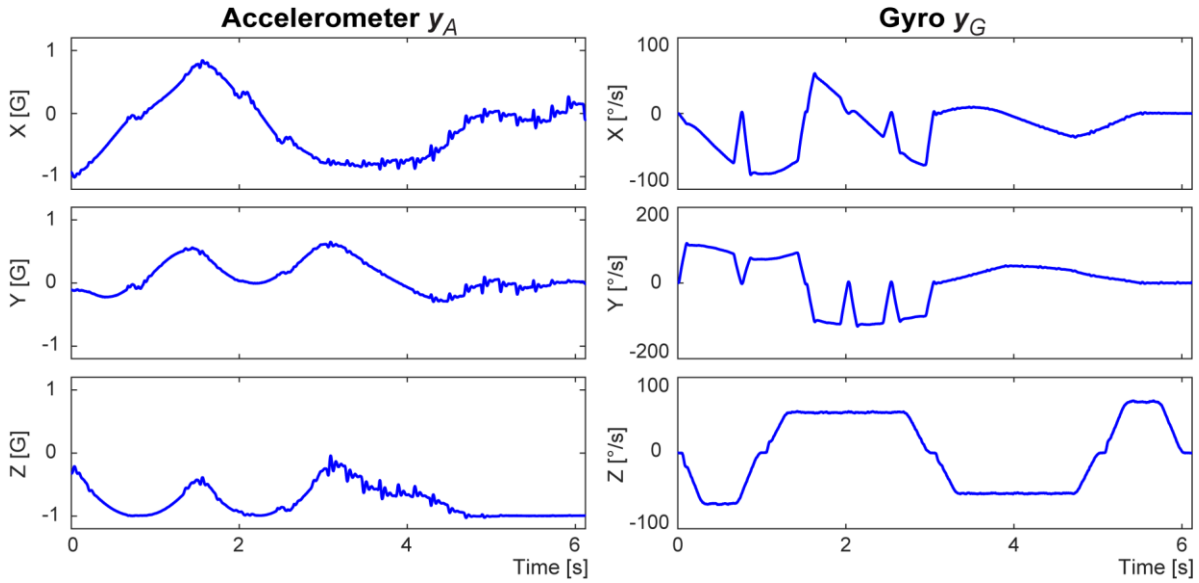

Figure 6-13 Raw measurement from the IMU.

By applying the sensor fusion algorithm introduced in 6.3.2, the raw measurement data is processed as shown in Figure 6-14. Due to the removal of the gravity component, structural vibration can be clearly seen in the linear acceleration data.

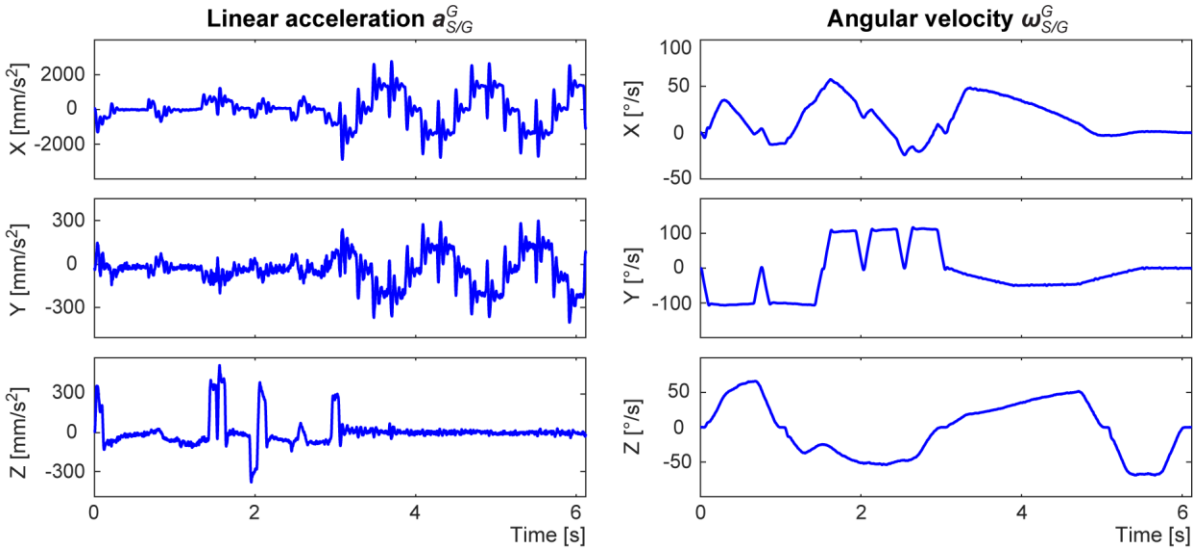

Figure 6-14 Estimation result of sensor fusion expressed in global frame.

Figure 6-15 presents the synchronization of the 22 tests. The absolute value of angular velocity derived from the servo data and IMU data are used for the synchronization (see Section 6.4.1). The residual only exhibits structural vibration and does not appear to show rigid body motion, indicating successful synchronization.

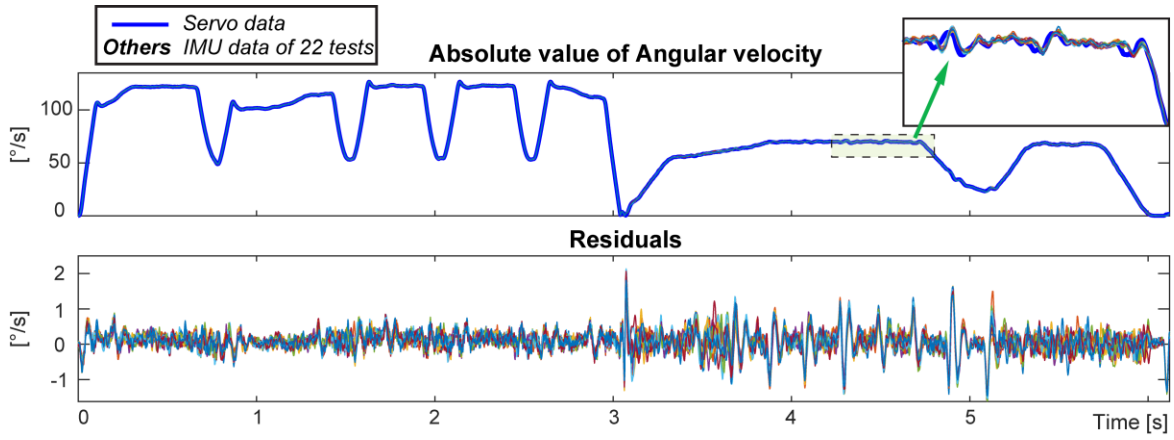

Figure 6-15 Synchronization of 22 tests using the absolute value of angular velocity.

By applying the estimation technique presented in Section 6.4.2, $\boldsymbol{R}_{G/M}$ and $\boldsymbol{R}_{S/T}$ of each of the 22 tests were estimated accordingly (see Figure 6-16). $\boldsymbol{R}_{S/T}$ is more repetitive than $\boldsymbol{R}_{G/M}$ because $\boldsymbol{R}_{S/T}$ represents the mechanical mounting of the sensor on the table. In contrast, $\boldsymbol{R}_{G/M}$ depends on the initial values of the IMU signals which could be affected by time-varying bias and noise.

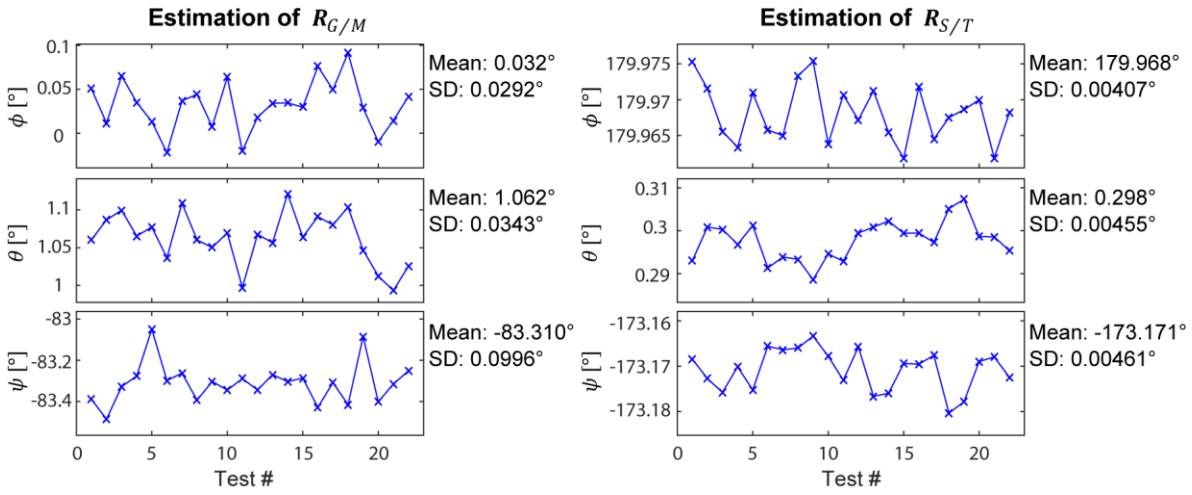

Figure 6-16 Estimation of $R_{G/M}$ and $R_{S/T}$ expressed by $R_x(\phi)R_y(\theta)R_z(\psi)$ Euler angles.

Then, following Eq. (6.27), structural vibration $\mathbf{R}_{\delta/Y}$ can be reconstructed. Euler angles, $\boldsymbol{R}_x(q_\delta)\boldsymbol{R}_y(q_\theta)\boldsymbol{R}_z(q_\psi)$, are used to represent $\boldsymbol{R}_{\delta/Y}$ where q_δ is the principal angle of the structural deflection, and q_ϕ and q_ψ are the rotations along the other two orthogonal directions (see Figure 6-11). The results are shown in Figure 6-17, Figure 6-18, Figure 6-19, and Table 6-6.

q_δ shown in Figure 6-17 exhibits clear vibration excited by the motion of the Y- and A-axis. However, low-frequency perturbations with different patterns are observed in all the three angles.

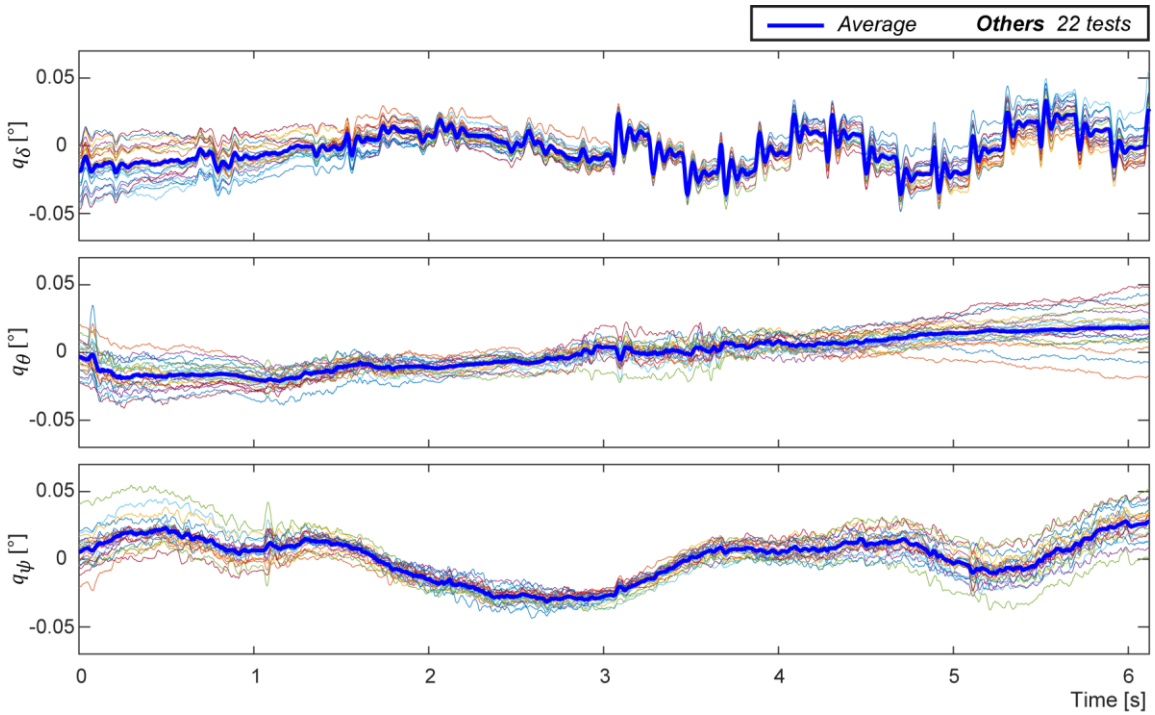

Figure 6-17 Estimation of $R_{\delta/Y}$ converted to Euler angles.

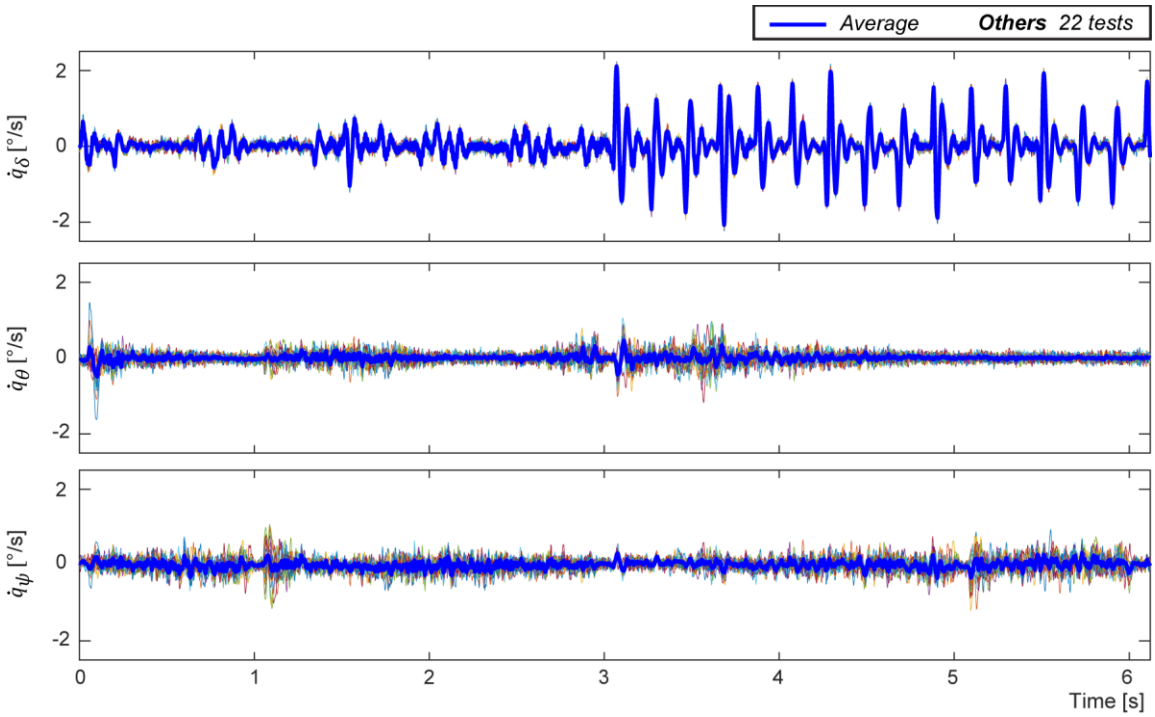

Figure 6-18 Estimated angular velocity $\dot{q}_\phi$, $\dot{q}_\delta$, and $\dot{q}_\psi$.

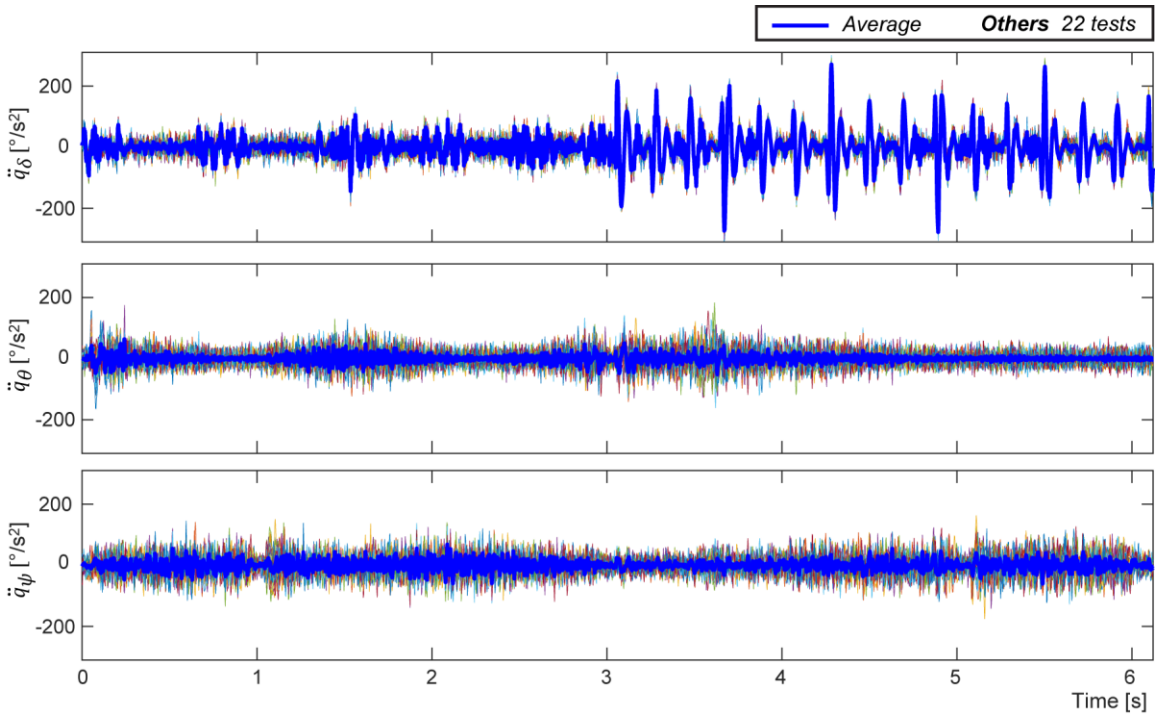

Figure 6-19 Estimated angular acceleration $\ddot{q}_\phi$, $\ddot{q}_\delta$, and $\ddot{q}_\psi$.

Angular velocities and acceleration are plotted in Figure 6-18 and Figure 6-19. Due to taking the time derivatives, structural vibration is much more pronounced in $\dot{q}_\delta$ and $\ddot{q}_\delta$, and low-frequency perturbation becomes insignificant. Non-repetitive noise is diminished by taking the average of the 22 tests.

Table 6-6 Standard deviation of the 22 tests.

$\boldsymbol{R}_{\delta/Y}(q_\delta, q_\theta, q_\psi)$	q_δ (X)	q_θ (Y)	q_ψ (Z)
Angle [˚]	8.150E-03	8.127E-03	8.000E-03
Angular velocity [˚/s]	7.172E-02	1.247E-01	1.497E-01
Angular acceleration [˚/s^2]	1.650E+01	2.354E+01	2.732E+01

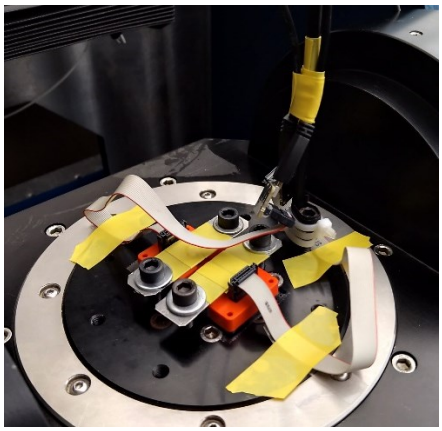

IMU #1: the original one
IMU #2: the new one

Figure 6-20 Two IMUs on machine table.

To further investigate the consistency of the measurement, one more IMU is mounted on the table as shown in Figure 6-20. Complete estimation results of IMU #2 are reported in Appendix B. The averaged results of IMU #1 and IMU #2 are plotted in Figure 6-21, Figure 6-22, and Figure 6-23.

As shown in Figure 6-21 and Figure 6-22, the measurements of angular velocity and acceleration are consistent. The RMS error between the two measurements are 0.0474 ˚/s and 7.3323 ˚/s^2, respectively. Repetitive vibration is observed in $\dot{q}_\delta$ and $\ddot{q}_\delta$, and the velocity and acceleration along the other two orthogonal directions ($\dot{q}_\theta$, $\dot{q}_\psi$, $\ddot{q}_\theta$, and $\ddot{q}_\psi$) are consistently close to zero.

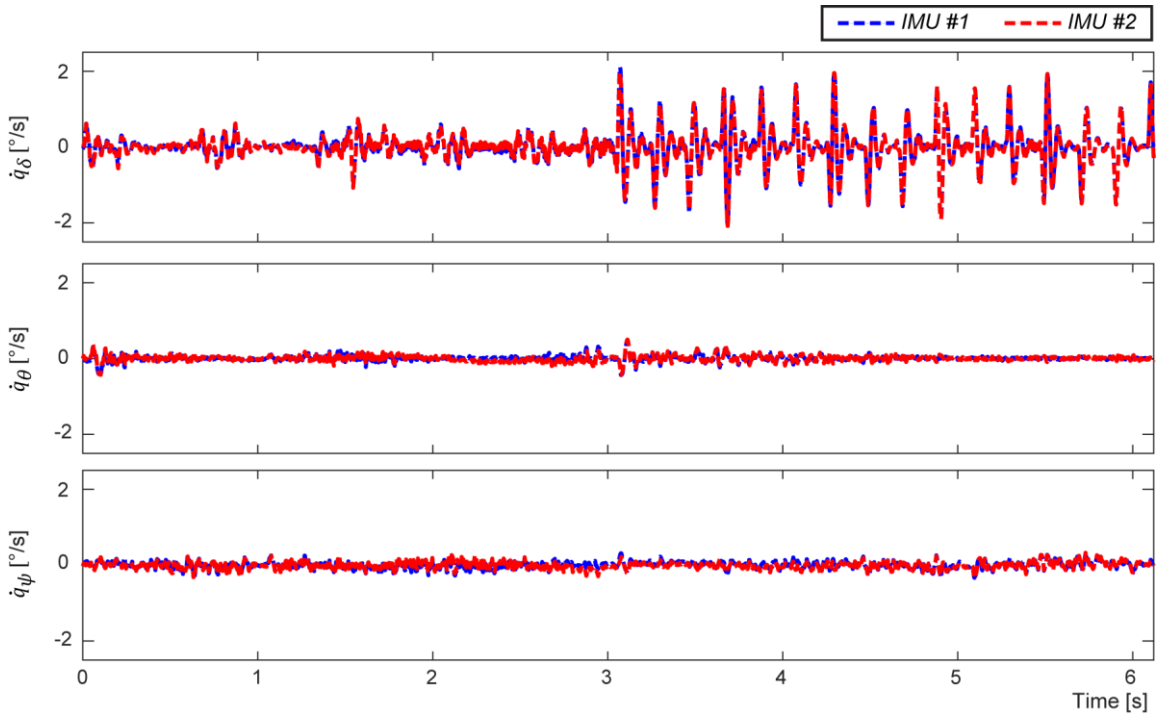

Figure 6-21 Averaged angular velocity of IMU #1 and IMU #2.

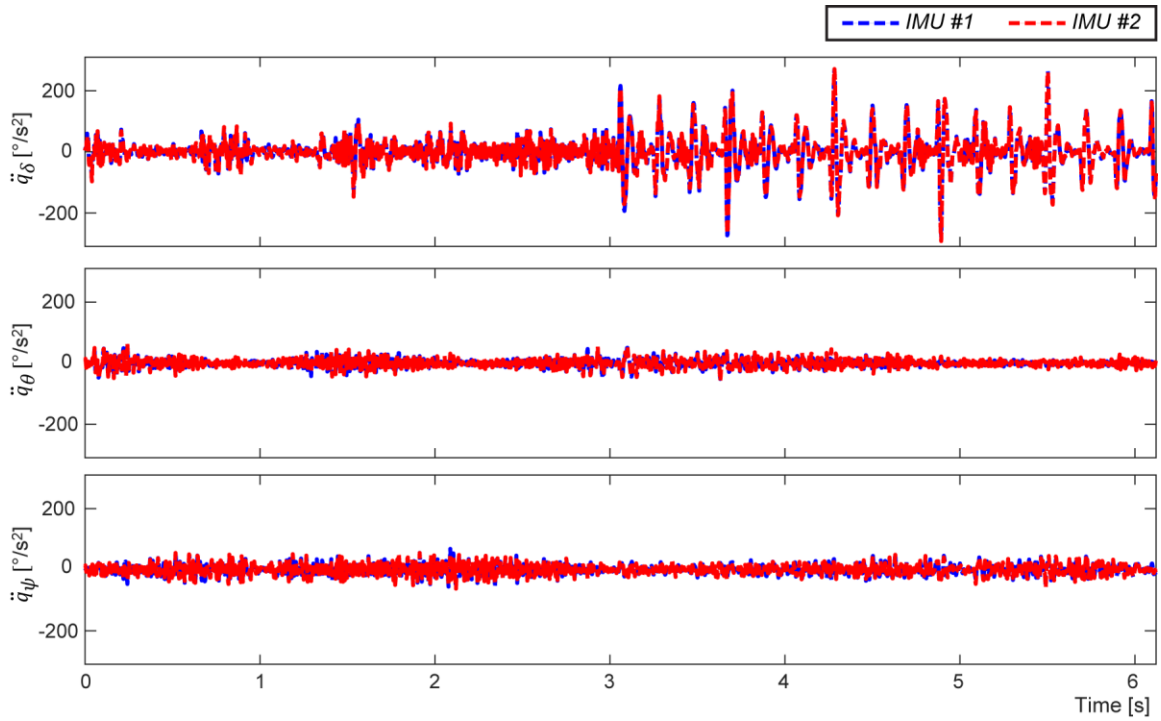

Figure 6-22 Averaged angular acceleration of IMU #1 and IMU #2.

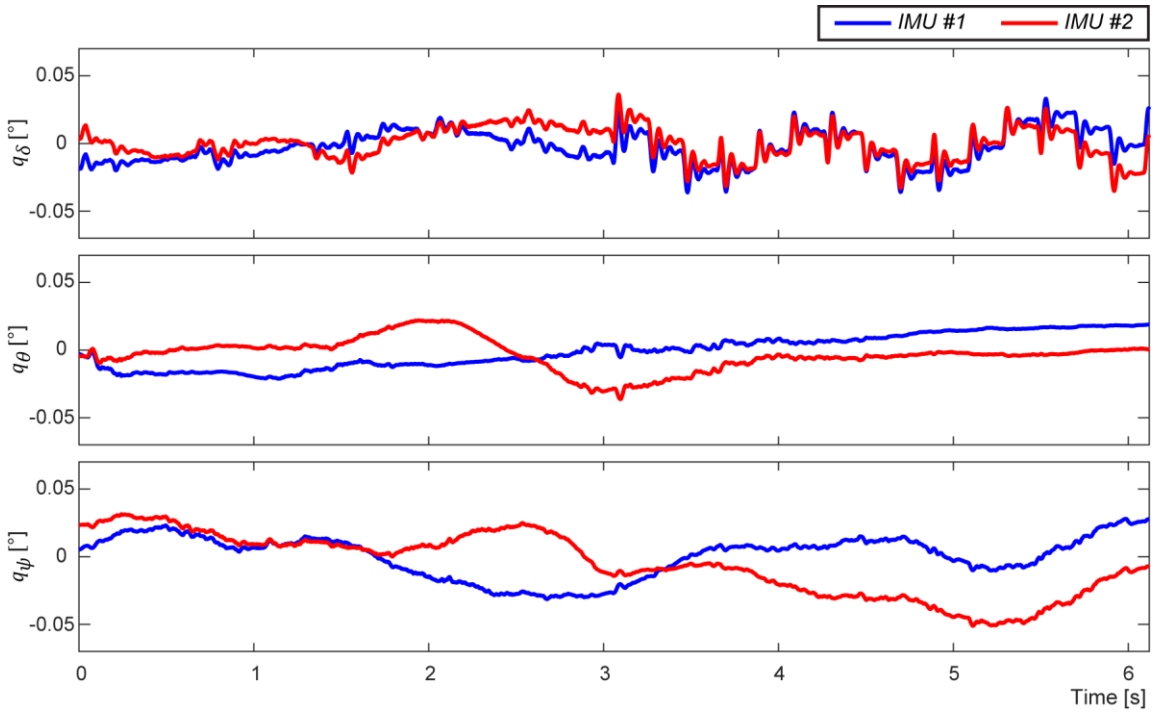

Figure 6-23 Averaged angles of IMU #1 and IMU #2.

However, the angles q_δ, q_θ, and q_ψ are not consistent between the two measurements. Different patterns of the low-frequency perturbations can be seen. The following discusses the cause of this measurement discrepancy.

First, low-frequency perturbations must exist because of the geometric imperfection error of the machine assembly, such as the linear axis also inducing parasitic rotational and off-axis movements, or the rotational axis not being perfectly perpendicular to the linear axis. However, even if geometric error exists, such perturbation behavior should be consistent and independent to the sensors and mounting locations.

The author found that the scale factor variation of the IMUs could be the problem. Scale factor variation listed in the product specification in Table 6-4 is 0.5%. According to the results of multiple tests, the scale factors of the gyros are found to be random and time-varying. Such variation could be around 0.2~0.5%. Hence, for example, assuming the error of scaling factor is 0.2%, and given that the maximum rotation speed of A-axis is 110 °/s (see the testing trajectory in Figure 6-12 and Table 6-2), rotation at 110 °/s for one second will lead to 0.22° error ($110°/s \times 0.2\% \times 1s = 0.22°$). Furthermore, other sensor errors such as non-orthogonality and G-sensitivity will cause additional errors to the

measurements. Currently, the discrepancy of the experimental data shown in Figure 6-23 is around ± 0.04˚. Further reduction is very difficult and impractical because it is beyond the performance of this type of sensor. Alternatively, considering the cost, choosing higher-accuracy sensors such as fiber optic gyroscopes is also impractical for this application. Nonetheless, $\dot{q}_\delta$ and $\ddot{q}_\delta$ can be consistently estimated, which are still very helpful in the dynamic model estimation presented in the next chapter. Also, it is acknowledged that it is difficult to verify the accuracy of the reconstructed $\dot{q}_\delta$ and $\ddot{q}_\delta$ by another referenced instrument, due to the complex experimental trajectory containing both linear and rotary movements. Nevertheless, it is indirectly verified by the prediction accuracy of the identified dynamic model presented in the next chapter.

6.6 Conclusion

This chapter presents the use of a low-cost MEMS IMU to capture the machine structural vibration that cannot be detected by the embedded encoders. The proposed data processing technique first estimates the mounting orientation $\boldsymbol{R}_{S/T}$ and inertial frame orientation $\boldsymbol{R}_{G/M}$ of the IMU such that the estimated vibration is independent to the mounting location and the initial orientation of the IMU.

A flexible multi-axis feed drive was built for the experimental validation. This experimental setup replicates the machine configuration discussed in Section 5.3.2 where significant flexibility is between the linear drive and the rotary drive. A multi-axis simultaneous trajectory was performed on the experimental drive. The structural vibration was excited by high acceleration and jerk.

The test was repeated 22 times to eliminate the random noise and drift which is inherent in low-cost MEMS IMUs. The experimental results show that vibration in velocity and acceleration ($\dot{q}_\delta$ and $\ddot{q}_\delta$) can be consistently estimated. However, the estimated vibration angle q_δ is unfortunately corrupted with inconsistent low-frequency perturbation due to the sensor's performance limitation. Nonetheless, $\dot{q}_\delta$ and $\ddot{q}_\delta$ is still helpful in the dynamic model estimation presented in the next chapter.

Chapter 7
Experimental Results of the Identification Considering Mechanical Flexibility

7.1 Introduction

In Section 5.3.2, it is found that the case with missing internal structural vibration requires an additional sensor for the model identification. In Chapter 6, an experimental feed drive with an IMU was built for this study. In Section 6.5, a multi-axis simultaneous trajectory was tested on the experimental drive. By incorporating the collected servo data and IMU data, the velocity and acceleration of the structural vibration ($\dot{q}_\delta$ and $\ddot{q}_\delta$) have been reconstructed. In this chapter, the collected servo data as well as the reconstructed structural vibration will be used to identify the dynamic model derived in Section 5.3.2.

The identification of the open-loop dynamics is presented in Section 7.2. Model simplification was made due to the lack of accurate measurement of q_δ. In the next step, the identification of closed-loop LTO dynamics is presented in in Section 7.3. Lastly in Section 7.4, the identified model was validated by predicting the responses to external impulse hammer forces.

7.2 Identification of Open-Loop Dynamics

As the identification procedure in Section 4.2.4, the purpose of step 4.1 and 4.2 is to construct the predicted generalized disturbance $\widehat{\boldsymbol{d}}$. The parameters of $\boldsymbol{d}$ are obtained by performing the identification of open-loop dynamics, i.e., Eq. (5.4) and Eq. (5.5). However, q_δ and $q_{A'}$ ($q_{A'} = q_\delta + q_A$) appear in these equations. The angle q_δ reconstructed in Section 6.5 is unfortunately corrupted by unwanted low-frequency drift and cannot be directly used for model identification. Only the time derivative terms $\dot{q}_\delta$ and $\ddot{q}_\delta$ are consistent and accurate. The direct use of q_δ and $q_{A'}$ is avoided by the following approach.

(1) First, given that q_δ is close to zero, the following approximations are made:

$$\begin{cases} \ddot{q}_\delta \cos(q_\delta) \cong \ddot{q}_\delta \\ {\dot{q}_\delta}^2 \sin(q_\delta) \cong 0 \\ \cos(q_{A'}) = \cos(q_A + q_\delta) \cong \cos(q_A) \\ \sin(q_{A'}) = \sin(q_A + q_\delta) \cong \sin(q_A) \end{cases} \tag{7.1}$$

(2) $-\varphi \sin(q_\delta)$ in Eq. (5.5) is the gravity force acting on the connection link. Since q_δ is small, this term can be approximated as $-\varphi q_\delta$ and then merged with the linear spring term $k_\delta q_\delta$ in Eq. (5.4). In other words, φ is not required to be identified.

(3) The parameters of the equations of d_δ in Eq. (5.5) are λ, μ, and the parameters of u_{f_A} and u_{p_A}. Since these parameters also appear in the equation of d_A and d_Y, the equations of motion for the connection link with flexibility can be excluded from the identification.

(4) Regarding u_{f_Y}, u_{f_A}, u_{p_Y}, and u_{p_A}, Coulomb friction is considered, i.e, $u_{f_Y} = C_Y d_n(\dot{q}_Y)$ and $u_{f_A} = C_A d_n(\dot{q}_A)$, where $d_n(\dot{q}_Y)$ and $d_n(\dot{q}_A)$ are the friction models (see Section 3.2). Hence, u_{f_Y} and u_{f_A} are functions of $\dot{q}_Y$ and $\dot{q}_A$. Position-dependent disturbances u_{p_Y} and u_{p_A} are modeled by a lookup table with linear interpolation (see Section 3.2). Therefore, u_{p_Y} and u_{p_A} are functions of q_Y and q_A.

Implementing the above simplifications, the parameters of $\boldsymbol{d}$ in Eq. (5.5) can be obtained by the identification of the parameters in the following dynamic equations:

$$\begin{cases} u_Y = m_Y \ddot{q}_Y + b_Y \dot{q}_Y - \mu \ddot{q}_\delta + \rho\left(\ddot{q}_{A'} \cos(q_A) - {\dot{q}_{A'}}^2 \sin(q_A)\right) + u_{f_Y} + u_{p_Y} \\ u_A = I_A \ddot{q}_{A'} + b_A \dot{q}_A + \lambda\left(-\ddot{q}_\delta \cos(q_A) - {\dot{q}_\delta}^2 \sin(q_A)\right) + \rho \ddot{q}_Y \cos(q_A) + \psi \sin(q_A) + u_{f_A} + u_{p_A} \end{cases} \tag{7.2}$$

As can be seen, q_δ and $q_{A'}$ do not appear in the above equation. All the variables are available as measurements or estimates. Thus, the data collected from the experiment in Section 6.5 was used to identify the dynamic parameters following the LS-based parameter identification approach illustrated in Section 3.3. To enhance the data quality for model identification, a velocity threshold is applied to remove the servo data of which the velocity of the linear and rotary axes are below 2 mm/s and 10^{-3} °/s respectively. The parameter estimates are summarized in Table 7-1.

Table 7-1 The identified dynamic parameters.

m_Y [kg]	μ [kg·m]	ρ [kg·m]	I_A [kg·m^2]	λ [kg·m^2]
5.57E+01	1.18E+01	8.86E-01	1.24E-01	2.57E-01
ψ [N·m]	C_Y [N]	b_Y [N/(m/s)]	C_A [N·m]	b_A[N·m/s]
8.47E+00	1.99E+01	4.95E+01	2.96E-01	3.63E-02

The motor force and torque predicted by the identified open-loop dynamic model are shown in Figure 7-1. To demonstrate the necessity of considering the machine flexibility, the prediction of the identified model has been compared with the prediction of a rigid-body model, where the connection between the linear and rotary drives were assumed to be infinitely stiff, and thus the $\ddot{q}_\delta$ and $\dot{q}_\delta$ related terms were neglected:

$$\begin{cases} u_Y = m_Y \ddot{q}_Y + b_Y \dot{q}_Y + \rho\left(\ddot{q}_A \cos(q_A) - \dot{q}_A{}^2 \sin(q_A)\right) + u_{f_Y} + u_{p_Y} \\ u_A = I_A \ddot{q}_A + b_A \dot{q}_A + \rho \ddot{q}_Y \cos(q_A) + \psi \sin(q_A) + u_{f_A} + u_{p_A} \end{cases} \tag{7.3}$$

As seen from Figure 7-1, the oscillatory behavior for the motor force and torque cannot be captured by the rigid-body model, leading to larger prediction errors as compared in Table 7-2. On the contrary, the prediction of the proposed flexible model accurately captures the structural vibration.

Table 7-2 RMS prediction error of motor force/torque.

	Linear axis u_Y [N]	Tilting axis u_A [N·m]
Rigid-body model	8.786	0.1314
Flexible model	2.771	0.1050

Figure 7-1 Prediction of motor force/torque by the identified open-loop dynamics.

7.3 MIMO Identification with Nonlinear Coupling

The MIMO LTI models of the closed-loop linear dynamics were developed in Section 5.3.2, where the Y-axis and A-axis were modeled by a 2×2 5th-order system and a 3×3 7th-order system, respectively. The predicted generalized disturbance $\widehat{\boldsymbol{d}}$ is reconstructed with the help of the parameters identified in Section 7.2. Then, $\widehat{\boldsymbol{d}}$ along with the collected $\boldsymbol{q}_r$ $\boldsymbol{u}$ and $\boldsymbol{e}$ are used as training data to identify the MIMO LTI model by the method of pole search with LS projection, as explained in Section 4.2.3.

Table 7-3 presents the estimated pole locations. $p_{2,Y}$ $p_{3,Y}$, $p_{2,A}$, and $p_{3,A}$ are pre-assigned high-frequency poles for the velocity and acceleration feedforward control, to realize causal implementations of the time-derivative. $\omega_{n_{2,A}}$ and $\zeta_{2,A}$ are complex pole pairs representing the structural resonance with low damping ratio. The same frequency was also verified by hammer tests (see Appendix A). The rest of the poles represent the dynamics from the interaction of the inertia with the decoupled servo feedback control laws.

It is worth noting that the proposed approach did not directly identify the parameters of the stiffness and damping of the flexible connection. Instead, they are implicitly expressed by an equivalent complex pole pair in the MIMO LTI closed-loop dynamic model.

Table 7-3 Estimated pole locations.

	Estimated pole locations		Search bounds	
			Min.	Max.
Linear Y-axis	$p_{1,Y}$ [Hz]	17.1	1	100
	$\omega_{n_{1,Y}}$ [Hz]	13.0	1	100
	$\zeta_{1,Y}$ []	0.628	0.1	1.5
	$p_{2,Y}$ & $p_{3,Y}$ [Hz]	1200, 1200	Pre-assigned	
Tilting A-axis	$p_{1,A}$ [Hz]	33.6	1	100
	$\omega_{n_{1,A}}$ [Hz]	7.84	1	100
	$\zeta_{1,A}$	0.884	0.1	1.5
	$\omega_{n_{2,A}}$ [Hz]	19.5	10	50
	$\zeta_{2,A}$ []	0.0538	0.01	0.7
	$p_{2,A}$ & $p_{3,A}$ [Hz]	1200,1200	Pre-assigned	

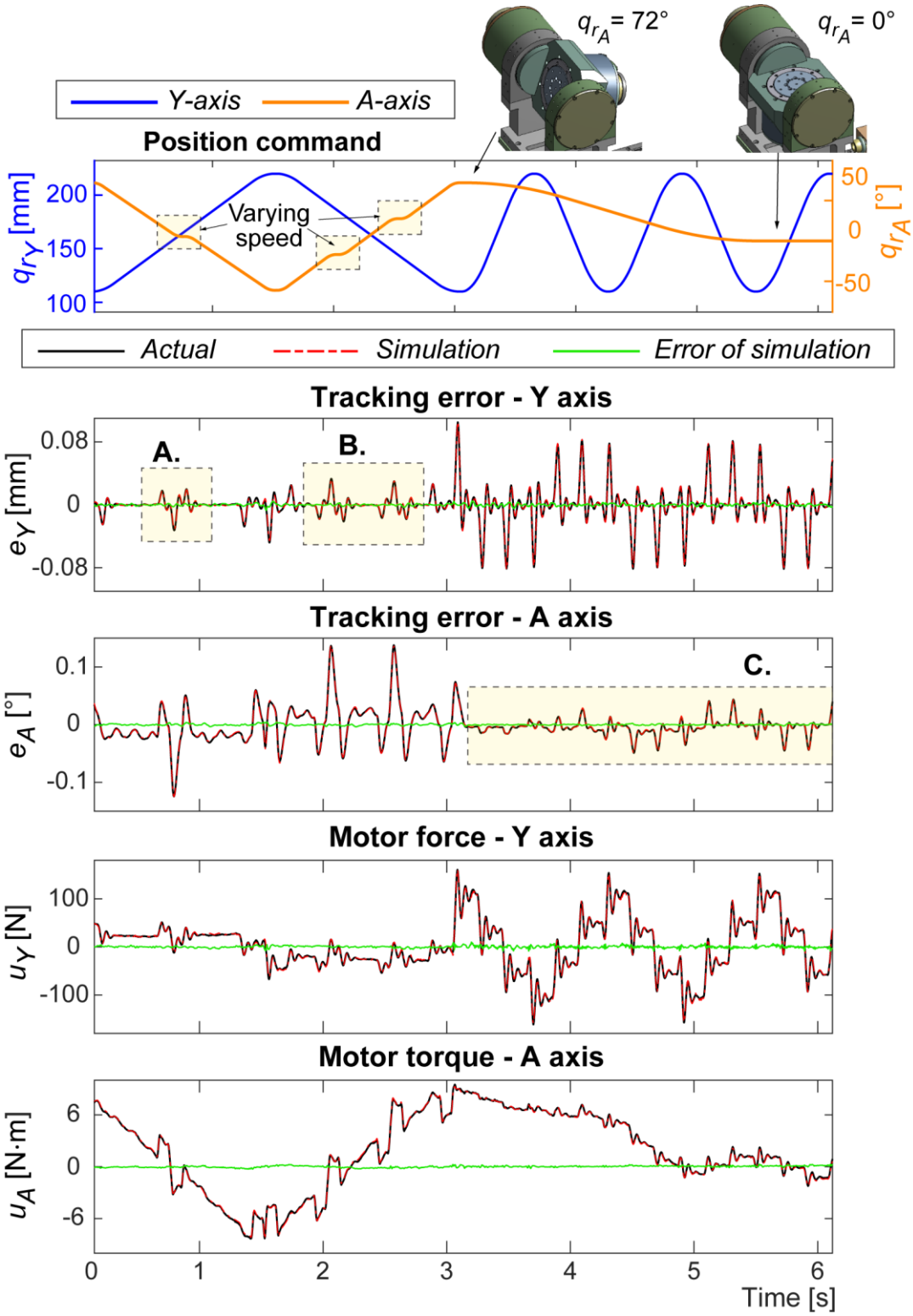

Figure 7-2 Simulation of tracking error and motor force/torque.

The model of the control system as Figure 5-13 can be assembled by integrating the identified MIMO LTI model of the closed-loop linear dynamics, with the generalized disturbance which captures all of the remainder open-loop nonlinear effects. Using this model, the simulation predictions for the servo error and motor actuation commands, in response to the trajectory used in the identification experiment, were obtained as shown in Figure 7-2 and Figure 7-3. The accuracy of the prediction is designated in Table 7-4, where the normalized RMS prediction errors are only 2~6%.

Table 7-4 Error of prediction.

	Y-Axis		A-Axis	
	Tracking error e_Y [mm]	Motor force u_Y [N]	Tracking error e_A [˚]	Motor torque u_A [N·m]
RMS error	1.339E-03	2.106E+00	1.193E-03	9.874E-02
Normalized RMS error	6.19%	3.89%	4.19%	2.03%

Normalized RMS error = RMS error ÷ RMS magnitude

In Figure 7-2, in Zone A and Zone B, the Y-axis is moving at constant velocity while the velocity of A-axis is varying. Acceleration of the A-axis causes considerable vibratory tracking error in the Y-axis. Thus, the model identified purely with CNC and IMU signals is able to accurately predict such inter-axis vibratory coupling. In Zone C, the A-axis is gradually moving from 72˚ to 0˚. The tracking error of the A-axis induced by the back-and-forth motion of the Y-axis is growing accordingly. Such a posture-dependent effect is also accurately captured with the model identified according to the proposed method.

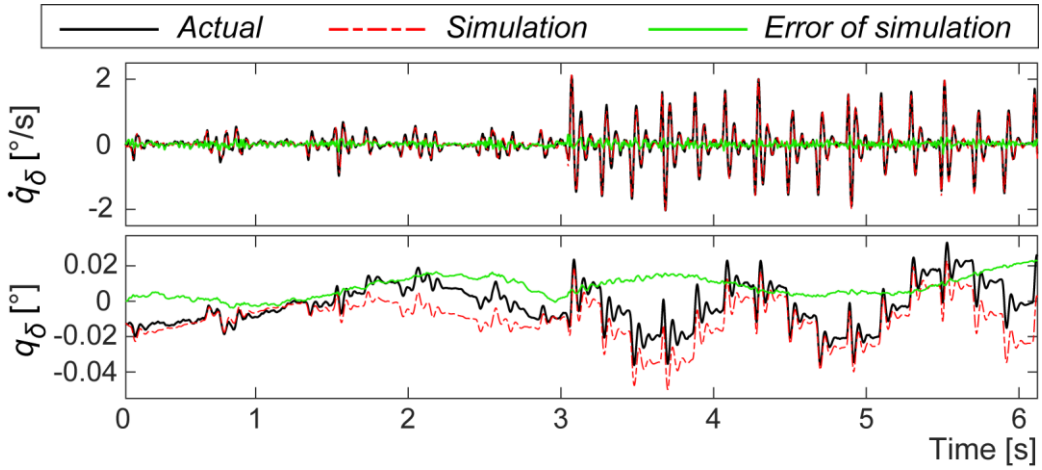

Figure 7-3 Simulation of vibration velocity and angle ($\dot{q}_\delta$ and q_δ).

The structural vibration variables q_δ and $\dot{q}_\delta$ are also simulated, as shown in Figure 7-3. However, large simulation error is found in q_δ due to measurement limitations of the IMU, as already discussed in

Section 6.5. Also, as discussed earlier, an accurate model can still be identified, which adequately replicates the observed behavior (in terms of tracking errors and motor actuation command) from all of the servo channels.

To ensure that the identified model is accurate and not overfitting, the identified model is validated by another trajectory. The results are reported in Appendix C. The average of the normalized RMS error becomes 5.54%, which is only slightly higher the original one (4.08%). Overall, such accuracy in the validation is still well accepted for the application of process planning and monitoring.

7.4 Dynamic Modelling Considering External Force

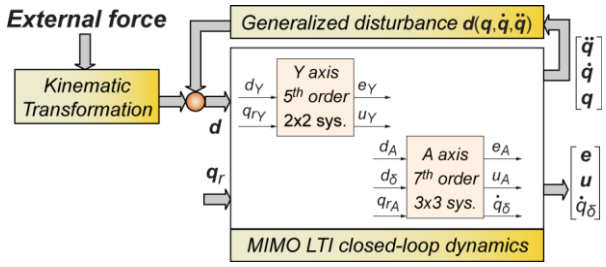

Figure 7-4 Dynamic model considering external force.

The physics-based model identified in Section 7.3, can also be applied to predict the response to external forces. This is done by considering the kinematic transformation [4] as shown in Figure 7-4. In the context of machine tools, the external force can refer to the cutting (or other process) forces. To validate such modeling, an external force has been injected by an impulse hammer, by hitting the left side and right side of the table at 32° and 73° tilting angles, respectively. The measured and simulated servo responses are shown in Figure 7-5. As a posture-dependent dynamic system, the vibratory responses are different, depending on the excitation locations and A-axis tilt angles. As can be seen, such behavior can be accurately simulated. This validation reveals that even only using the excitation of time-domain trajectory, a dynamic model for predicting the responses to both trajectory commands, and also external disturbance forces, can be successfully identified.

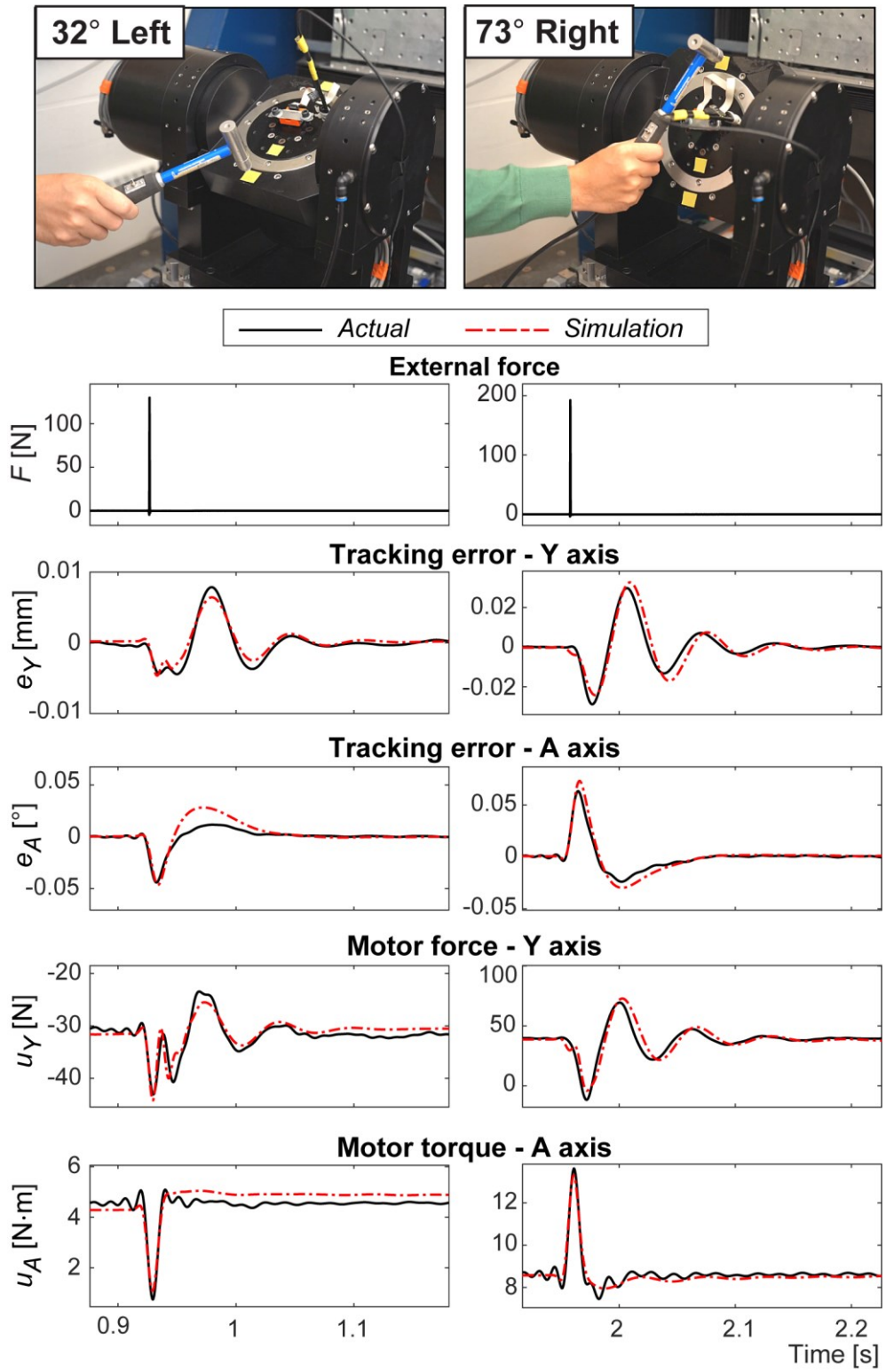

Figure 7-5 Dynamic Simulation considering external force.

7.5 Conclusion

In this chapter, the dynamic model proposed in Section 5.3.2 is validated. Since the measurements of q_δ and q_A by the IMU are not accurate, the identification of open-loop dynamics is simplified to avoid using such data. The parameters of generalized disturbance $\boldsymbol{d}$ can still be obtained from the simplified model. The prediction results show that the vibratory behavior observed in motor force/torque is captured by the open-loop dynamic model considering the structural flexibility.

Then, the proposed MIMO LTI model is identified and validated. The identified MIMO LTI closed-loop dynamic model integrated with the generalized disturbance is able to accurately simulate the tracking error and motor force/torque induced by inter-axis vibratory coupling effect and posture-dependent effect, where the normalized RMS prediction errors are only 2~6%. Such simulation accuracy is well accepted for the application of process planning and monitoring. Lastly, the hammer test on the experimental feed drive reveals that the model identified by time-domain trajectory is also able to predict the responses to external forces.

Chapter 8
Conclusions and Future Work

8.1 Conclusions and Contributions

This thesis has studied new modeling and identification techniques targeting high-speed multi-axis machine tools. The resulting techniques can be successfully applied for process simulation, optimization, and monitoring. The main conclusions and contributions of this thesis are summarized as follows:

As the first main contribution, a new modeling and identification technique has been proposed in Chapter 4. The model can capture a wide range of dynamic effects, such as inter-axis coupling effects, the influences of actuator force/torque ripples and nonlinear friction, and feedforward/feedback control dynamics. In earlier proposed top-down identification approaches, the modeling was confined to single-axis (decoupled) motion systems. In this thesis, by integrating multi-rigid-body dynamics into the model, multi-axis (coupled) motion control systems can also be modeled from in-situ data.

The proposed method decouples the closed-loop linear dynamics from the open-loop nonlinear dynamics, and also strikes a good compromise between computational load (for parameter estimation) and model accuracy, by searching only for the independent parameters that cannot be solved directly with LS estimation, and directly solving all other dependent parameters for each candidate set of independent parameters, using LS. Although the searched independent parameters rely on global optimization of which the solution may be non-unique, a model that yields sufficiently accurate predictions is still obtained, which is beneficial for industrial application.

This proposed method was validated using an industrial 5-axis laser drilling machine. The model was estimated by the servo data collected during the production, causing minimum machine downtime. Such an approach is in-line with the principles of Industry 4.0. The estimated model achieved 2.38% RMS error in predicting the servo errors and motor torques. Another experimental validation was performed using an in-house feed drive system, with linear and tilting motion. Since the model was built by a physics-based approach, the disturbances from each mechanical factor and their resulting servo error can be respectively predicted and evaluated. Such analysis provides insights into the machine and the process, facilitating machine trouble shooting and process optimization.

The second main contribution, presented in Chapter 5 through Chapter 7, is the extension of the method in Chapter 4 to also identify structural flexibility, which is a crucial characteristic of large-sized high-speed machine tools. In Chapter 5, the interaction possibilities of a flexible linear drive coupled with a rotary drive are systematically analyzed. It is found that in the case where there is significant mechanical flexibility in the attachment between the linear and rotary drives, an additional motion sensor capturing the internal vibration between the feed drives is required for the model identification.

The above requirement is fulfilled in Chapter 6, with the estimation of the relative vibration by fusing signals from a MEMS IMU, as well as servo measurements from the axis encoders. The proposed data processing technique first synchronizes these independent data sets, estimates the orientation of the IMU, calibrates the mounting orientation, and finally extracts the structural vibration between the two feed drives. To the best knowledge of the author, this is among the first studies in the literature where an IMU is used to measure and identify the multibody and vibratory dynamics in a machine tool application.

An experimental feed drive with significant mechanical flexibility was built to validate the proposed dynamic model, measurement, and sensor fusion concept. The experiment shows that the angular velocity and acceleration of the vibration can be consistently estimated. The RMS error between measurements from two different IMUs are 0.0474 $^\circ$/s and 7.33 $^\circ$/s^2 respectively. The vibration angle however cannot be successfully reconstructed, due to the geometric assembly error and the performance limitation of the MEMS IMU. Nonetheless, the estimated velocity and acceleration of the vibration is still very helpful for estimating the overall multibody motion control system model with inherent mechanical flexibility.

Finally, in Chapter 7, the proposed identification method, utilizing the IMU data, is experimentally validated. Also, judicious simplification to the dynamic model helps circumvent the need to explicitly estimate and use the deflection angle data. As a result, the dynamic tracking error and motor force/torque could be predicted, by the identified ‘digital twin’, with 2-6% normalized RMS prediction error. This model, estimated only from a short packet of practical data, successfully considers multiple effects, such as vibratory inter-axis coupling, posture-dependent dynamics, as well as the experimental setup’s own disturbances (like friction, cable spring-back and torque ripples). The achieved prediction accuracy is well-acceptable for machining process planning, optimization, and monitoring in industry.

8.2 Future Work

Ideas for future improvements to this work are proposed in the following:

(a) Validation using non-symmetrical inertia for the rotary axis, and later on large-sized industrial 5-axis machine tools

The proposed modeling and identification for multi-axis flexible drives was validated in this thesis using the lab's experimental setup, a tilt-rotary drive stacked on top of a linear drive. The rotary axis, while contributing to a third degree-of-freedom trajectory and the IMU signal processing, due to its symmetrical nature, had not contributed to dynamic coupling with the tilt and the translating axes. A first step of future research could be to study the configuration where the rotary axis is also coupled with the tilt and linear axes, presumably by including a non-symmetrical inertia attachment.

Afterwards, the overall methodology should be further extended and validated on a large-sized industrial 5-axis machines tool. In such situation, at least two IMUs are required, one at the workpiece side and the other at the tool side. By installing the IMUs at both sides, their relative motion can be captured.

(b) Investigation of the measurement error of IMUs

The angular measurement by IMUs presented in Chapter 6 exhibits undesirable low-frequency drift. Part of the reasons could be the measurement error of the IMUs used during the experiment (although significant care has been taken to select high quality IMUs at a reasonable price point). There are plenty of commercial MEMS IMUs on the market. Some of them claim better measurement accuracy. It is given that different designs of the MEMS result in different signal responses and sensitivities. Thus, it is worth testing other MEMS IMUs with claimed better measurement accuracy, to reduce the measurement error that originate from the sensors.

(c) Measurement of the geometric error by IMUs

As seen in the measurements in Chapter 6, the IMU also captures geometric errors of the machine assembly, which is beyond the scope of this thesis research. Geometric errors could be identified by further tests. For example, Vogl et al. [95] used an IMU to inspect the angular pitch error of a ball screw drive. Other geometric errors, such as squareness and straightness, could also be identified by different measurement strategies. In summary, if the dynamic error as well as the geometric error can both be identified by affordable MEMS IMUs in practical ways, this would be extremely beneficial in terms of

identifying further realistic machine tools digital twins, which not only predict the dynamic responses, but also volumetric positioning errors, and the influence of such errors on the dynamics (e.g., in exciting further vibrations) during high traverse rates.

(d) Vibration reconstruction for multiple flexible joints

The proposed vibration reconstruction method presented in Chapter 6 uses one IMU to reconstruct the motion of one internal flexible joint around one rotation axis (q_δ, per Figure 6-11). First extension would target reconstructing simultaneous vibrations around multiple axes (e.g., by also inducing flexibilities around q_θ and q_ψ axes). Then, further research should focus on reconstructing the motion of 'multiple' internal flexible joints, for example, configured in a structure that connects multiple actuators and links. For such cases, multiple IMUs would be expected to be used on the links, with assumed dominantly rigid characteristics. This would also enable the extension of the proposed methodology to model identification for robots with multiple mechanical flexibilities.

(e) Monitoring of high-speed 5-axis machining process

The model built in this thesis can predict dynamic responses to trajectory commands and external (presumably cutting) forces. It offers a highly effective and versatile foundation of developing cutting force monitoring algorithms for high-speed 5-axis machining process. The inter-axis dynamic coupling effect and the dynamic responses to the external disturbances (i.e., cutting forces) can be both captured and predicted, allowing for tool tip forces to be reconstructed from limited and practical sensor data.

(f) Integration with 5-axis trajectory planning

5-axis trajectory planning is an under-determined problem. Various toolpath planning strategies can be chosen. On the other hand, 5-axis machine dynamics is coupled and posture-dependent, i.e., the motion of one axis can possibly induce tracking errors in another axis. With the aid of a dynamic model, obtained via the proposed method, such complex interactions can be simulated or predicted, enabling more optimal 5-axis trajectory planning.

(g) Posture dependency of linear axes

The proposed dynamic model can capture posture dependency of rotary axes. However, the posture dependency of linear axes is not discussed in this thesis. This could be achieved by building a more sophisticated multibody dynamic model as, for example as achieved by Huynh and Altintas (Figure 5-3 [115]), where multiple flexible joints are used to connect bodies along different directions.

(h) Model identification using both command trajectory and disturbance force input

So far in this thesis, the command trajectory has been the primary excitation source for the model identification, while an instrumented impact force hammer was used for the model validation (as shown in Section 7.4). To further improve the accuracy of the model identification, the command trajectory and an external disturbance force can be used together as the excitation sources [123]. Of course, safety considerations must still be kept in mind, e.g., impact hammer testing on a rapidly moving structure may not be practical or safe. However, a separate mount-on actuator, such as a small shaker or linear motor, with known inertia characteristics can be used for such a purpose.

References

[1] Altintas, Y., Brecher, C., Weck, M., & Witt, S. (2005). Virtual machine tool. CIRP annals, 54(2), 115-138.

[2] Armendia, M., Alzaga, A., Peysson, F., Fuertjes, T., Cugnon, F., Ozturk, E., & Flum, D. (2019). Machine Tool: From the Digital Twin to the Cyber-Physical Systems. In Twin-Control (pp. 3-21). Springer, Cham.

[3] FANUC. High Performance Machining. Online Available: https://www.fanucamerica.com/

[4] Aslan, D., & Altintas, Y. (2018). Prediction of cutting forces in five-axis milling using feed drive current measurements. IEEE/ASME Transactions on Mechatronics, 23(2), 833-844.

[5] Jeschke, S., Brecher, C., Meisen, T., Özdemir, D., & Eschert, T. (2017). Industrial internet of things and cyber manufacturing systems. In Industrial Internet of Things (pp. 3-19). Springer, Cham.

[6] Erkorkmaz, K., & Wong, W. (2007). Rapid identification technique for virtual CNC drives. International Journal of Machine Tools and Manufacture, 47(9), 1381-1392.

[7] Tseng, G. W. G., Chen, C. Q. G., Erkorkmaz, K., & Engin, S. (2019). Digital shadow identification from feed drive structures for virtual process planning. CIRP Journal of Manufacturing Science and Technology, 24, 55-65.

[8] Turhan, M. H., Tseng, G. W. G., Erkorkmaz, K., & Fidan, B. (2020). Dynamic model identification for CNC machine tool feed drives from in-process signals for virtual process planning. Mechatronics, 72, 102445.

[9] Sencer, B., & Altintas, Y. (2011). Identification of 5-axis machine tools feed drive systems for contouring simulation. International Journal of Automation Technology, 5(3), 377-386.

[10] Erkorkmaz, K., & Altintas, Y. (2001). High speed CNC system design. Part II: modeling and identification of feed drives. International Journal of Machine Tools and Manufacture, 41(10), 1487-1509.

[11] Vicente, D. A., Hecker, R. L., Villegas, F. J., & Flores, G. M. (2012). Modeling and vibration mode analysis of a ball screw drive. The International Journal of Advanced Manufacturing Technology, 58(1-4), 257-265.

[12] Frey, S., Dadalau, A., & Verl, A. (2012). Expedient modeling of ball screw feed drives.

Production Engineering, 6(2), 205-211.

[13] Poignet, P., Gautier, M., & Khalil, W. (1999). Modeling, control and simulation of high speed machine tool axes. In 1999 IEEE/ASME International Conference on Advanced Intelligent Mechatronics (Cat. No. 99TH8399) (pp. 617-622). IEEE.

[14] Wang, C. P., Liang, S. P., & Luo, T. L. (2018). A Machine Tool Design Methodology Integrating FEM Analysis and CNC Controller Model. 7th International Conference on Virtual Machining Process Technology (VMPT).

[15] Brecher, C., Altstädter, H., & Daniels, M. (2015). Axis position dependent dynamics of multi-axis milling machines. Procedia CIRP, 31, 508-514.

[16] Zirn, O. (2008). Machine Tool Analysis-Modeling, Simulation and Control of Machine Tool Manipulators. ETH Zurich, Institute of Machine Tools and Manufacturing, Zurich.

[17] Wagner, P. (2016). Simulation in design of high performance machine tool. HELLER Maschinenfabrik GmbH.

[18] Kehl, G., Hofsäss, U., Lwowski , W., Ma, J., & Wagner, P. (2015). Responding to frequently asked questions of machine tool design-engineers by application of finite element analysis. Fourth African Conference on Computational Mechanics, Morocco.

[19] Luo, T., Wang, C., Liang, S. (2016). A Process Stability Enhanced Machine Tool Design Method Integrated Dynamic Stiffness Topology Optimization. The 17th International Conference on Machine Design and Production.

[20] Budak, E., Matsubara, A., Donmez, A., & Munoa, J. (2022). Mechanical interfaces in machine tools. CIRP Annals.

[21] Bograd, S., Reuss, P., Schmidt, A., Gaul, L., & Mayer, M. (2011). Modeling the dynamics of mechanical joints. Mechanical Systems and Signal Processing, 25(8), 2801-2826.

[22] Konowalski, K. (2009). Experimental research and modeling of normal contact stiffness and contact damping of machined joint surfaces. Advances in Manufacturing Science and Technology, 33(3), 53-68.

[23] Tiwari, R., Lees, A. W., & Friswell, M. I. (2004). Identification of dynamic bearing parameters: a review. Shock and Vibration Digest, 36(2), 99-124.

[24] Brecher, C., Fey, M., & Bäumler, S. (2013). Damping models for machine tool components of

linear axes. CIRP Annals, 62(1), 399-402.

[25] Armstrong-Hélouvry, B., Dupont, P., & De Wit, C. C. (1994). A survey of models, analysis tools and compensation methods for the control of machines with friction. Automatica, 30(7), 1083-1138.

[26] Haug, E. (2018). Simulation of friction and stiction in multibody dynamics model problems. Mechanics Based Design of Structures and Machines, 46(3), 296-317.

[27] Karnopp, D. (1985). Computer simulation of stick-slip friction in mechanical dynamic systems. Journal of dynamic systems, measurement, and control, 107(1), 100-103.

[28] Brown, P., & McPhee, J. (2016). A continuous velocity-based friction model for dynamics and control with physically meaningful parameters. Journal of Computational and Nonlinear Dynamics, 11(5).

[29] Haug, E. J. (1989). Computer aided kinematics and dynamics of mechanical systems.

[30] Lampaert, V., Al-Bender, F., & Swevers, J. (2004). Experimental characterization of dry friction at low velocities on a developed tribometer setup for macroscopic measurements. Tribology Letters, 16(1-2), 95-105.

[31] Dahl, P. R. (1968). A solid friction model (No. TOR-0158 (3107-18)-1). Aerospace Corp El Segundo Ca.

[32] De Wit, C. C., Olsson, H., Astrom, K. J., & Lischinsky, P. (1995). A new model for control of systems with friction. IEEE Transactions on automatic control, 40(3), 419-425.

[33] Swevers, J., Al-Bender, F., Ganseman, C. G., & Projogo, T. (2000). An integrated friction model structure with improved presliding behavior for accurate friction compensation. IEEE Transactions on automatic control, 45(4), 675-686.

[34] Lampaert, V., Swevers, J., & Al-Bender, F. (2002). Modification of the Leuven integrated friction model structure. IEEE transactions on Automatic Control, 47(4), 683-687.

[35] Al-Bender, F., Lampaert, V., & Swevers, J. (2005). The generalized Maxwell-slip model: a novel model for friction simulation and compensation. IEEE Transactions on automatic control, 50(11), 1883-1887.

[36] Yeung, C. H., Altintas, Y., & Erkorkmaz, K. (2006). Virtual CNC system. Part I. system architecture. International Journal of Machine Tools and Manufacture, 46(10), 1107-1123.

[37] Erkorkmaz, K., Yeung, C. H., & Altintas, Y. (2006). Virtual CNC system. Part II. High speed contouring application. International Journal of Machine Tools and Manufacture, 46(10), 1124-1138.

[38] Sato, R. (2012). Development of a feed drive simulator. In Key Engineering Materials (Vol. 516, pp. 154-159). Trans Tech Publications.

[39] Wong, W. W. S., & Erkorkmaz, K. (2010). Constrained identification of virtual CNC drives using a genetic algorithm. The International Journal of Advanced Manufacturing Technology, 50(1-4), 275-288.

[40] Bohez, E. L. (2002). Five-axis milling machine tool kinematic chain design and analysis. International Journal of Machine Tools and Manufacture, 42(4), 505-520.

[41] Sakamoto, S. (1993). Analysis of generating motion for five-axis machining centers. Transactions of NAMRI/SME, 287.

[42] Landers, R. G., Min, B. K., & Koren, Y. (2001). Reconfigurable machine tools. CIRP Annals, 50(1), 269-274.

[43] Moriwaki, T. (2008). Multi-functional machine tool. CIRP Annals, 57(2), 736-749.

[44] Zhu, Z., Dhokia, V. G., Nassehi, A., & Newman, S. T. (2013). A review of hybrid manufacturing processes–state of the art and future perspectives. International Journal of Computer Integrated Manufacturing, 26(7), 596-615.

[45] DMG MORI. Machines Overview. Online Available: https://en.dmgmori.com/products/machines/.

[46] Spong, M. W., & Vidyasagar, M. (2008). Robot dynamics and control. John Wiley & Sons.

[47] Mayeda, H., Yoshida, K., & Osuka, K. (1990). Base parameters of manipulator dynamic models. IEEE Transactions on Robotics and Automation, 6(3), 312-321.

[48] Abele, E., Weigold, M., & Rothenbücher, S. (2007). Modeling and identification of an industrial robot for machining applications. CIRP annals, 56(1), 387-390.

[49] Chen, Y., & Dong, F. (2013). Robot machining: recent development and future research issues. The International Journal of Advanced Manufacturing Technology, 66(9-12), 1489-1497.

[50] Iglesias, I., Sebastián, M. A., & Ares, J. E. (2015). Overview of the state of robotic machining: Current situation and future potential. Procedia engineering, 132, 911-917.

[51] Verl, A., Valente, A., Melkote, S., Brecher, C., Ozturk, E., & Tunc, L. T. (2019). Robots in machining. CIRP Annals, 68(2), 799-822.

[52] Cen, L., & Melkote, S. N. (2017). Effect of robot dynamics on the machining forces in robotic milling. Procedia Manufacturing, 10, 486-496.

[53] Cvitanic, T., Nguyen, V., & Melkote, S. N. (2020). Pose optimization in robotic machining using static and dynamic stiffness models. Robotics and Computer-Integrated Manufacturing, 66, 101992.

[54] Spong, M. W. (1987). Modeling and control of elastic joint robots. Journal of dynamic systems, measurement, and control, 109(4), 310-318.

[55] Tomei, P. (1991). A simple PD controller for robots with elastic joints. IEEE Transactions on automatic control, 36(10), 1208-1213.

[56] Shabana, A. A. (2020). Dynamics of multibody systems. Cambridge university press.

[57] Dwivedy, S. K., & Eberhard, P. (2006). Dynamic analysis of flexible manipulators, a literature review. Mechanism and machine theory, 41(7), 749-777.

[58] De Luca, A. (2000). Feedforward/feedback laws for the control of flexible robots. In Proceedings 2000 ICRA. Millennium Conference. IEEE International Conference on Robotics and Automation. Symposia Proceedings (Cat. No. 00CH37065) (Vol. 1, pp. 233-240). IEEE.

[59] Moberg, S. (2010). Modeling and control of flexible manipulators (Doctoral dissertation, Linköping University Electronic Press).

[60] Book, W. J. (1984). Recursive Lagrangian dynamics of flexible manipulator arms. The International Journal of Robotics Research, 3(3), 87-101.

[61] Siciliano, B., & Book, W. J. (1988). A singular perturbation approach to control of lightweight flexible manipulators. The International Journal of Robotics Research, 7(4), 79-90.

[62] Khosla, P. K., & Kanade, T. (1985, December). Parameter identification of robot dynamics. In 1985 24th IEEE Conference on Decision and Control (pp. 1754-1760). IEEE.

[63] Atkeson, C. G., An, C. H., & Hollerbach, J. M. (1986). Estimation of inertial parameters of manipulator loads and links. The International Journal of Robotics Research, 5(3), 101-119.

[64] Gautier, M., & Khalil, W. (1988). On the identification of the inertial parameters of robots. In Proceedings of the 27th IEEE Conference on Decision and Control (pp. 2264-2269). IEEE.

[65] Olsen, H., & Bekey, G. (1986). Identification of robot dynamics. In Proceedings. 1986 IEEE International Conference on Robotics and Automation (Vol. 3, pp. 1004-1010). IEEE.

[66] Khalil, W., & Dombre, E. (2004). Modeling, identification and control of robots. Butterworth-Heinemann.

[67] Wu, J., Wang, J., & You, Z. (2010). An overview of dynamic parameter identification of robots. Robotics and computer-integrated manufacturing, 26(5), 414-419.

[68] Swevers, J., Verdonck, W., & De Schutter, J. (2007). Dynamic model identification for industrial robots. IEEE control systems magazine, 27(5), 58-71.

[69] Gautier, M. (1997). Dynamic identification of robots with power model. In Proceedings of International Conference on Robotics and Automation (Vol. 3, pp. 1922-1927). IEEE.

[70] Gautier, M., & Poignet, P. (2001). Extended Kalman filtering and weighted least squares dynamic identification of robot. Control Engineering Practice, 9(12), 1361-1372.

[71] Swevers, J., Ganseman, C., Tukel, D. B., De Schutter, J., & Van Brussel, H. (1997). Optimal robot excitation and identification. IEEE transactions on robotics and automation, 13(5), 730-740.

[72] Ljung, L. (1999). System identification. Wiley Encyclopedia of Electrical and Electronics Engineering, 1-19.

[73] Gautier, M., & Khalil, W. (1992). Exciting trajectories for the identification of base inertial parameters of robots. The International journal of robotics research, 11(4), 362-375.

[74] Albu-Schaffer, A., & Hirzinger, G. (2001). Parameter identification and passivity based joint control for a 7 DOF torque controlled light weight robot. In Proceedings 2001 ICRA. IEEE International Conference on Robotics and Automation (Cat. No. 01CH37164) (Vol. 3, pp. 2852-2858). IEEE.

[75] Pham, M. T., Gautier, M., & Poignet, P. (2001). Identification of joint stiffness with bandpass filtering. In Proceedings 2001 ICRA. IEEE International Conference on Robotics and Automation (Cat. No. 01CH37164) (Vol. 3, pp. 2867-2872). IEEE.

[76] Pham, M. T., Gautier, M., & Poignet, P. (2002). Accelerometer based identification of mechanical systems. In Proceedings 2002 IEEE International Conference on Robotics and Automation (Cat. No. 02CH37292) (Vol. 4, pp. 4293-4298). IEEE.

[77] Östring, M., Gunnarsson, S., & Norrlöf, M. (2003). Closed-loop identification of an industrial robot containing flexibilities. Control Engineering Practice, 11(3), 291-300.

[78] Öhr, J., Moberg, S., Wernholt, E., Hanssen, S., Pettersson, J., Persson, S., & Sander-Tavallaey, S. (2006). Identification of flexibility parameters of 6-axis industrial manipulator models. Technical reports. Linköping University Electronic Press.

[79] Lightcap, C., & Banks, S. (2007). Dynamic identification of a mitsubishi pa10-6ce robot using motion capture. In 2007 IEEE/RSJ International Conference on Intelligent Robots and Systems (pp. 3860-3865). IEEE.

[80] Oaki, J., & Adachi, S. (2009). Decoupling identification for serial two-link robot arm with elastic joints. IFAC Proceedings Volumes, 42(10), 1417-1422.

[81] Wernholt, E., & Moberg, S. (2011). Nonlinear gray-box identification using local models applied to industrial robots. Automatica, 47(4), 650-660.

[82] Moberg, S., Wernholt, E., Hanssen, S., & Brogårdh, T. (2014). Modeling and parameter estimation of robot manipulators using extended flexible joint models. Journal of Dynamic Systems, Measurement, and Control, 136(3), 031005.

[83] Gaz, C., Flacco, F., & De Luca, A. (2014). Identifying the dynamic model used by the KUKA LWR: A reverse engineering approach. In 2014 IEEE international conference on robotics and automation (ICRA) (pp. 1386-1392). IEEE.

[84] Miranda-Colorado, R., & Moreno-Valenzuela, J. (2018). Experimental parameter identification of flexible joint robot manipulators. Robotica, 36(3), 313-332.

[85] Ruderman, M., Hoffmann, F., & Bertram, T. (2009). Modeling and identification of elastic robot joints with hysteresis and backlash. IEEE Transactions on Industrial Electronics, 56(10), 3840-3847.

[86] Alici, G., & Shirinzadeh, B. (2005). Enhanced stiffness modeling, identification and characterization for robot manipulators. IEEE transactions on robotics, 21(4), 554-564.

[87] Dumas, C., Caro, S., Garnier, S., & Furet, B. (2011). Joint stiffness identification of six-revolute industrial serial robots. Robotics and Computer-Integrated Manufacturing, 27(4), 881-888.

[88] Gao, W., Kim, S. W., Bosse, H., Haitjema, H., Chen, Y. L., Lu, X. D., ... & Kunzmann, H. (2015). Measurement technologies for precision positioning. CIRP Annals, 64(2), 773-796.

[89] Heidenhain. (2015). User's Manual ACCOM.

[90] Ibaraki, S., Kakino, Y., Lee, K., Ihara, Y., Braasch, J., & Eberherr, A. (1970). Diagnosis and compensation of motion errors in NC machine tools by arbitrary shape contouring error measurement. WIT Transactions on Engineering Sciences, 34.

[91] Law, M., Gupta, P., & Mukhopadhyay, S. (2020). Modal analysis of machine tools using visual vibrometry and output-only methods. CIRP Annals, 69(1), 357-360.

[92] Abir, J., Longo, S., Morantz, P., & Shore, P. (2016). Optimized estimator for real-time dynamic displacement measurement using accelerometers. Mechatronics, 39, 1-11.

[93] Ahmad, N., Ghazilla, R. A. R., Khairi, N. M., & Kasi, V. (2013). Reviews on various inertial measurement unit (IMU) sensor applications. International Journal of Signal Processing Systems, 1(2), 256-262.

[94] Woodman, O. J. (2007). An introduction to inertial navigation (No. UCAM-CL-TR-696). University of Cambridge, Computer Laboratory.

[95] Vogl, G. W., Donmez, M. A., & Archenti, A. (2016). Diagnostics for geometric performance of machine tool linear axes. CIRP annals, 65(1), 377-380.

[96] Manon Kok, Jeroen D. Hol and Thomas B. Sch¨on (2017), "Using Inertial Sensors for Position and Orientation Estimation", Foundations and Trends in Signal Processing: Vol. 11: No. 1-2, pp 1-153.

[97] Honeywell. Compare our inertial measurement units [Online]. Available https://aerospace.honeywell.com/us/en/learn/products/sensors/inertial-measurement-units [Accessed 2022 January]

[98] Passaro, V., Cuccovillo, A., Vaiani, L., De Carlo, M., & Campanella, C. E. (2017). Gyroscope technology and applications: A review in the industrial perspective. Sensors, 17(10), 2284.

[99] Xsens. Inertial Sensor Modules [Online]. Available https://www.xsens.com/inertial-sensor-modules [Accessed 2022 January]

[100] Rehbinder, H., & Hu, X. (2004). Drift-free attitude estimation for accelerated rigid bodies. Automatica, 40(4), 653-659.

[101] Luinge, H. J., & Veltink, P. H. (2005). Measuring orientation of human body segments using miniature gyroscopes and accelerometers. Medical and Biological Engineering and computing,

43(2), 273-282.

[102] Sabatini, A. M. (2006). Quaternion-based extended Kalman filter for determining orientation by inertial and magnetic sensing. IEEE transactions on Biomedical Engineering, 53(7), 1346-1356.

[103] Suh, Y. S. (2010). Orientation estimation using a quaternion-based indirect Kalman filter with adaptive estimation of external acceleration. IEEE Transactions on Instrumentation and Measurement, 59(12), 3296-3305.

[104] Yoo, T. S., Hong, S. K., Yoon, H. M., & Park, S. (2011). Gain-scheduled complementary filter design for a MEMS based attitude and heading reference system. Sensors, 11(4), 3816-3830.

[105] Lee, J. K., Park, E. J., & Robinovitch, S. N. (2012). Estimation of attitude and external acceleration using inertial sensor measurement during various dynamic conditions. IEEE transactions on instrumentation and measurement, 61(8), 2262-2273.

[106] Valenti, R. G., Dryanovski, I., & Xiao, J. (2015). Keeping a good attitude: A quaternion-based orientation filter for IMUs and MARGs. Sensors, 15(8), 19302-19330.

[107] Diebel, J. (2006). Representing attitude: Euler angles, unit quaternions, and rotation vectors. Matrix, 58(15-16), 1-35.

[108] Mahony, R., Hamel, T., & Pflimlin, J. M. (2008). Nonlinear complementary filters on the special orthogonal group. IEEE Transactions on automatic control, 53(5), 1203-1218.

[109] Madgwick, S. O., Harrison, A. J., & Vaidyanathan, R. (2011). Estimation of IMU and MARG orientation using a gradient descent algorithm. In 2011 IEEE international conference on rehabilitation robotics (pp. 1-7). IEEE.

[110] Vydhyanathan, A, & Bellusci, G. (2018) The Next Generation Xsens Motion Trackers for Industrial Applications. Version 2.0.5. Xsens, The Netherlands.

[111] McPhee, J. J. (1996). On the use of linear graph theory in multibody system dynamics. Nonlinear Dynamics, 9(1-2), 73-90.

[112] Global Optimization Toolbox, The MathWorks Inc., Natick MA.

[113] Monkhorst, W. (2004) Dynamic Error Budgeting – A Design Approach. Master thesis. Delft University of Technology, Delft.

[114] FANUC America. FANUC R-1000IA Series Robot [Online]. Available https:// https://www.fanucamerica.com/products/robots/series/r-1000ia [Accessed 2022 April].

[115] Huynh, H. N., & Altintas, Y. (2021). Modeling the dynamics of five-axis machine tool using the multibody approach. Journal of Manufacturing Science and Engineering, 143(2).

[116] Huynh, H. N., & Altintas, Y. (2022). Multibody dynamic modeling of five-axis machine tool vibrations and controller. CIRP Annals.

[117] Rankers, A. M. (1998). Machine dynamics in mechatronic systems: An engineering approach. PhD Thesis, Universiteit Twente.

[118] Erkorkmaz, K., & Hosseinkhani, Y. (2013). Control of ball screw drives based on disturbance response optimization. CIRP Annals, 62(1), 387-390.

[119] HURCO. Benefits of Trunnion 5-Axis Mill [Online]. Available https://www.hurco.com/en-us/products/5-axis/Pages/U-trunnion-style-machining-centers.aspx [Accessed 2022 January]

[120] Hiramoto, K., Hansel, A., Ding, S., & Yamazaki, K. (2005). A study on the drive at center of gravity (DCG) feed principle and its application for development of high performance machine tool systems. CIRP annals, 54(1), 333-336.

[121] Quiroga, R. Q., Kraskov, A., Kreuz, T., & Grassberger, P. (2002). Performance of different synchronization measures in real data: a case study on electroencephalographic signals. Physical Review E, 65(4), 041903.

[122] Sorkine-Hornung, O., & Rabinovich, M. (2017). Least-squares rigid motion using svd. Computing, 1(1), 1-5.

[123] Franco, O., Beudaert, X., Erkorkmaz, K., & Munoa, J. (2022). Influence of guideway friction on the cutting point receptance in machine tools. CIRP Annals.

Appendix A

Experimental Setup for the Study of Multi-Axis Flexible Drives

Introduction

To model the dynamics of high-speed 5-axis machine tools, multibody dynamics and vibratory dynamics should both be taken into account. Theoretical investigation on this topic was carried out in Chapter 5. A critical finding from Section 5.3.2 is that if there is significant mechanical flexibility between a linear drive and a rotary drive, then model identification requires not only the servo data from CNC, but also an extra motion sensor to capture the vibration between the linear and rotary drives.

To further investigate this particular case, an experimental feed drive with similar configuration was built. This appendix details the design and verification of this experimental feed drive.

Designing the Experimental Setup

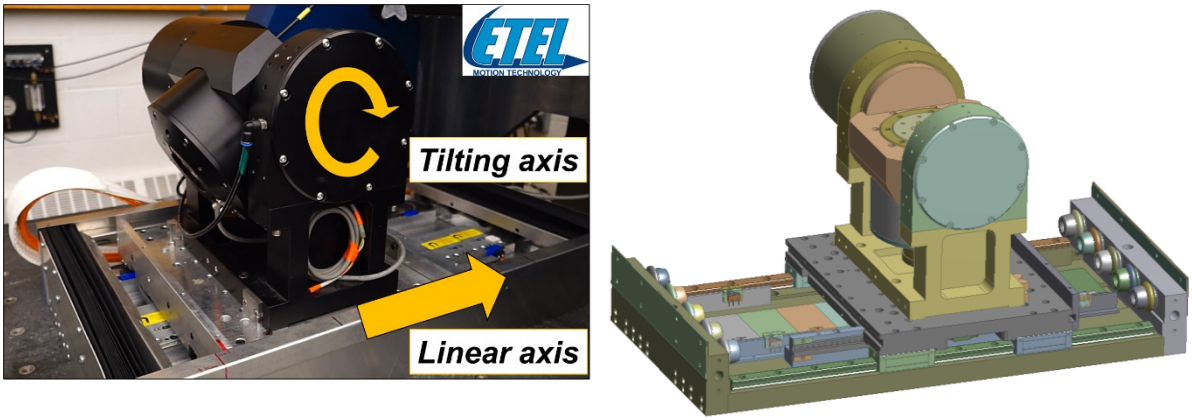

(a) Real setup. **(b) CAD model.**

Figure A-1 In-house linear-tilt-rotary feed drive.

A linear-trunnion feed drive that was available in the lab is shown in Figure A-1. Since all the axes are driven by direct drive motors, and the machine fame supporting the trunnion is well designed, the system is considered rigid. To create vibratory mode similar to the case shown in Section 5.3.2, a flexure should be made to connect the linear axis and the tilting axis to introduce mechanical flexibility.

Several design considerations are listed below.

- A bending mode can be excited by both the linear & tilting axis.
- The natural frequency should be around 30~50 Hz, similar to the characteristics of a medium or large-sized industrial machine tool.

- The setup should be safe to use. Safety factor is specified to be at least 10 when subject to 1 G linear acceleration.
- The flexure should be reconfigurable for other research applications.

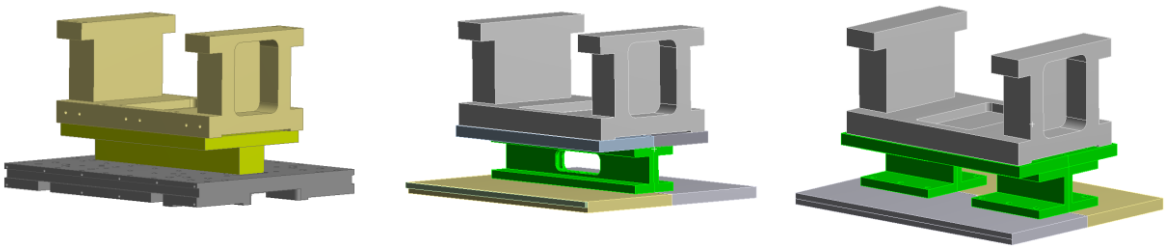

(a) **(b)** **(c)**

Figure A-2 Candidate flexure designs.

Taking the above considerations into account, three concept design candidates (see Figure A-2) were proposed. The candidate (c) was chosen due to the convenience of fabrication. Essentially, this flexure is composed of three parts, one plate on the top and two I-beams at the bottom. The plate is connected to the trunnion base frame. The two I-beams are connected to the linear table. Hence, if the value of natural frequency needs to be adjusted, only the I-beams need to be replaced.

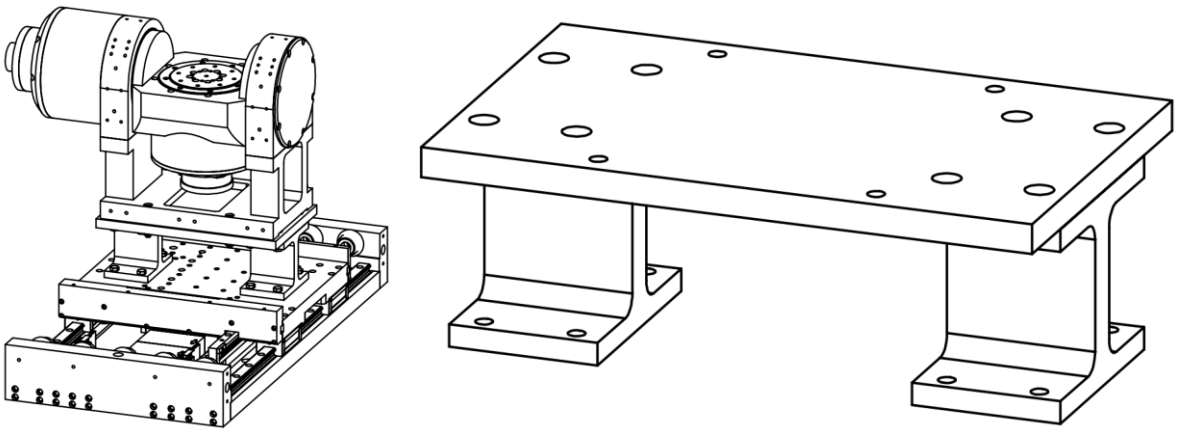

(a) Full assembly **(b) Flexure**

Figure A-3 Finalized flexure design.

Figure A-3 is the final design of the flexure. Finite element (FE) analysis was performed using ANSYS Workbench. The geometric parameters of the design are iteratively adjusted according to the result of FE simulation. The FE model of the feed drives is shown in Figure A-4 (a). Some details about building the FE model are described as follows.

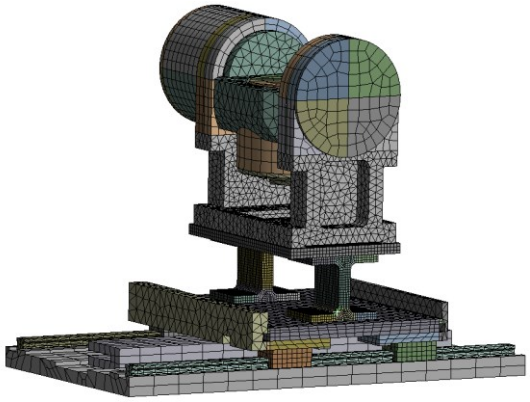

(a) The entire FE model.

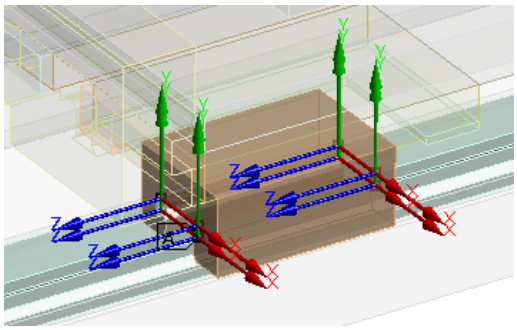

(b) Guide and rail connection by spring elements.

Figure A-4 FE model of the feed drive.

(1) To save the computational cost, the CAD model is simplified by removing small and trivial geometric features. If possible, hexahedral mesh is applied.

(2) By performing a simple back and forth motion experiment on the linear axis, the total mass of the linear table and the entire trunnion unit is identified as 62.2 kg. According to the CAD model, the total mass of the same moving components is 62.5 kg, which is very closed to the identified value. This indicates high confidence in the fidelity of the mass matrix of the model.

(3) Interfaces such as linear guideways and the air bearing for supporting the tilting axes are modelled by a series of spring elements. As shown in Figure A-4 (b), each coordinate represents one spring element. The equivalent stiffness parameters are set according to the product specifications.

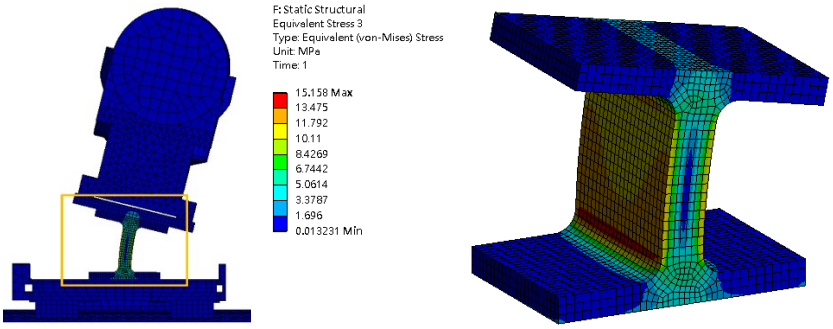

Figure A-5 Stress concentration around the I-beam when subject to 1G linear acceleration.

When subject to 1 G static linear acceleration while the linear motor is constrained, the simulated maximum stress is 15 MPa (see Figure A-5). The material of the I-beams is aluminum alloy 6061-T6

of which the yielding stress is 240MPa. Hence, the safety factor under this extreme case is 16, which is sufficiently high in a common engineering sense.

Validation

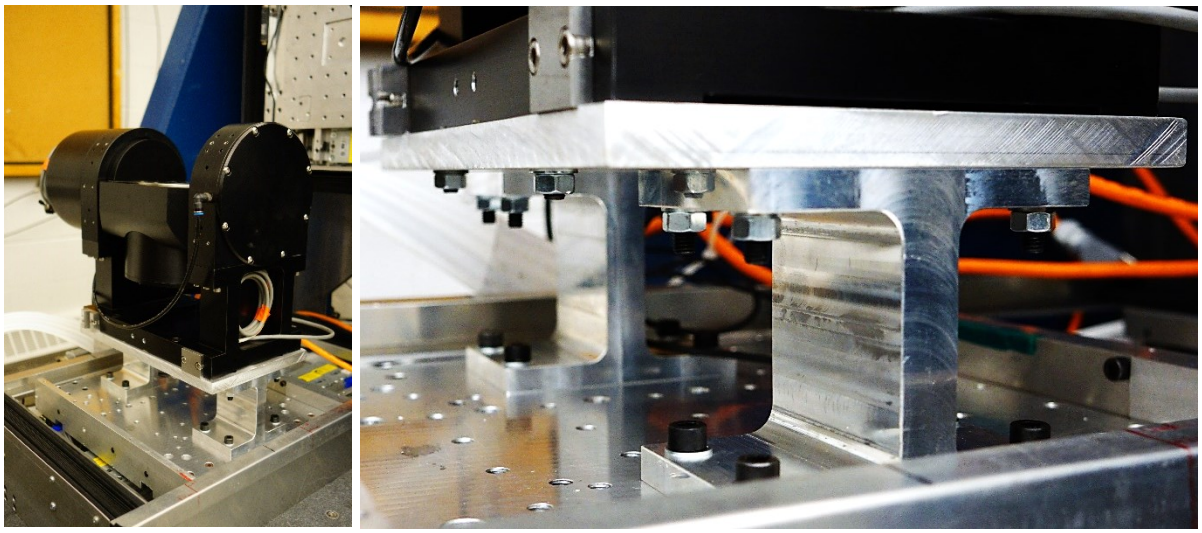

Figure A-6 Experimental feed drive.

	The primary bending mode		Lateral mode
	With motor constraint	No constraint	
Mode shape	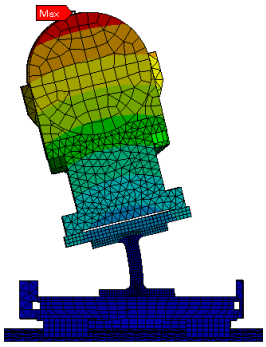	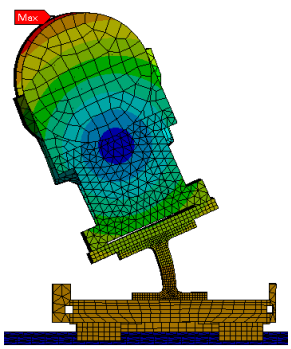	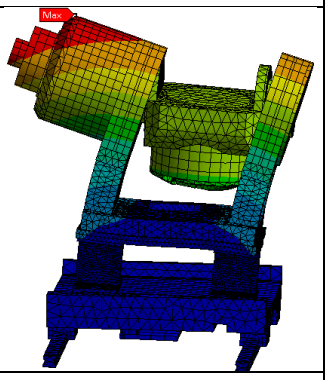
Simulated / actual natural frequency	23.8 / 20 [Hz]	39.5 / 34.6 [Hz]	81.5 / 75 [Hz]
Simulation error	13%	14%	8%

Figure A-7 FEA simulation result of the bending mode.

Figure A-6 is the final assembly of the flexure. The I-beams were made by pocketing solid aluminum blocks. Tap testing was conducted to verify the actual natural frequencies. The simulated and actual natural frequencies of the feed drives are shown in Figure A-7. The simulation errors are 8~14%, which

are accurate considering such a complex system. All the measured frequencies are slightly lower than the simulated frequencies, probably because some of interface compliance were overestimated.

The natural frequency of the primary bending mode without motor constraint is 34.6 Hz, which is a reasonable value for large industrial machine tools. The lateral bending mode (75 Hz) is not likely to be excited by the trajectory input since it is higher than a typical servo control bandwidth. Therefore, the experiments on this setup can only focus on the primary bending mode.

Appendix B

Estimation Results of IMU #2

Table B-1 Signal property of IMU #2.

		X	Y	Z
Gyro	Bias $[°/s]$	-6.855E-02	3.738E-02	6.225E-02
	RMS noise $[°/s]$	1.663E-01	9.148E-02	8.925E-02
Accelerometer	RMS noise $[mm/s^2]$	8.647	7.331	6.408

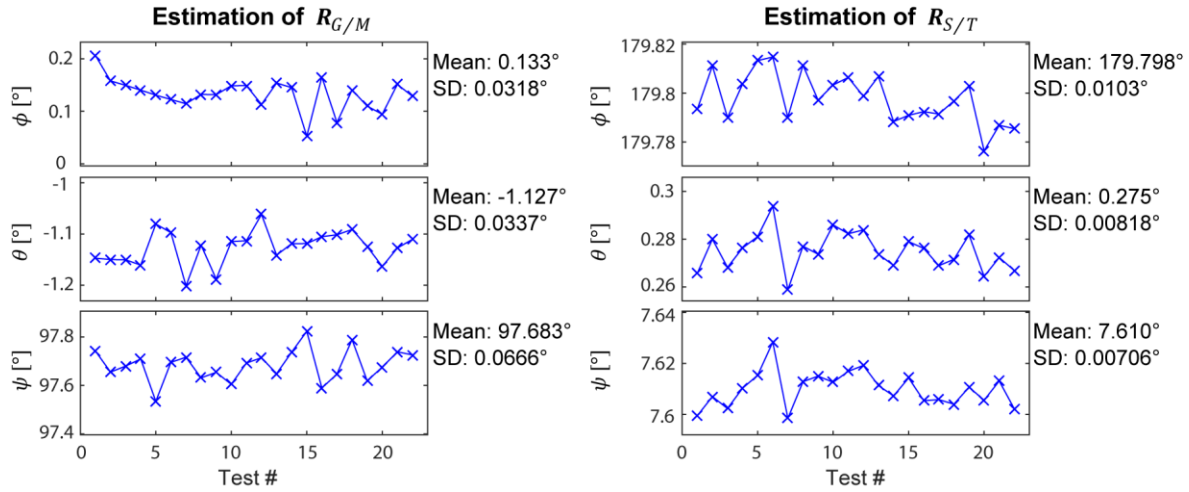

Figure B-1 Estimation of $R_{G/M}$ and $R_{S/T}$ expressed by $R_x(\phi)R_y(\theta)R_z(\psi)$ Euler angles.

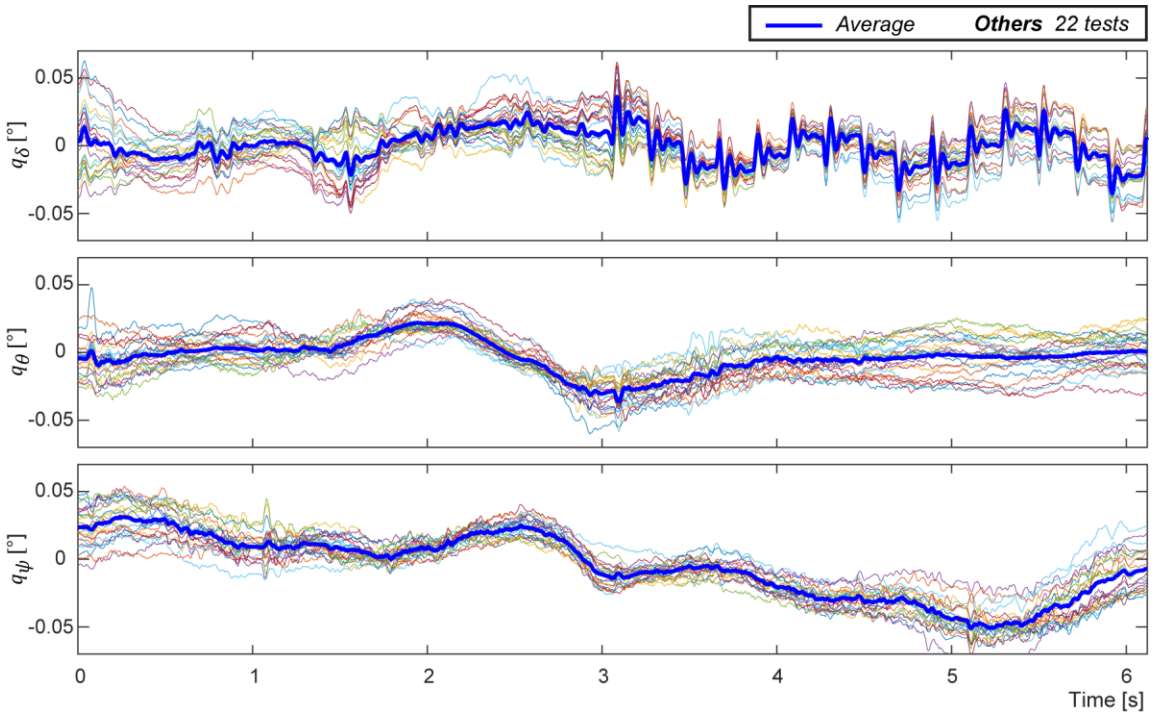

Figure B-2 Estimation of $R_{\delta/Y}$ represented with $R_x(q_\phi)R_y(q_\delta)R_z(q_\psi)$ Euler angles.

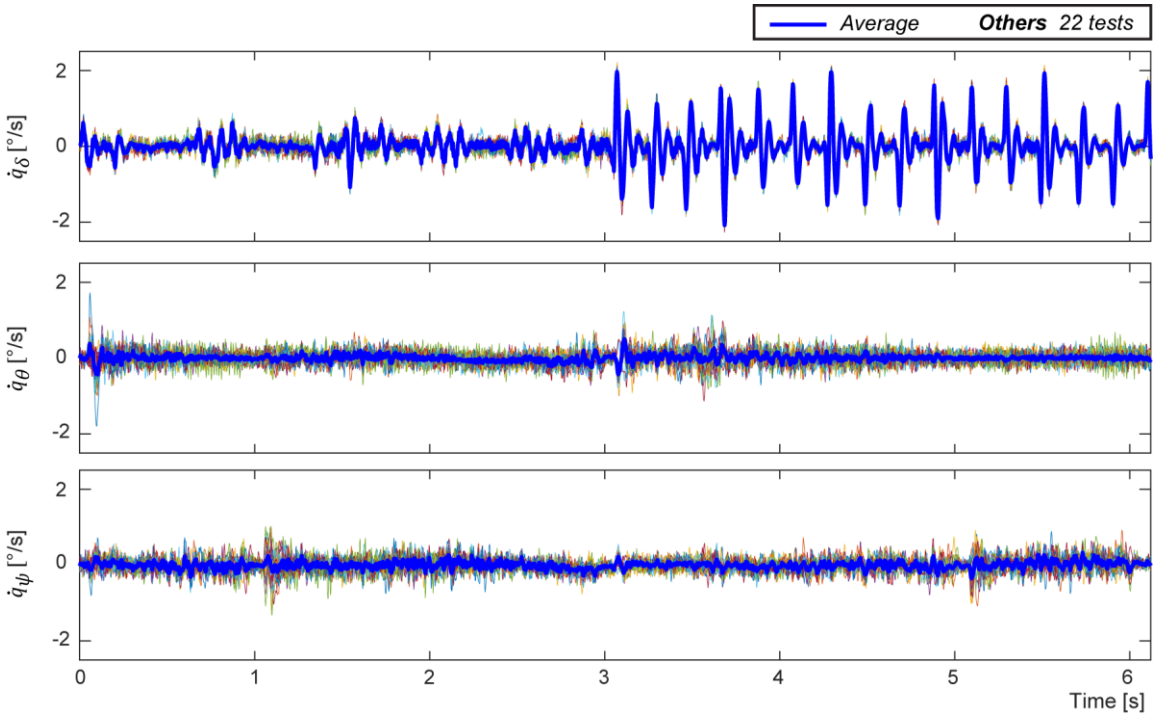

Figure B-3 Estimated angular velocity $\dot{q}_\phi$, $\dot{q}_\delta$, and $\dot{q}_\psi$.

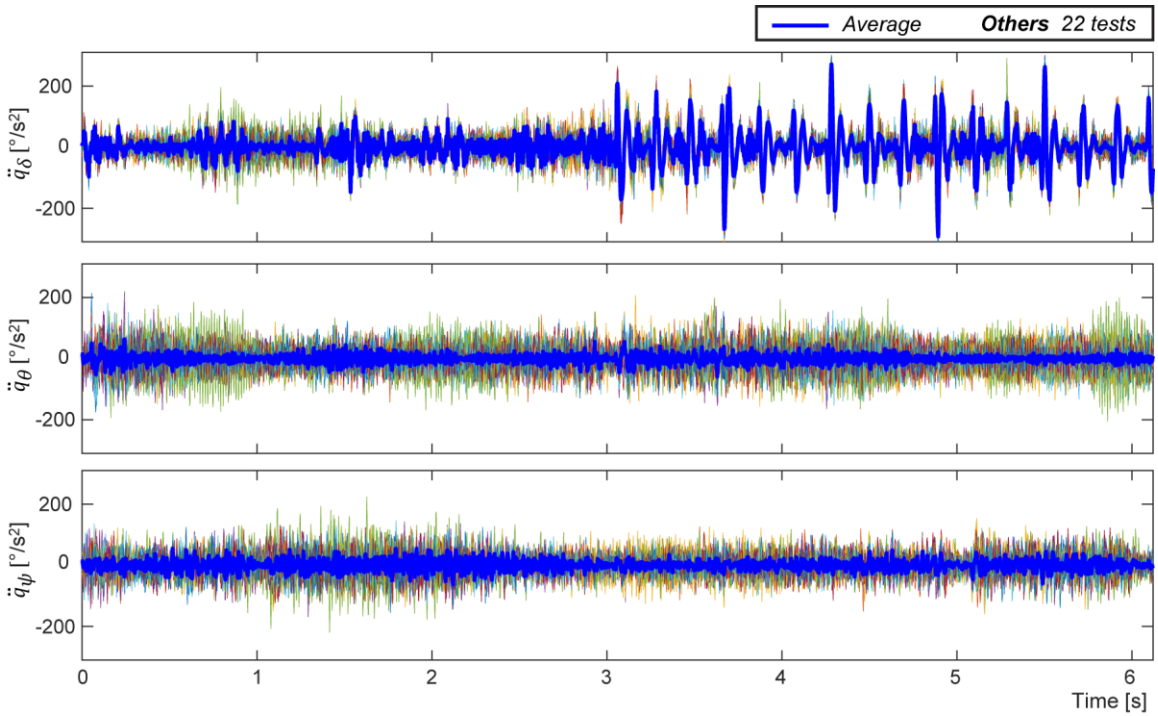

Figure B-4 Estimated angular acceleration $\ddot{q}_\phi$, $\ddot{q}_\delta$, and $\ddot{q}_\psi$.

Appendix C
Validation of the identified model

In Section 7.3, the dynamic model of the experimental feed drive was identified using the trajectory in the experiment in Section 6.5. To ensure that the identified model is accurate and not overfitting, the identified model was also validated by another trajectory, as shown in Figure C-1, where the kinematic limits are listed in Table C-1. The results of the simulation and experiment are compared in Figure C-1 and Table C-2.

Inter-axis vibratory coupling effect and posture-dependent effect are again induced by the validation trajectory due to the multi-axis simultaneous trajectory with high acceleration and jerk values. The simulation still accurately predicts the tracking error and motor force/current. The RMS error of simulation listed in Table C-2. The averaged normalized simulation error is 5.54%.

Table C-1 Kinematic limits of the trajectory for validation.

	Speed [mm/s] or [°/s]	Acceleration [mm/s^2] or [°/s^2]	Jerk [mm/s^3] or [°/s^3]
Y	2.85E+02	1.60E+03	9.03E+04
A	1.87E+02	2.34E+03	1.17E+05

Table C-2 RMS error of simulation for validation.

	Y-Axis		A-Axis	
	Tracking error e_Y [mm]	Motor force u_Y [N]	Tracking error e_A [°]	Motor torque u_A [N·m]
RMS error	2.248E-03	4.775E+00	3.630E-03	1.671E-01
Normalized RMS error	5.52%	6.63%	6.00%	4.02%

Normalized RMS error = RMS error ÷ RMS magnitude

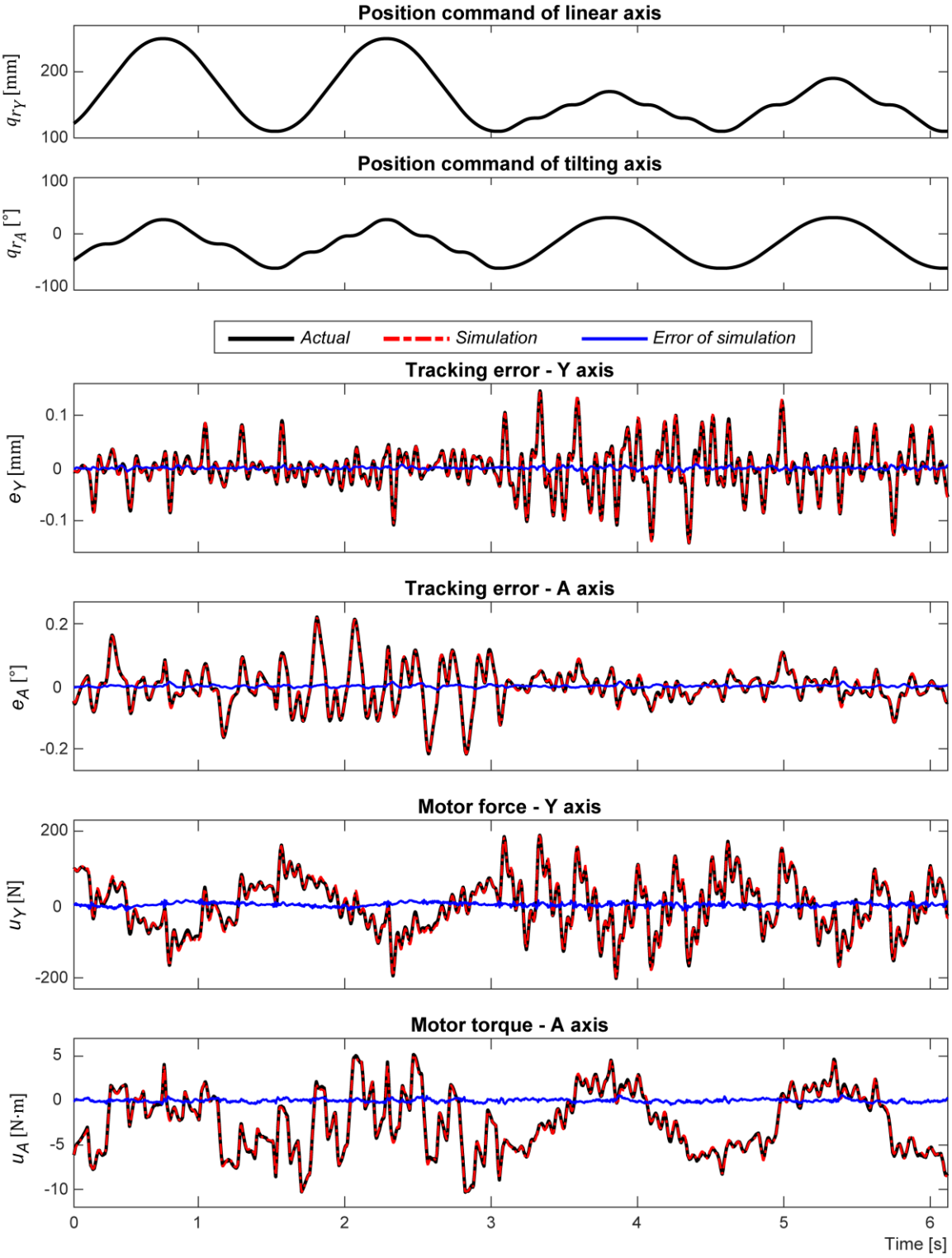

Figure C-1 Measurement and simulation results for validation.